UNIVERSITÉ DU LUXEMBOURG

PhD-FSTM-2023-020

The Faculty of Science, Technology and Medicine

DISSERTATION

Defence held on 20/02/2023 in Luxembourg

to obtain the degree of

DOCTEUR DE L'UNIVERSITÉ DU LUXEMBOURG EN INFORMATIQUE

by

Gabriel Tedgue Beltrão

Born on 18 June 1986 in Salvador (Brazil)

Signal Processing Contributions to Contactless Monitoring of Vital Signs Using Radars

Dissertation defence committee

Dr. Bhavani Shankar, dissertation supervisor

Assistant Professor, Université du Luxembourg

Dr. Avik Santra

Principal Engineer, Infineon

Dr. Mohammed Jahangir

Research Fellow, University of Birmingham

Dr. Björn Ottersten, Chairman

Professor and Director of SnT, Université du Luxembourg

Dr. Udo Schroeder, Vice Chairman

Research Scientist, IEE S.A.

Dissertation Defence Committee

Committee members:	Prof. Dr. Björn Ottersten, Chairman *Professor and Director of SnT, University of Luxembourg* Dr. Avik Santra *Principal Engineer, Infineon* Dr. Mohammed Jahangir *Research Fellow, University of Birmingham*
Supervisor:	Prof. Dr. Bhavani Shankar *Assistant Professor, SnT, University of Luxembourg*
Co-supervisor:	Dr. Udo Schroeder *Research Scientist, IEE S.A., Luxembourg*

Affidavit

I hereby confirm that the PhD thesis entitled "Signal Processing Contributions to Contactless Monitoring of Vital Signs Using Radars" has been written independently and without any other sources than cited.

Luxembourg, _____ _____

Gabriel Tedgue Beltrão

Abstract

Vital signs are a group of biological indicators that show the status of the body's life-sustaining functions. They provide an objective measurement of the essential physiological functions of a living organism, and their assessment is the critical first step for any clinical evaluation. Monitoring vital sign information provides valuable insight into the patient's condition, including how they are responding to medical treatment and, more importantly, whether the patient is deteriorating. However, conventional contact-based devices are inappropriate for long-term continuous monitoring. Besides mobility restrictions and stress, they can cause discomfort, and epidermal damage, and even lead to pressure necrosis. On the other hand, the contactless monitoring of vital signs using radar devices has several advantages. Radar signals can penetrate through different materials and are not affected by skin pigmentation or external light conditions. Additionally, these devices preserve privacy, can be low-cost, and transmit no more power than a mobile phone. Despite recent advances, accurate contactless vital sign monitoring is still challenging in practical scenarios. The challenge stems from the fact that when we breathe, or when the heart beats, the tiny induced motion of the chest wall surface can be smaller than one millimeter. This means that the vital sign information can be easily lost in the background noise, or even masked by additional body movements from the monitored subject. This thesis aims to propose innovative signal processing solutions to enable the contactless monitoring of vital signs in practical scenarios. Its main contributions are threefold: a new algorithm for recovering the chest wall movements from radar signals; a novel random body movement and interference mitigation technique; and a simple, yet robust and accurate, adaptive estimation framework. These contributions were tested under different operational conditions and scenarios, spanning ideal simulation settings, real data collected while imitating common working conditions in an office environment, and a complete validation with premature babies in a critical care environment. The proposed algorithms were able to precisely recover the chest wall motion, effectively reducing the interfering effects of random body movements, and allowing clear identification of different breathing patterns. This capability is the first step toward frequency estimation and early non-invasive diagnosis of cardiorespiratory problems. In addition, most of the time, the adaptive estimation framework provided breathing and heart rate estimates within the predefined error intervals, being capable of tracking the reference values in different scenarios. Our findings shed light on the strengths and limitations of this technology and lay the foundation for future studies toward a complete contactless solution for vital signs monitoring.

Dedicated to my beloved wife, daughter, and my family

Acknowledgements

It has been a long and challenging journey, but I am grateful to have had the support of so many throughout this process.

I want to express my gratitude to my supervisor Bhavani Shankar, who guided and pushed me constantly towards my best performance. Additionally, and more importantly, for being more than a "boss", a true friend. I also had the privilege of having multiple "mentors". The same gratitude goes to them: Mohammad Alaee, Udo Schröder, Wallace Alves Martins, Dimitri Tatarinov, and Regine Stutz; for their guidance and valuable feedback.

I also want to thank my friends and colleagues from the SPARC and SIGCOM groups in the SnT. It was amazing to share these moments with them. Not only during lunch and coffee breaks, but also along nice technical discussions, and uncountable radar measurements.

I am also deeply grateful to my family and loved ones, especially my wife, for her unwavering encouragement and understanding during this time. This adventure wouldn't even have started without her. Her sacrifices, her dedication, and support, have been a constant source of strength and inspiration for me. I could not have completed this journey without her. More than that, she gave me, and now we know, the true meaning of love: she is called Duda.

Thanks to my thesis committee: Dr. Bjorn Ottersten, Dr. Avik Santra, and Dr. Mohammed Jahandir. For providing valuable comments and insights.

Finally, thanks SnT (Interdisciplinary Centre for Security, Reliability and Trust), IEE Sensing, and FNR (Fonds National de la Recherche), for supporting this PhD project.

Thank you all for being a part of this journey!

This work was supported by the FNR, under the FNR Industrial Fellowship Grant, project MIDIA, Reference 14269859.

Gabriel Tedgue Beltrão
Luxembourg, March, 2023

Contents

List of Figures

List of Tables

Acronyms

A | C | D | E | F | G | H | I | L | M | N | P | Q | R | S | T | U | V | W

A

ACC-FTPR autocorrelation frequency-time phase regression. 53

AD arctangent demodulation. 30, 31, 39–41, 50–53, 61, 63, 64, 67, 70, 77, 78, 108, 113

ADC analog-to-digital converter. 27–29, 34, 47, 64, 75, 77, 78, 83, 87, 88, 103, 107, 128, 130

ANLS adaptive nonlinear least squares. 104, 120–125, 127, 129, 132

ANS autonomic nervous system. 8

AWGN additive white Gaussian noise. 49

C

CEEMDAN complete ensemble EMD with adaptive noise. 32

CFAR constant false-alarm rate. 29

CPI coherent processing interval. 29, 114, 115, 133

CSD complex-signal demodulation. 30, 31, 40, 41, 50–52, 77, 78, 80, 108

CW continuous-wave. 27, 28, 47, 74, 77, 87–89, 103, 124

CZT chirp Z-transform. 33

D

DACM differentiate and cross-multiply. 31, 51–53

DC direct current. 31, 34, 48, 50, 77, 82, 108, 128

DFT discrete Fourier transform. 29, 33, 51, 53, 55–58, 84–86, 107, 120–123, 125

DSP digital signal processing. 1, 19, 24, 28

E

ECG electrocardiography. 7, 9, 129, 130

EEMD ensemble empirical mode decomposition. 32

EMD empirical mode decomposition. 32

EWS Early Warning Scores. 2, 9, 10

EWT empirical wavelet transform. 32

F

FDA US Food and Drug Administration. 131

FFT fast Fourier transform. 105, 112, 115

FMCW frequency-modulated continuous-wave. 27–31, 47, 87, 103–105, 118, 124, 125, 132

G

GUI graphical user interface. 34, 36–38

H

HRV heart rate variability. 8

I

ICA independent component analysis. 32

ICU Intensive Care Unit. 6, 11, 129

iPPG imaging photoplethysmography. 14

ISM industrial, scientific and medical. 26, 76, 88

L

LD linear demodulation. 31, 51–53

LM Levenberg–Marquardt. 108

M

MARSI Medical adhesive–related skin injuries. 12

MIMO multiple-input multiple-output. 27, 87, 132

N

NICU Neonatal Intensive Care Unit. 12, 17, 20, 71, 73–77, 83, 87, 88, 131, 132

NLS nonlinear least squares. 43, 53, 82, 84, 85, 104, 111–118, 121, 122, 125, 129, 132

NMF nonnegative matrix factorization. 32, 79–81, 84, 88, 90, 91, 127–129, 132

NRE normalized recovery error. 67, 68, 70

P

PCA principal component analysis. 31, 51

PMCW phase-modulated continuous-wave. 27, 28, 47

PPG photoplethysmography. 7, 9, 14

Q

QCT quadrature cosine transform. 33

R

RBM random body movement. 16, 17, 31, 32, 59, 61–63, 66–71, 75, 79–82, 84–87, 90–92, 101, 127–129, 131–133

RCS radar cross section. 26, 39

RELAX relaxation. 56–58

RF radio frequency. 27

RMSE root-mean-square error. 49, 51–58, 85–87, 121–125

ROI region of interest. 15

ROI return over investment. 11

rPPG remote photoplethysmography. 14

S

SCG seismocardiogram. 25

SFCW stepped-frequency continuous-wave. 27

SINR signal-to-interference-plus-noise ratio. 31, 129

SIR signal-to-interference ratio. 49, 55–58, 104

SNR signal-to-noise ratio. 27, 29, 30, 32, 34, 49, 51, 53–58, 82, 83, 104, 107, 109, 115, 118, 120, 129

STFT short-time Fourier transform. 33, 80, 90, 91, 132

STPC slow-time phase correlation. 129

T

TA time-analysis. 53, 54

U

US Unlimited Sampling. 59, 61, 64–70, 127, 128, 131, 132

UWB ultrawideband. 27, 103

V

VMD variational mode decomposition. 32

VSM vital sign monitoring. 11, 13–16, 24, 26–29, 32, 34, 131

W

WHO World Health Organization. 6

"Celebrate we will, because life is short but sweet for certain. We are climbing two by two, to be sure these days continue."

Steve Lillywhite

Chapter 1

Introduction

People are living longer. Between 2015 and 2050, the proportion of the world's population over 60 years will nearly double, and outnumber children under the age of 5 [1]. Due to the rapid aging of the population worldwide, a lot of effort is being dedicated to providing more efficient and accessible healthcare solutions.

In this context, monitoring vital signs is of paramount importance. These critical physiological parameters play a crucial role in the early detection of conditions that affect the well-being of a patient. By continuously monitoring vital signs, it is possible to detect drowsiness [2], sleep apnea [3], and even depression [4].

However, conventional contact-based devices are inappropriate for long-term continuous monitoring. Besides mobility restrictions and stress, they can cause discomfort, and epidermal damage, and even lead to pressure necrosis [5–10].

On the other hand, the contactless monitoring of vital signs using radar devices has several advantages. Radar signals can penetrate through different materials and are not affected by skin pigmentation or external light conditions. Additionally, these devices preserve privacy, they can be low-cost, and they transmit no more power than a mobile phone [11–13].

Despite recent advances, accurate contactless vital sign monitoring is still challenging in practical scenarios. The challenge stems from the fact that when we breathe, or when the heart beats, the tiny induced motion of the chest wall surface can be smaller than one millimeter. This means that the vital sign information can be easily lost in the background noise, or even masked by additional body movements from the monitored subject [14–16].

The goal of this thesis is to propose innovative radar digital signal processing (DSP) solutions to enable the contactless monitoring of vital signs in practical scenarios.

1.1 Motivation

Vital signs are a group of biological indicators that show the status of the body's life-sustaining functions. They provide an objective measurement of the essential physiological functions of a living organism, and their assessment is the critical first step for any clinical evaluation. Traditionally, there are four primary vital signs: body temperature, blood pressure, breathing rate, and pulse rate (heart rate). In the last few decades, monitoring vital signs has become an active area of research, with numerous studies reporting that abnormal changes in vital signs can be early indicators of patient deterioration and adverse events [17].

1.1.1 Why do we need to monitor vital signs?

The assessment of vital signs is essential for high-quality care. Vital sign information provides valuable insight into the patient's condition, including how they are responding to medical treatment and, more importantly, whether the patient is deteriorating [18]. Abrupt changes in vital signs typically correlate with changes in the cardiopulmonary status of the patient and often indicate that a higher level of attention is needed [19].

Vital signs can provide early warning of cardiac arrest and its common causes, such as myocardial infarction, respiratory failure, and sepsis [20]. The diagnosis of sepsis, for instance, is usually based on the evidence of infection with the presence of a systemic inflammatory response [21]. This, in turn, is defined by three of the primary vital signs: either elevated or lowered body temperature, elevated heart rate, and high respiratory rate. The presence of hypotension (low blood pressure) can also be an indicator of a more serious infection, such as severe sepsis. The respiratory rate and shock index (defined as the ratio of heart rate to systolic blood pressure) have also been demonstrated to be independent prognostic factors in patients with suspected infection [22].

In addition, vital sign values are often used as a tool for decision-making in terms of clinical behavior and patient care [23]. Early Warning Scores (EWS), mostly using vital sign abnormalities, are guides used by medical services to quickly determine the degree of illness of a patient. They are based on the principle that clinical deterioration can be seen through changes in multiple physiological measurements. The observations are used to generate a single composite score which is statistically linked to an increased likelihood of patient deterioration. Within hospitals, EWS are used as a trigger system in which an increasing score produces an escalated response, varying from a higher frequency of patient observation up to urgent review by a rapid response team. Fig. 1.1 shows an observation chart for an EWS used in the UK [24].

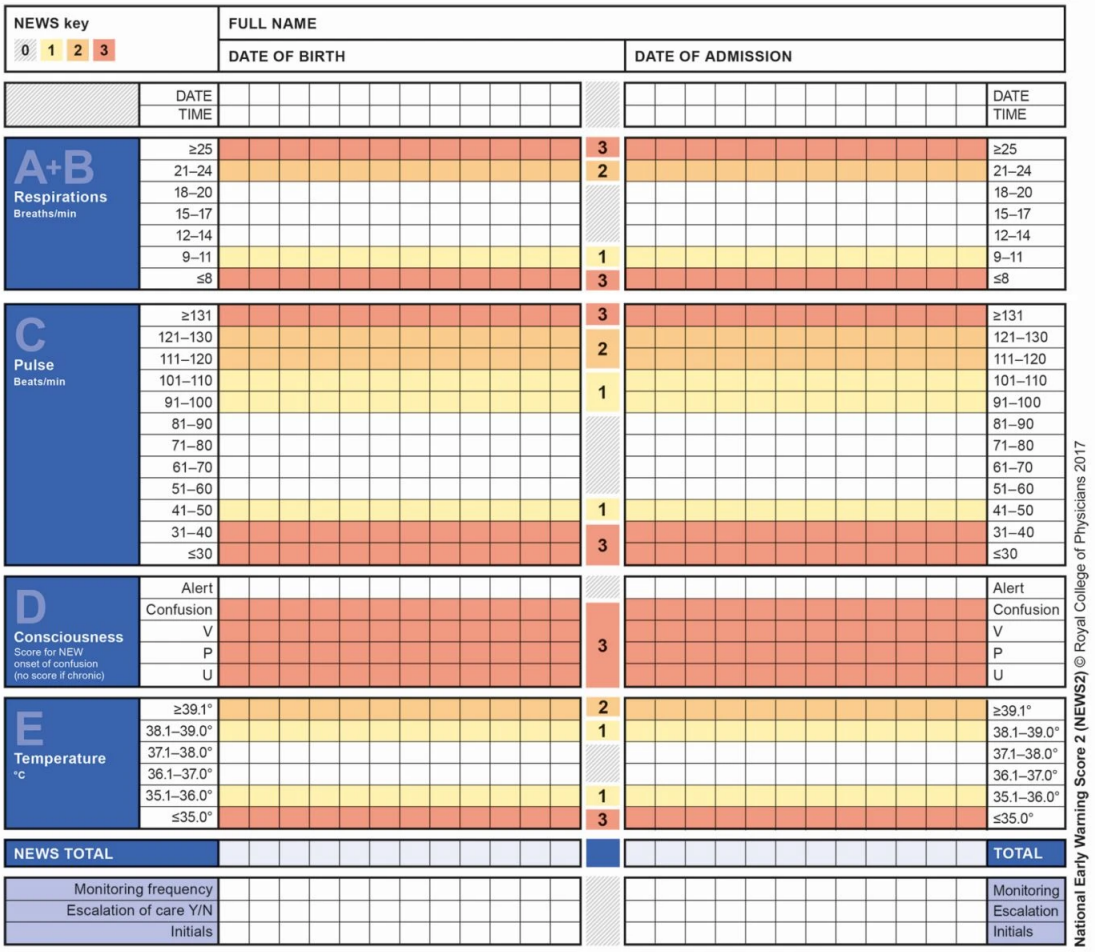

FIGURE 1.1: National Early Warning Score observation chart (adapted from [24] - reproduced with permission from Springer Nature).

Furthermore, many diseases manifest in similar symptoms, and measuring vital signs can help prevent misdiagnosis. Recent research has shown that vital signs can be used with artificial intelligence for distinguishing between viral infections. More specifically, based on vital sign information, machine-learning models can be trained to accurately diagnose and differentiate hospitalized patients with COVID-19 or seasonal influenza [25]. This indicates that vital signs can be used for improving diagnosis, especially when the healthcare system lacks relevant information about a patient [26].

Therefore it is clear that monitoring vital signs is a key component of healthcare and a fundamental nursing priority. However, as we will show throughout this chapter, several studies seem to indicate their importance is underestimated and measurements are often neglected.

In the next subsections and throughout this thesis we will focus on two of the four primary vital signs: the breathing rate and the heart rate. These are currently the vital

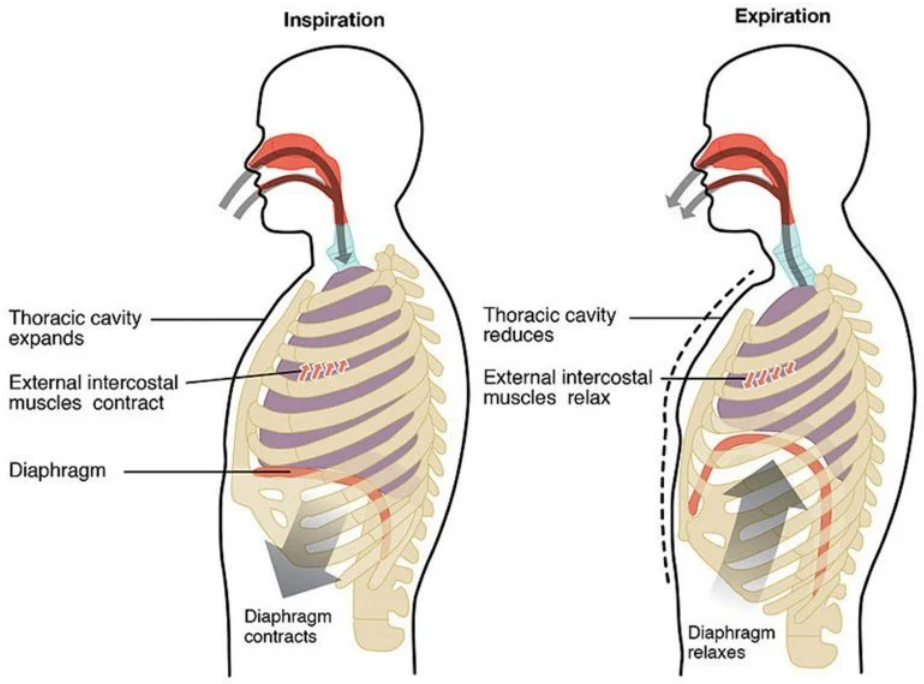

FIGURE 1.2: Inspiration and expiration (adapted from [29] - licensed under CC BY 4.0).

signs that can be measured in a contactless way using radar systems. Therefore, these vital signs are the main focus of this research.

1.1.2 Breathing (respiration) rate

Respiration is by definition a single complete act of breathing [27]. It is also defined as the physicochemical process by which an organism supplies its cells and tissues with the oxygen needed for metabolism, and relieves the carbon dioxide formed in energy-producing reactions. All aerobic organisms need oxygen to produce energy and, in this process, carbon dioxide is generated as a waste product that needs to be removed from the body [28].

In other words, respiration is the movement that brings oxygen from the external environment to the cells and moves carbon dioxide in the opposite direction. In mammals, it involves respiratory cycles of inhaled and exhaled breaths. The inhalation is usually an active process, started by the contraction of the diaphragm muscle. It causes a pressure variation that brings air into the lungs expanding them. This air is then diffused across the alveolar-capillary interface and reaches the entire body through the arterial blood. In contrast, exhalation (breathing out) is usually a passive process. Fig. 1.2 illustrates the breathing process.

The breathing rate, or respiratory rate, is the number of breaths per minute. At rest, normal breathing rate values for healthy adults are around 12 to 20 breaths per minute (bpm) [15]. However, many factors can affect these limits, including age, activity, emotional state, fever, and medications. For premature infants, for instance, average breathing rates can normally reach 60 bpm [30] and go up to 80 bpm under specific conditions [31]. In any case, a normal respiration rhythm should be even and regular with equal pauses between inhaling and exhaling [28].

Respiration is carefully controlled by the actions of central and peripheral chemoreceptors and lung receptors. The body attempts to correct hypoxemia (low levels of oxygen in your blood) and hypercarbia (increased carbon dioxide levels) by increasing both the tidal volume (amount of air that moves at each cycle) and the respiratory rate [32]. Tachypnea (rapid breathing) is a condition described by an abnormally high breathing rate. It can occur under common physiological conditions (exercises, emotional changes, or pregnancy), but also under many pathological conditions such as pain, pneumonia, asthma, anxiety, and sepsis, just to cite a few. On the other side, bradypnea is an abnormally low breathing rate. It can be caused due to worsening of underlying respiratory conditions leading to respiratory failure, or due to the usage of central nervous system depressants. More extremely, an apnea event is the complete cessation of airflow to the lungs for at least 10 seconds. It is commonly caused by airway obstructions, but it can also appear during cardiopulmonary arrests, and in case of a drug overdose [33].

The depth of breathing is also an important parameter. Hyperpnea is described as an increased depth of breathing which can be seen in anxiety states, lung infections, and congestive heart failure. It can evolve to hyperventilation, where both rate and depth of breathing are high, and can indicate pathological conditions like diabetic ketoacidosis or lactic acidosis. In contrast, the term hypoventilation describes the decreased rate and depth of breathing. This condition can be a result of excessive sedation, metabolic alkalosis, or instances of obesity hypoventilation syndrome [32].

The pattern of breathing also gets affected by various conditions that can indicate an underlying pathology. Fig. 1.3 illustrates a few examples. The Kussmaul's breathing pattern refers to an increased depth of breathing, although at a constant breathing rate. This presentation can be seen in patients with renal failure and diabetic ketoacidosis [34]. Biot respiration is a condition characterized by a highly irregular or ataxic breathing pattern, with variable tidal volumes and random periods of apnea [35]. This pattern is suggestive of raised intracranial pressure or conditions like meningitis. Finally, the Cheyne-Stokes breathing pattern is similar to Biot's (alternating breathing and apnea periods), however, with a sequential increase and decrease in depth during the breathing periods. It occurs in conditions of raised intracranial pressure, but it can also be seen

during excessive usage of sedatives and worsening congestive heart failure. Cheyne-Stokes is pathophysiological in adults but very common in newborns. Due to their immature respiratory system, premature infants often show periodic Cheyne-Stokes respiration. With increasing maturity, this transitions to a regular breathing pattern [36].

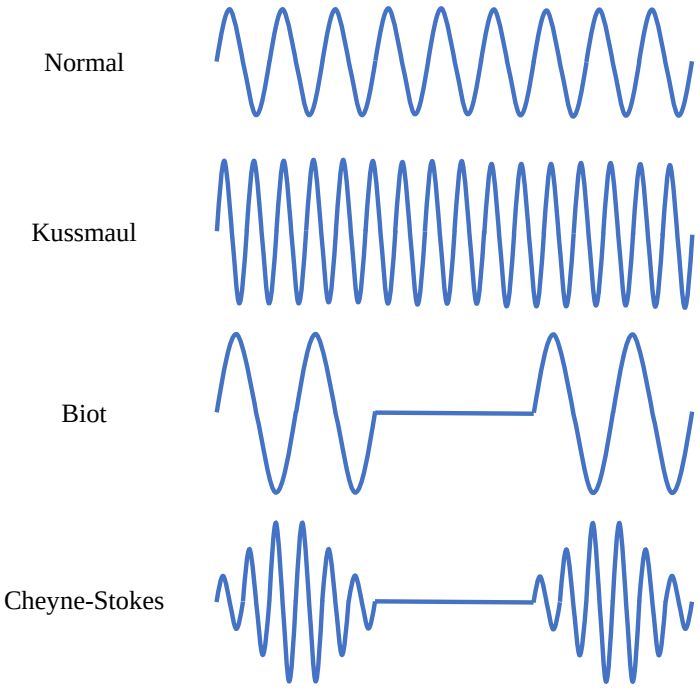

FIGURE 1.3: Breathing patterns.

The breathing rate is often the first vital sign affected if there is a change in the cardiac or neurological state of a patient [37]. Abnormal breathing rate values can occur up to 24 hours before other signs of clinical deterioration [38], and have been associated with a 13-fold increased risk of mortality [39]. The tachypnea, for instance, is one of the most significant predictors of in-hospital cardiac arrest and admission to Intensive Care Units (ICUs). In fact, it was already reported that a respiratory rate higher than 27 breaths/minute was the most important predictor of cardiac arrest in hospital wards [40]. Another study showed that 21% of critical care patients with a respiratory rate between 25 bpm to 29 bpm died in the hospital. Those with a higher respiratory rate had an even higher mortality rate [41].

There are several methods and devices for monitoring the breathing rate, relying on different measuring principles. They can be based on the analysis of variations caused by the breathing activity in the airflow, air temperature, air components, or air humidity [42]. Despite all these options, the breathing rate is still widely measured by counting breaths manually. In fact, the World Health Organization (WHO) recommends the assessment of the breathing rate by a 60-second visual count or auscultation for the number of breaths taken. In addition, it states this is the most reliable method (gold standard) [43]. Besides

being labor-intensive, this approach is also unsuitable for the early detection of patient deterioration [44].

When considering automated and continuous breathing monitoring, capnography (which measures carbon dioxide levels breath by breath) may be the more accurate method [45]. Being intrinsically quite intrusive, these devices are generally only available in critical care areas and are used only with patients who are intubated and sedated. Impedance pneumography, electrocardiography (ECG), and photoplethysmography (PPG) are less invasive methods also widely used for continuous breathing monitoring. While the first one measures changes in the electrical activity over the chest during inhalation and exhalation, the others are cardiac sensors that can also measure respiration by analyzing its modulation effects over the cardiac activity [44].

Despite the growing interest in using these techniques for continuous breathing monitoring, due to the contact-based nature of the used devices, both have limitations in performance and usability for long-term monitoring [46]. Extensive reviews on methods and devices for breathing monitoring can be found in [42, 44, 45, 47, 48]

1.1.3 Heart (pulse) rate

The arteries are blood vessels responsible for carrying blood from the heart to all other organs within the human body. Besides delivering oxygen and nutrients to all cells and tissues, the arterial system - part of the circulatory system - also contributes to removing carbon dioxide and waste products from the cells. The aorta is the largest and most important artery in the human body, originating from the left ventricle, and extending down to the abdomen [49].

When the heart beats, it pushes blood into the aorta, which must expand to receive this new volume. This movement creates a pressure wave through the walls of the arterial system. This is the pulse. This pulse travels through the entire body, but it can be most easily felt at points where the arteries approach the body surface. The heart rate can be measured simply by counting the number of pulses (beats) in a minute [50].

As the breathing rate, the heart rate also provides relevant information for assessing physiological and pathological processes affecting the body. Normal values for the heart rate in healthy adults at rest range from 60 to 100 beats per minute [15]. This can also vary based on different factors including age, gender, activity, emotional state, metabolism, and medications taken. Abnormally high and low heart rates are referred to as tachycardia and bradycardia, respectively [51].

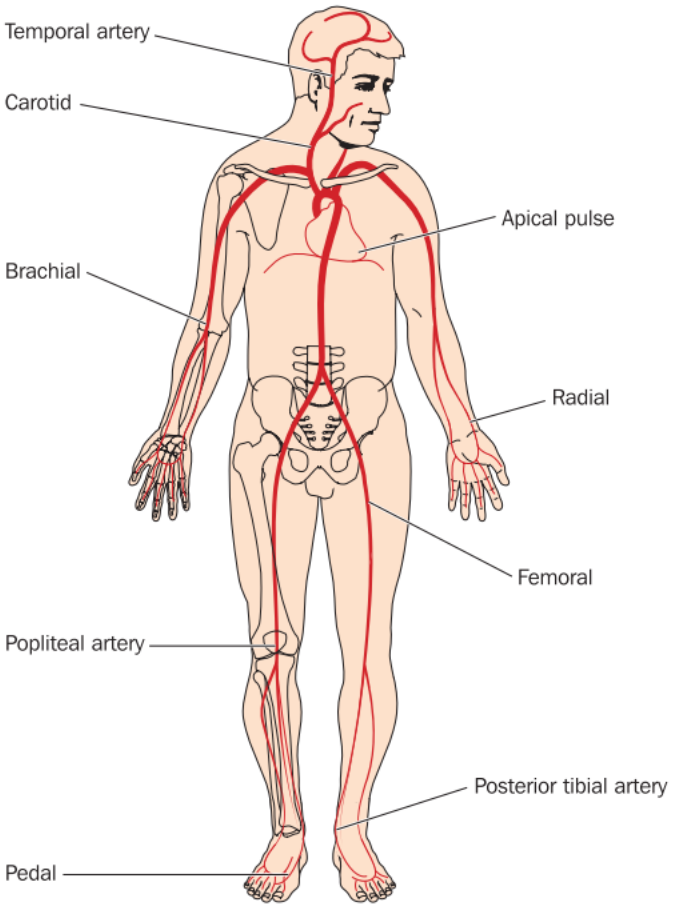

FIGURE 1.4: Arterial system (adapted from [51] - used with permission).

Continuous monitoring of the heart rate enables evaluation of parameters such as the heart rate variability (HRV) [52]. As this physiological parameter is controlled by the autonomic nervous system (ANS), it provides rich information about the physical and mental status of a patient [53]. The ANS is involved in the regulation of many important life-sustaining functions, such as homeostasis, blood pressure, and digestion. Imbalances in the ANS function can be an indicator of impending cardiac diseases and even sudden cardiac death, one of the leading causes of cardiovascular mortality [54].

The data acquisition of cardiovascular parameters is usually done in a clinical environment, being carried out by medical staff. The heart rate is commonly measured manually, especially outside critical care. While the radial artery is most commonly used, the pulse can be easily felt at any of the artery sites (please refer to Fig. 1.4), by carefully compressing the appropriate position.

It is important to clarify that the heart rate and pulse rate are technically different. The heart rate refers to the number of heart contractions (heartbeats) over time, whereas the pulse rate measures the rate of resulting blood pressure changes throughout the body. For individuals with certain heart conditions or circulatory disorders, the heart may not

efficiently push blood through the body within each contraction. These individuals may have a pulse rate that is lower than their heart rate. However, for most people, each heart contraction produces a pulse and the heart rate will often be synchronized with the pulse. Therefore, in general, the pulse is an effective way to measure the heart rate.

The two most common methods for continuous heart rate monitoring are the ECG and the PPG. The former uses several body-attached electrodes to capture the electrical activity controlling the expansion and contraction of the heart. The latter analyzes the light reflection around peripheral arteries to detect blood volume changes occurring due to the heartbeats. Therefore, while ECG sensors are directly measuring the heart rate, PPG sensors actually measure the pulse rate.

Despite being the gold standard for measurements in clinical settings, ECG devices are relatively expensive and require precise placement of electrodes. On the other hand, PPG devices are cheaper and easier to use. Although based on a different concepts and measuring different phenomena, both methods provide reliable results when properly executed. However, as we will show later, performance and usability for long-term monitoring are limited by several factors, deriving mostly from the need for physical contact with the monitored subject [54].

From now on we will be using the acronym "bpm" alternatively as breaths per minute (when talking about the breathing rate) or beats per minute (when talking about the heart rate). The meaning will be clear from the context.

1.1.4 Continuous monitoring is essential

The importance of monitoring vital signs in clinical practice is indisputable, but how frequently they should be measured is still unclear [17]. Despite some agreement in literature regarding how often measurements should be taken, and what parameters should always be measured, it seems this is based on perceived best practice rather than evidence [55].

Recording a full set of vital signs at least daily is considered standard for monitoring patients in acute hospital wards [41]. However, there is strong variability between institutes and countries, and this depends on clinical conditions, staff availability, cost issues, organizational practices, etc. For instance, a 12-hourly minimum frequency is used in the UK, with the timing of subsequent observations being derived from EWS [55]. There is also evidence that the frequency of measurements also varies according to the moment in which the patient enters the hospital [22]. During the night shift, patients

had a higher frequency of measurements and less missing data than those visiting the emergency department during the day or evening [56].

Despite the use of electronic equipment, some of the vital signs are often still measured through manual procedures and observation, leading to insufficient, subjective, and, most of the time, unreliable results [57]. Recent studies have found that the level of documentation of vital signs in many hospitals is poor [41]. In pediatric emergency departments, 60% and 42.3% of patients had no record of respiratory and heart rates, respectively [56]. According to [58], poor clinical monitoring was also responsible for a third of preventable deaths in British hospitals. An audit in Australian hospitals found that 83% of medical records had incomplete documentation of vital signs, with the respiratory rate being the most neglected [39].

In fact, the breathing rate has consistently been the least frequently measured vital sign. It is often not recorded, even when the patient's primary problem is a respiratory condition [41]. Another study reported that in pediatric patients with suspected infection, the respiratory rate had not been measured in 15% of the cases [22], and when patients were evaluated as "not seriously ill", medical staff tended to skip the measurement of all vital signs.

Regarding EWS, despite having relevant predictive value, they are limited by the intermittent nature of the measurements [59]. Although accurately predicted by vital sign changes, clinical deterioration often goes unnoticed or is not detected until it is too late to treat [17]. Vital signs are measured at predetermined intervals, with patient deterioration possible between recordings. Numerous studies have highlighted a lack of vital sign measurements in the hours preceding life-threatening events, with more than 75% of patients having at least one vital sign unrecorded immediately before the event [39]. This gap between observations seems to be one of the primary failings of EWS-systems [19]. For instance, considering patients with septic shock, there is an 8% increase in mortality for every hour of delay in antibiotic administration [59].

In summary, regardless of its clinical importance, research has consistently found that vital sign assessment is neglected in clinical practice. Recordings are often inaccurate, incomplete, and even falsified [60]. Whilst this neglect is not a new clinical issue, the reasons for this remain unclear [39]. In addition, intermittent monitoring prevents full exploitation of vital sign information and limits the capacity for a prompt response from emergency teams. Furthermore, the necessity of repetitive measurements contributes significantly to the medical staff workload [55].

A solution that arises from all these limitations is automated continuous monitoring. This is one of the most essential components in intensive care medicine. Its implementation

leads to significant improvements in patient safety [61]. It allows insights into vital sign trends, and this can be much more informative and predictive than single deviating values [62]. In fact, in comparison to intermittent monitoring, the predictive value of continuous vital sign monitoring (VSM) is irrefutable. According to [59], continuous monitoring of heart rate, systolic blood pressure, and shock index are predictive of transfusion risk, and this predictive ability improves with the duration of monitoring. For instance, [63] found that the instability score derived from continuous monitoring predicted instability 9 minutes before standard intermittent monitoring, in 80% of cases.

As discussed in [59], secondary benefits from continuous monitoring also include cost savings from the reduced dependency of ICUs and shortened hospital stay. In fact, there is a highly positive return over investment (ROI) by implementing continuous monitoring systems. For instance, in the 5-year ROI model adopted in [64], it saved between $3,268,000 (conservative model) and $9,089,000. It was reported in [65] an estimated cost reduction of $28,195 per patient when using continuous monitoring. Due to reduced ICU transfers after implementing continuous monitoring at a 400-bed referral center in [66], the estimated annual cost reduction was $817,000 in the first year. And it was projected to reach $1,295,000 in subsequent years. Similarly, in [67], reduced ICU transfers lead to 367.11 saved ICU-days over a 2-year period. This resulted in estimated cost savings of more than $2.3 million.

Furthermore, biomedical signals are non-stationary in nature [68]. Besides reducing or, at least, averaging measurement errors, continuous monitoring enables proper and effective statistical diagnosis and trend analyses using the measured values. This will certainly improve the recognition of possible pointers to pathological conditions [17, 54].

However, continuous VSM is still limited to ICUs. It is commonly performed using expensive equipment with complicated setups. This requires a high staff-to-patient ratio which restricts monitoring only to the critical care environment. Less intrusive and accessible remote monitoring devices are thus needed. These new technologies have the potential to convey the advantages of continuous ICU-style VSM to general wards and even to the patient home [59].

1.1.5 To be continuous, contactless is needed

Conventionally, continuous monitoring of vital signs is achieved by contact-based sensors mainly using adhesive, electrodes, wires, and/or chest straps. Most existing physiological monitoring systems require multiple electrodes attached to the patient and connected by cables to display units. Although fixed-on-body electrodes usually provide good signal quality, there are several disadvantages to contact-based methods. And these limitations

FIGURE 1.5: Infants with irritant contact dermatitis reaction from medical adhesives; one caused by transparent adhesive dressing, the other from hydrogel for electrodes (adapted from [73] - with permission from Elsevier).

are mostly related to the need for direct contact between the sensor and the monitored subject. Most of the time, the measurement process can be annoying, unpleasant, or even inappropriate for specific groups of patients. This includes especially: neonates, infants, elderly, and burned patients [54].

Besides being unpleasant, long-term contact-based monitoring can lead to additional problems. Medical adhesive–related skin injuries (MARSI) is an underrecognized complication that is thought to impact at least 1.5 million people each year in the United States [69, 70]. For instance, injuries can occur while removing electrodes attached to the skin and may include the formation of vesicles, skin erosion, skin tears, epidermal stripping, or allergic dermatitis. Elderly patients are more susceptible to MARSI. With aging, the epidermis and the subcutaneous layers become thinner and more susceptible to mechanical forces. The blood vessels of the dermis also become more fragile, increasing the risk of bleeding underneath the skin [69].

Adhesive injury is also the most common source of skin breakdown[1] in Neonatal Intensive Care Units (NICUs) [71]. Existing neonatal monitoring systems have undergone little innovation over the past five decades, nearly all requiring a multitude of rigid sensors and accessories affixed to the neonate's skin [72]. And compared with adults, the skin of premature neonates is up to 60% thinner with substantially lower mechanical strength. Besides resulting in stress and pain, skin breakdown increases the risk of infection and, if large areas are involved, it can lead to fluid and temperature loss. As a consequence of using medical devices with associated adhesives, the incidence of skin breakdown in hospitalized neonates ranges from 31% to 45%. In smaller premature neonates, 15% of the entire body surface area can be traumatized daily [72]. Fig. 1.5 shows two infants with irritant contact dermatitis reaction from medical adhesives.

[1] also known as "pressure ulcer", it refers to a localized injury to the skin and/or underlying tissue, as the result of pressure, or pressure in combination with shear and/or friction.

In addition, the presence of cables also considerably limits mobility for the complete duration of the monitoring period [54]. Tethering patients for long periods increases the risk of venous thrombosis, sleep disturbance, functional decline, and delirium [72]. Wires and cables also reduce patient comfort, compromise the sustainability of the monitoring strategy [45], and can be a great barrier to the acceptance of VSM systems at the patient home.

Mobility restriction is also a problem for neonates. Monitoring cables represent a physical barrier to kangaroo mother care, a crucial lifesaving intervention for them. It was reported in [74] that kangaroo mother care reduces all-cause mortality by 40%, hospital-based infection by 65%, and hypothermia by 72%. In addition, it can result in clinically significant increases in weight, length, and head circumference growth for neonates [72]. Moreover, infants attached to monitors with leads and wires may be at higher risk of strangulation or entanglement, especially in situations such as bedding and transport. This represents a major patient safety issue [61].

Furthermore, the need for precise placement of electrodes requires a competent operator as misplaced ones may result in faulty recordings. Since trained staff is required, hospitalization periods can be extended and treatment costs increased. Monitoring performance may also be time-dependent due to the use of a conductive gel which can dry over time. Finally, the performance of contact-based devices is also affected by body movement artefacts [54].

The acquisition of vital sign information in a contactless manner can become a valuable tool in clinical healthcare applications, as well as in the non-clinical environment [54]. The contactless monitoring of the cardiorespiratory activity neither confines nor inhibits the patient, reduces hygiene risks, and does not cause any discomfort, irritation, or skin damage [15, 75]. This is especially important over extended periods of time and considering patients with sensitive skin. In an ideal measuring setting, the subject would not be aware of the measuring process itself, thus resulting in a decreased psychological factor. Besides eliminating several limitations of contact-based sensors, such contactless devices would therefore result in more objective readings [54].

The challenge of an aging population is pushing toward novel healthcare solutions, evolving from traditional hospital-based systems to a more person-centric approach where patients can be remotely observed in their homes [76]. This demand for ubiquitous monitoring is increasing not only in the medical field but also in several consumer applications, such as the automotive industry, psychology, security, and sports [54]. In order to provide continuous measurements in such diverse scenarios, one needs to rely on contactless devices.

1.1.6 Why using radars?

While the concept of contactless monitoring of vital signs has been demonstrated before the 90's [75, 77], recent research efforts are moving this technology toward low-power, light-weight, smaller, and cheaper devices [78]. Nowadays, a few technologies are still under investigation and approaching the market. Even though optical, WiFi and acoustic-based sensors have shown promising results [15, 50, 79, 80], camera and radar systems are, until now, the most adopted technologies [42].

The contactless monitoring of cardiorespiratory activity using cameras is mainly based on three different measured variables: body motion, temperature, and color.

Motion-based methods: When we breathe, the chest wall moves back and forth to allow the expansion and contraction of the lungs. Also, when the heart beats, the pulsating blood flow results in small skin displacements that can be seen in different parts of the body. These small movements can be detected by cameras, thus allowing the identification of inspiration/expiration and heartbeat cycles under certain conditions.

Thermal-based methods: The resulting airflow while breathing causes small temperature variations around the nostril. Similarly, when the heart beats, the pulsating body flow also changes the temperature around major superficial arteries. Specific cameras can be used to track these small changes in temperature, which also provide valuable information about respiration and heartbeat cycles.

Color-based methods: These methods rely on the detection of subtle skin color changes due to the cyclical movement of the blood. They are based on a similar principle as in conventional PPG sensors, however in a contactless way. This is why these methods are usually called remote photoplethysmography (rPPG) or imaging photoplethysmography (iPPG). As the cardiac activity is modulated by the respiratory activity, iPPG signals can also be used to detect breathing cycles [81].

Based on these principles, several camera-based systems for contactless VSM have already been proposed [82], spanning clinical and non-clinical applications, such as monitoring newborns, elderly, sleep, activity, and drivers [15]. A variety of cameras are being used, from advanced thermal or time-of-flight cameras [50] to simpler smartphone, laptop, or even web cameras [49].

However, camera-based systems have several limitations. They require that patients remain in the line of sight while being monitored. In fact, a direct view of the monitored

area is needed. Using blankets, for instance, can be a challenging situation [83]. In addition, the quality of the vital sign information is directly related to the quality and size of the extracted region of interest (ROI). Besides the challenge of precise ROI detection and tracking, image/video processing over large areas demands powerful computational capabilities. This can prohibitive when considering small devices with low computing resources [15].

Camera-based devices are also strongly affected by skin pigmentation and ambient illumination conditions [84]. In fact, any approach relying on cameras requires specific light conditions and can easily be interfered with by low illumination, smoke, or opaque obstructions [80]. Furthermore, these methods come at higher costs due to expensive devices, deployment, and maintenance overhead [76].

Perceived privacy is another important aspect, especially considering non-clinical deployment and sensitive environments, such as bedrooms and bathrooms [16]. For recording very rich and detailed information, any type of camera can be seen as privacy-invasive. Video recording and storage can also lead to safety and operational issues. These seem to be important obstacles to the wide adoption of this technology. Comprehensive reviews on camera-based methods for VSM can be found in [49, 82, 85, 86]

On the other hand, radars have already been proven to be a promising technology for contactless monitoring of vital signs [12, 16, 76]. Unlike camera-based systems [83, 87], radar signals can penetrate through different materials (such as plexiglass, clothing, mattresses, and blankets), and are not affected by skin pigmentation or ambient light levels [88]. Unlike wearable sensors, radar systems do not require users to wear or carry any additional equipment. People under observation do not need to wear/interact with any device, or even to comply with instructions that would change their routines [12]. Radar-based VSM has also advantages when considering its applicability in foggy, non-line-of-sight, and through-wall scenarios [11]. In addition, radar data preserve privacy as no images or videos are recorded [13]. Furthermore, radar devices can be low-power and low-cost, and they transmit no more power than a mobile phone.

These inherent characteristics have drawn the attention of the research community, and a variety of radar types are being used to address different healthcare and consumer applications, including sleep monitoring [89], life detection and rescue [90], assisted living [91], diagnosis [92], and many others.

With respect to the practical deployment of radar systems and market-related aspects (miniaturization, cost, and infrastructure), we are now moving from a research-based setting to a more practical and close-to-market validation. Despite not being as popular as cameras and wearables, the intense research and mass production from the automotive

industry is driving costs down [16], resulting in the large availability of compact and inexpensive radar modules, with increased capabilities and functionalities.

However, radar devices also have limitations. Due to the reduced transmitted power, radar signals can be easily buried in the background noise, or even masked by external interference, including additional body movements from the monitored patient [93]. This type of interference is a major challenge for accurate estimation in contactless solutions, as well as for contact-based devices. Specific signal processing techniques are thus needed in order to ensure reliable and robust measurements.

1.2 Contributions of this thesis

Despite a few recent works investigating more complex scenarios, *i.e.* multiple subjects [14], occasionally moving [93], and outside laboratory environment [94], most research on contactless VSM with radar sensors still focus on a single-person setup under ideal conditions. The subject is typically instructed to remain relatively motionless (sitting still or lying down), in a quiet environment, and in the absence of other moving objects [95].

Throughout our literature review, we identified the reasons behind this limitation are related to the lack of robustness in dealing with practical scenarios. Particularly, two problems deserve special attention: the additional random body movements (RBMs) from the monitored patient, and the harmonic interference from breathing over the heartbeat signal. Although the huge amount of recent work, validation is usually performed in idealized scenarios, where the subject is breathing calmly, and body movements are being emulated through predefined behavior.

At a higher level, these remaining challenges can be summarized into three research questions:

- **Question 1)** How to precisely recover the vital sign information from the tiny induced chest wall movements?
- **Question 2)** How to mitigate the effects of interfering components, especially RBMs from the monitored patient?
- **Question 3)** How to accurately estimate vital sign frequencies in different conditions, and particularly, how to estimate the heart rate under the harmonic interference from breathing?

In an effort to better understand and eventually answer these three questions, the main contributions of this thesis are threefold:

- **Contribution 1)** a new algorithm for recovering the chest wall movements from radar signals;
- **Contribution 2)** a novel random body movement and interference mitigation technique;
- **Contribution 3)** a robust and accurate heart rate estimation framework.

These contributions were tested under different operational conditions and scenarios, ranging from ideal simulation settings to complete validation with premature babies in a real NICU environment.

1.3 List of publications

The work presented in this thesis has resulted in two patent applications, and a number of peer-reviewed journal and conference papers, currently published or under revision. The publications related to this thesis are listed below.

Patents

- P1: "System and Method of RBM Mitigation for Vital-Sign Monitoring using Radar Systems" (filing number P-IEE-553/LU).
- P2: "Method and System for Vital Sign Monitoring" (filing number P-IEE-559/LU).

Journals

- J1: **G. Beltrão** et al, "Contactless radar-based breathing monitoring of premature infants in the neonatal intensive care unit", Sci Rep 12, 5150 (2022). DOI
- J2: **G. Beltrão** et al, "Adaptive Nonlinear Least Squares Framework for Contactless Vital Sign Monitoring", IEEE Transactions on Microwave Theory and Techniques (Early Access), 2022. DOI

Conferences

- C1: **G. Beltrão**, M. Alaee-Kerahroodi, U. Schroeder and M. R. Bhavani Shankar, "Joint Waveform/Receiver Design for Vital-Sign Detection in Signal-Dependent Interference", 2020 IEEE Radar Conference (RadarConf20), 2020, pp. 1-6. DOI
- C2: **G. Beltrão**, M. Alaee-Kerahroodi, U. Schroeder, D. Tatarinov, and M. R. Bhavani Shankar, "Nonlinear Least Squares Estimation for Breathing Monitoring Using FMCW Radars", 18th European Radar Conference (EuRAD), 2022, pp. 241-244. DOI
- C3: **G. Beltrão**, M. Alaee-Kerahroodi, U. Schroeder, D. Tatarinov, and M. R. Bhavani Shankar, "Statistical Performance Analysis of Radar-Based Vital-Sign Processing Techniques", Sensing Technology, pp. 101-112, Springer, Cham., 2022. DOI
- C4: **G. Beltrão**, T. Feuillen, M. R. Bhavani Shankar, M. Alaee-Kerahroodi, and U. Schroeder, "Unlimited Sampling for Radar-based Vital Sign Monitoring", invited paper at the Asilomar Conference on Signals, Systems, and Computers, 2022 (to be published).
- C5: **G. Beltrão**, "Contactless Radar-based Vital Sign Monitoring", European Signal Processing Conference (EUSIPCO), 3 Minutes Thesis (3MT) competition: Runner-up, 2022.

Publications not included in this thesis

The following publications, also carried out in the context of the Ph.D. work, were not included or referenced in this thesis.

- C6: **G. Beltrão**, L. Pralon, M. Alaee-Kerahroodi and M. R. Bhavani Shankar, "Sidelobe Performance Analysis of Noise Waveforms Considering the Doppler Mismatch", 2020 21st International Radar Symposium (IRS), 2020, pp. 192-196. DOI
- J3: **G. Beltrão**, L. Pralon, A. Barreto, M. Alaee-Kerahroodi and M. R. B. Shankar, "Subpulse Processing for Unambiguous Doppler Estimation in Pulse-Doppler Noise Radars", in IEEE Transactions on Aerospace and Electronic Systems, vol. 57, no. 6, pp. 3813-3826, Dec. 2021. DOI
- J4: L. Pralon, **G. Beltrão**, A. Barreto and B. Cosenza, "On the Analysis of PM/FM Noise Radar Waveforms Considering Modulating Signals with Varied Stochastic Properties", Sensors, 21(5), pp. 1727. DOI

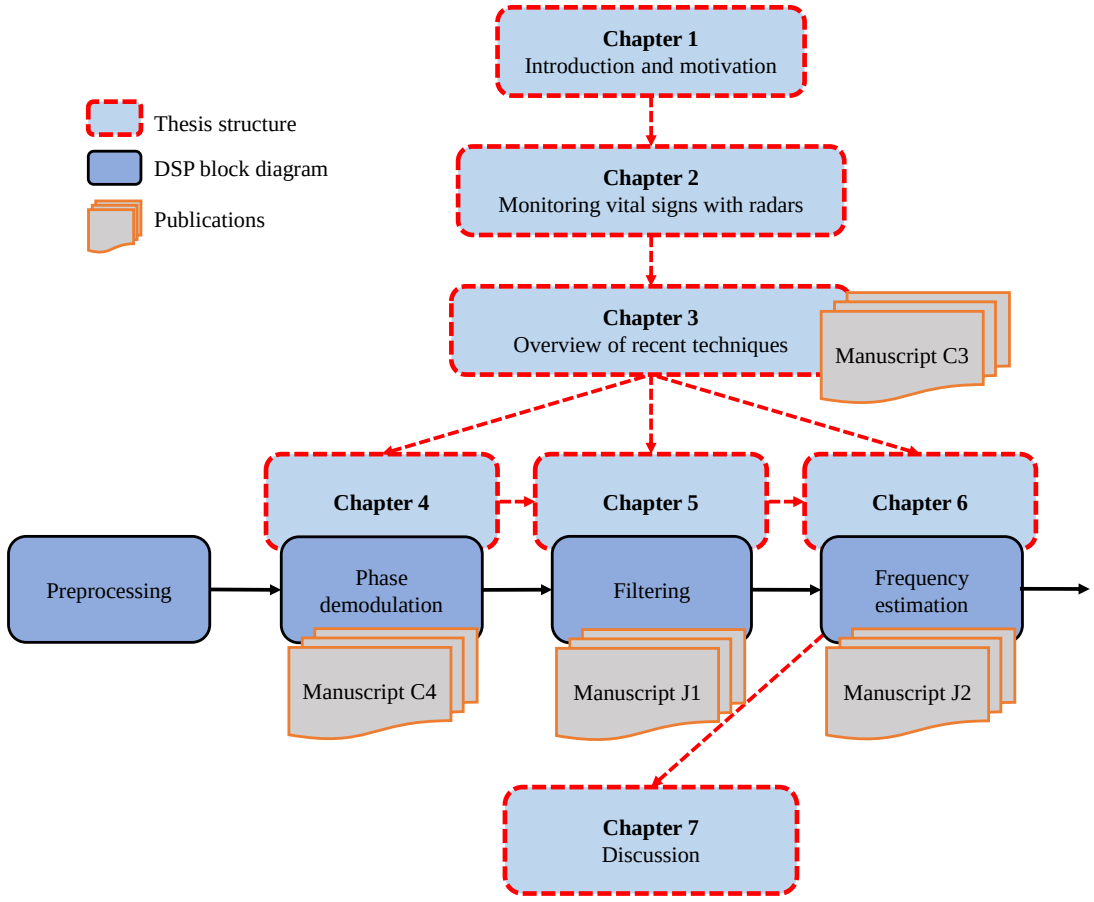

FIGURE 1.6: Thesis organization and basic DSP block diagram for contactless monitoring of vital signs.

1.4 Thesis organization

This thesis is a "thesis with publications". It includes four manuscripts reproduced in their entirety. While the first one (**C3**) is part of our literature review, the other three (**C4**, **J1**, and **J2**) present our contributions to improving the state of the art. Despite describing complete signal processing solutions in each one of them, the major contribution in each manuscript is related to a particular stage of the basic DSP block diagram for contactless monitoring of vital signs. Therefore, each chapter/manuscript addresses one or more challenges related to this block. Fig. 1.6 shows the thesis structure, including the basic DSP block diagram. The manuscripts have been listed in Section 1.3. A more detailed description of each stage in the block diagram will be provided in the next chapter. In summary:

- Chapter 2 is the first part of our literature review. It provides an introduction and overview of many concepts related to the contactless monitoring of vital signs

using radars, and also presents the state of the art in terms of signal processing techniques for enabling this technology.

- Chapter 3 is the second part of our literature review. Here we present our first manuscript. It complements the previous chapter by providing a simulation framework and selected results that allow to analyze and compare existing signal processing techniques for radar-based monitoring of vital signs.

- Chapter 4 looks into the phase demodulation block. In this chapter, we present our second manuscript, with a new algorithm for robust recovery of the chest wall motion from radar data. It greatly extends the resilience of the recovery process if compared to conventional methods. This is the **Contribution 1** of this thesis.

- Chapter 5 addresses the filtering stage and one of its main challenges: how to deal with random body movements from the monitored subject. In this chapter, we present a manuscript that shows our work at the NICU, where we monitored premature babies in a real clinical environment. This work is the **Contribution 2** of this thesis and led us to the first patent application (**P1**).

- In Chapter 6 we focus on the frequency estimation block. Here we present the last manuscript, in which we proposed a novel algorithm to mitigate the effects of the harmonic interference from breathing over the heartbeat signal. In this case, the validation was performed with real data collected while imitating common working conditions in an office environment. This work is the **Contribution 3** of this thesis and resulted in a second patent application (**P2**).

- Finally, in Chapter 7 we finalize this thesis by summarizing and connecting the relevant aspects of our contributions, and discussing what remains as interesting research avenues.

Each chapter with a manuscript also contains a preamble. It aims to guide the reader along the thesis, by introducing the general topic and establishing a smooth connection between the current chapter and the rest of the thesis.

The manuscripts included in each chapter are presented as published or submitted for consideration. A few formatting aspects have been adjusted to match the rest of the thesis. All pages, tables, equations, and figures have been numbered consecutively throughout the thesis for continuity. All references were consolidated into a single reference list, presented at the end of this thesis.

Please note that each manuscript presents its own notation and the used terms may differ in each chapter.

1.5 Support

This work was supported by the Luxembourg National Research Fund (FNR), under the FNR Industrial Fellowship Grant, project MIDIA, Reference 14269859. This project is a partnership between the University of Luxembourg's Interdisciplinary Centre for Security, Reliability and Trust (SnT), and IEE S.A.

The support for data collection at the hospital was provided by the Department of General Pediatrics and Neonatology, from the Saarland University Medical School, in Homburg, Germany.

Chapter 2

Monitoring vital signs with radars

2.1 Operating principle

The activity of the cardiovascular and respiratory systems causes some physical and physiological effects on the human body. The chest moves during the inspiration/expiration cycle as a result of the diaphragm and intercostal muscle movements. The volumetric changes in the heart muscle due to pumping blood through the circulatory system can also be transmitted to the chest leading to a subtle movement. These small and periodic displacements can be detected by radar, allowing accurate estimation of the breathing and heart rates under certain conditions.

Fig. 2.1 shows the basic operating principle for monitoring vital signs in a contactless way using radars. When we breathe, or when the heart beats, the subtle motion at the chest wall surface modulates the transmitted radar signal, which is reflected with additional phase information regarding this movement. The received signal can thus be modeled as a scaled and time-shifted version of the transmitted signal, in which the phase variation over time contains the desirable vital sign information. This time-varying phase $\theta(t)$ is usually modeled as

$$\theta(t) = \frac{4\pi d(t)}{\lambda}, \tag{2.1}$$

where λ is the radar operating wavelength, and $d(t)$ represents the displacement signal which, ideally, would correspond only to the chest wall movements due to breathing and heartbeat. As seen by the radar, these movements are mainly originated by the reflected points over the chest moving surface, but it may additionally include residual motion from the belly, shoulders, sides, and also from the back [96, 97].

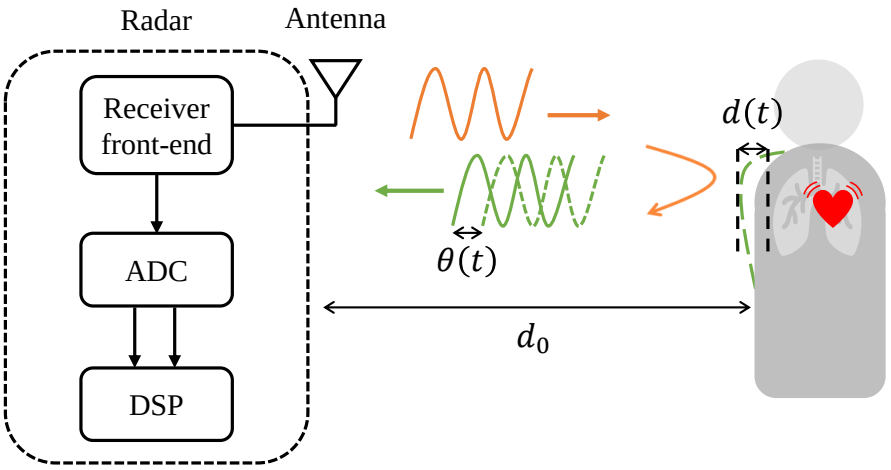

FIGURE 2.1: Contactless VSM with radars: operating principle.

The radar receives the reflected signal and, after analog-to-digital conversion, tries to reconstruct the chest wall motion by using DSP techniques. Perfect recovery of the chest movement would allow precise estimation of breathing and heartbeat frequencies by simple analysis of the signal's periodicity. However, in practical applications, besides unavoidable hardware imperfections, the received radar signal is usually mixed with additional reflections from the external environment, arising not only from different body movements of the monitored subject but also from every object in the radar's field of view. These interfering signals are usually much stronger than those induced by the chest wall millimeter displacement, and this makes accurate recovery and subsequent estimation of the breathing and heartbeat frequencies a challenging task.

2.2 The chest wall displacement signal

The chest wall displacement signal is usually modeled as a superposition of both breathing and heartbeat movements. Simplistically, it could be expressed as

$$d(t) = d_{\mathrm{b}}(t) + d_{\mathrm{h}}(t), \tag{2.2}$$

where $d_{\mathrm{b}}(t)$ represents the displacement due to the breathing movement, and $d_{\mathrm{h}}(t)$ represents the displacement due to the heartbeat movement. Both motions can be assumed to be periodic but with different ranges of amplitudes and frequencies (spectral content).

Pure sinusoidal models have been extensively applied for modeling both breathing and heartbeat displacement signals [78]. This simple assumption is based on the Fourier theory, which states that any time-varying periodic signal can be represented as a

superposition of weighted harmonic sinusoids. Usually, in the most simplistic model, both signals are assumed to have a single dominant frequency and, in this case, $d_{\mathrm{b}}(t)$ and $d_{\mathrm{h}}(t)$ can be written as

$$d_b(t) = a_{\mathrm{b}} \cos(2\pi f_{\mathrm{b}} t), \tag{2.3}$$

and

$$d_h(t) = a_{\mathrm{h}} \cos(2\pi f_{\mathrm{h}} t), \tag{2.4}$$

where a_{b} and a_{h} are the amplitudes of the chest wall movement, whereas f_{b} and f_{h} are the associated frequencies corresponding to the breathing and heart rates. Despite their simplicity, these models are widely used [98, 99].

It is important to clarify that, in relation to the heartbeat displacement signal, what the radar "sees" and what is being modeled is not the actual heart movement, but the resulting residual movements at the chest wall surface, *i.e.* the precordial movements[1]. At the operating frequency of 24 GHz for instance, there is almost no penetration of radiation into the body. In fact, typically the skin will reflect around 73% of the incident wave, with the rest of the energy being quickly dissipated in the first millimeters of the body [100].

More complex patterns have also been already proposed for the displacement signal. In [101], the breathing chest wall movement is modeled as a symmetric bell-like shaped curve. Alternatively, in [28], it corresponds to a low-pass filtered periodic sequence of quadratic inspiration and exponential expiration. There are also studies using camera-based systems to model breathing movements by tracking markers distributed along the chest wall surface [102]. Finally, electromagnetic models and motion kinematics can also be used for approximating the displacement signal during complex movements as suggested in [103].

A Gaussian pulse train can be used for modeling the heartbeat, based on the idea that the heartbeat is a short explosive motion, with a pulsatile nature [104]. In [105], periodic exponential pulses are low-pass filtered by a (critically damped) second-order Butterworth filter. A more realistic model uses recorded signals from a seismocardiogram (SCG) sensor. These sensors measure the accelerations on the chest wall produced by the myocardial movements of the heart [106]. By taking the double-integral of the SCG signal, the chest wall displacement due to the heartbeat can be derived [107].

[1]Precordial impulses are pulsations originating from the heart or great vessels that are visible or palpable on the anterior chest wall.

Substituting (2.2) in (2.1) implies the underlying assumption that the monitored subject and its moving parts can be modeled as a single-point scatter. This is equivalent to assuming that, when we breathe, or when the heart beats, the moving parts of the body have the same reflectivity, i.e. the same radar cross section (RCS). However, a few studies have shown that the manifestation of these vital signs is distributed differently over the body [108]. In fact, the resulting RCS of the breathing movement is consistently and significantly larger than the one corresponding to the heartbeat [109], which is rather intuitive. More recent models [101] are trying to exploit these differences in order to obtain more realistic patterns for breathing and heartbeat movements.

It is important to mention that when we breathe, or when the heart beats, the resulting body movements are the manifestation of a complex physiological phenomenon. It is unlikely that any model could fully characterize it for every person in every situation. As discussed in [105], these models are highly idealized and not intended to be used as rigorous physiological models, but merely to capture the essence of these signals and to allow easy testing of signal processing algorithms.

This also seems to be the reason why most of the proposed processing techniques in literature are model agnostic and, therefore, the presented models are mostly used for illustrative purposes. However, regardless of the displacement signal shape, its spectral structure (frequency content) is mainly determined by its inherent periodicity. This spectral structure will be further explored throughout this thesis to improve estimation performance as we will show in subsequent chapters.

2.3 Radar frequencies and devices

As discussed in Section 1.1.6, a multitude of radar types is being used to address different applications. To comply with these different scenarios, a wide range of radar frequencies have already been used.

While using a lower operating frequency improves electromagnetic penetration and allows easier extraction of the displacement signal, higher frequencies result in better phase sensitivity and increased target reflectivity [13]. Frequencies generally used for radar-based VSM start from as low as 2 GHz and go up until 230 GHz [78]. Most research is still focused on frequency bands below 30 GHz, and especially around 24 GHz [110]. This includes industrial, scientific and medical (ISM) bands, which allow worldwide unlicensed operation under specific conditions.

However, regulatory authorities have recently decided that the 24-GHz wideband will be phased out for radar operation in Europe and in the United States [110]. These new

restrictions, and the need for high performance in emerging radar applications, are now moving research and industry toward mm-wave operation. At this region, the wider bandwidth significantly increases range resolution and accuracy, which drives the better separation of objects and improves tracking and classification. Another benefit of higher operating frequencies is the small form factor of devices. For the same antenna gain and field of view, the antenna size of a 79-GHz device can be reduced to approximately one-third if compared to 24-GHz systems. Alternatively, for the same antenna size, mm-wave operation results in narrow beamwidth which increases directivity and improves the signal-to-noise ratio (SNR).

In relation to the radar's waveform, Continuous-wave (CW) radars are usually being employed for VSM [54, 78, 111]. These devices have the advantages of low transmitted power, simple hardware structure, and high sensitivity. This explains their widespread use across various areas. Within this group, unmodulated CW systems, also called Doppler radars, have the simplest architecture. Due to the transmission and reception of a simple constant-frequency signal, the radio frequency (RF)-chain is greatly simplified and no synchronization mechanism is required.

However, the transmission of an unmodulated continuous signal with no timing information implies that no distance (range) information is acquired. Besides not being able to estimate the range of the monitored subject, other moving objects at different distances may interfere with the unmodulated CW signal, making it more difficult to isolate and extract the desired vital sign information [13].

For being able to estimate the distance of the monitored subject, typical approaches use ultrawideband (UWB) [11], frequency-modulated continuous-wave (FMCW) [76], stepped-frequency continuous-wave (SFCW) [13], or phase-modulated continuous-wave (PMCW) [112] radars. Recently, the application of millimeter-wave FMCW radars to short-range VSM has been extensively investigated [12, 16, 42, 111, 113]. These devices are being widely used in the automotive industry, which is constantly improving this technology and driving costs down. Such radars benefit from high range resolution and Doppler sensitivity, yet with simple architecture, that allows using relatively simple circuits and low-cost analog-to-digital converters (ADCs) [113].

There are several options already available in the market, from different manufacturers, and spanning frequencies usually from 60 GHz to 79 GHz. A few examples include the AWR and IWR families from Texas Instruments [114], and the BGT family from Infineon [115]. Despite the small form factor, large bandwidth and several transmit/receive channels are usually available, thus conferring high range resolution and multiple-input multiple-output (MIMO) capabilities. Such devices can be already fully integrated into

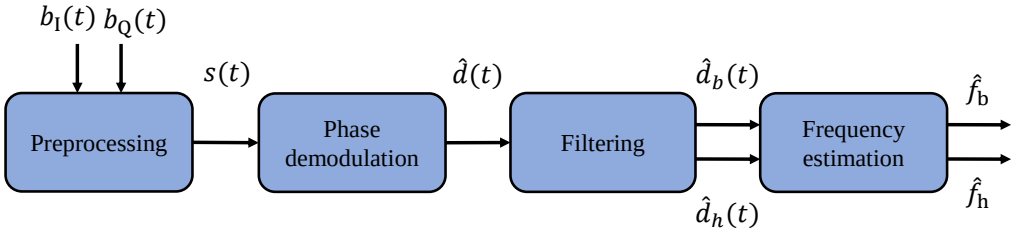

FIGURE 2.2: Basic DSP block diagram for contactless monitoring of vital signs. The flow of signals is now highlighted.

evaluation boards containing not only the antenna and radar front-end, but also built-in processors and a set of interfaces for configuration, control and data extraction.

2.4 Basic signal processing

The signal processing framework for contactless VSM using radars can be divided into four main parts: preprocessing, phase demodulation, filtering, and estimation. Figure 2.2 shows again the basic signal processing block diagram, now highlighting the flow of signals into the signal processing chain.

The following sections contain an overview of the basic signal processing steps for enabling the contactless monitoring of vital signs using radars. More detailed information, including the relevant equations considering CW and FMCW systems, will be provided throughout the manuscripts in Chapters 3, 4, 5, and 6.

2.4.1 Preprocessing

The preprocessing block receives the complex baseband radar signals as in-phase and quadrature samples ($b_{\mathrm{I}}(t)$ and $b_{\mathrm{Q}}(t)$) from the ADCs. Its main function is to detect and extract the signal $s(t)$ corresponding to the monitored subject.

For simpler single-channel CW radar systems (no range or angle processing), the input ADC signal already contains all the information relative to the radar's field of view. In this case, the detector can be directly applied over this signal, just to identify the moments where the chest wall movements are present.

For modern FMCW or PMCW systems with several receiving channels, the desired vital sign information is embedded in the slow-time signal, at a specific range and angle position where the target (monitored subject) is located. The received signals corresponding to each transmitted pulse are stored to create the radar data cube, which has temporal

dimensions corresponding to fast-time and slow-time. Using different antenna elements, the radar signal is also sampled spatially, thus generating an additional dimension along the receiving ADC channels. The total duration of the collected fast-time samples corresponds to the duration of the transmitted pulse, whereas the total duration of the slow-time samples corresponds to the coherent processing interval (CPI). Similarly, the size of the spatial dimension corresponds to the antenna size or aperture.

Particularizing to FMCW systems, as illustrated by Fig. 2.3, a two-dimensional discrete Fourier transform (DFT) is usually performed over the radar data cube, across fast-time and ADC dimensions. This corresponds to an approximation of the matched filter operation, in the sense of being the linear filter that maximizes the target SNR in presence of additive noise. This operation also translates the fast-time dimension into frequency (beat frequency), which in turn is directly related to the target's range information. Similarly, the ADC dimension is translated into the angle, corresponding to the target's azimuth or elevation information.

Thus, in the next step, the detector should identify the range/angle cells (bins) where the target is present, *i.e.* where the chest wall movements can be detected. After detection, the slow-time signal at the target range/angle bin is finally extracted and will be further processed for phase demodulation and estimation.

Considering the simplistic scenarios where most solutions are usually validated (single static target, at short-range), simple amplitude, energy, or constant false-alarm rate (CFAR) detectors are commonly employed. In this case, most of the techniques used at the preprocessing block will be classic radar signal processing methods, with no specific adaptation for processing vital signs.

Recent research is approaching new detection techniques more tailored to the VSM application. Particularly, considering dynamic scenarios where one of the monitored subjects can be breathing still (i.e., no translational movement in relation to the radar), conventional clutter (zero-Doppler) filtering cannot be applied as it may also prevent vital sign detection from non-moving subjects. In addition, when operating at higher frequencies with large bandwidth, the human body may become an extended target, with vital sign energy being spread over several adjacent range bins. In these cases, just selecting the range/angle bins with maximum amplitude/energy may not be optimal.

2.4.2 Phase demodulation

The phase demodulation block aims to recover the chest wall movement over time. It is essentially the process where the complex samples from $s(t)$ (corresponding to

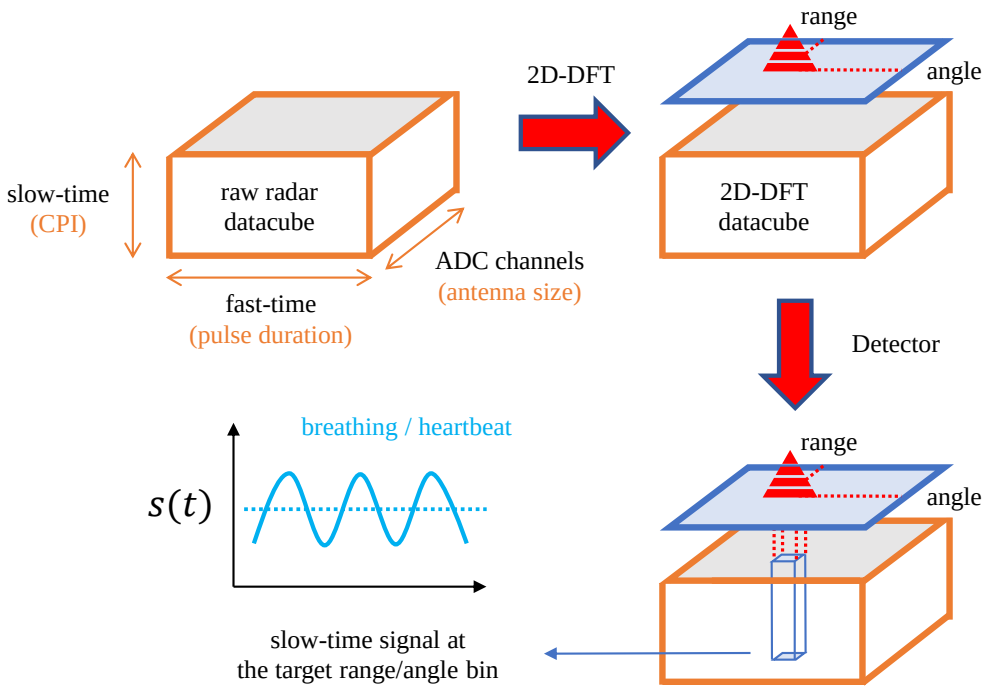

FIGURE 2.3: Preprocessing steps for FMCW systems.

the reflected signal from the monitored subject) are combined to obtain the recovered displacement signal $\widehat{d}(t)$ (an approximation of the true displacement $d(t)$).

For providing sufficient SNR, while still preserving the update rate, the phase demodulation and the subsequent steps for vital sign processing are commonly performed using overlapped sliding windows. This strategy leaves sufficient time to acquire several breathing/heartbeat cycles, revealing (and enhancing) the periodicity of the movement. Hence, the obtained frequency value from each processing window corresponds to an average over the window duration. In addition, the frequency resolution is also improved. In order to provide new estimates every one or two seconds, large overlaps are usually employed.

Among several methods, the two most used are the complex-signal demodulation (CSD) [116] and the arctangent demodulation (AD) [117]. The CSD was first proposed to eliminate the optimum/null detection point problem, which was very common when operating with former single-channel receivers [118]. With the advent of modern quadrature receivers, the resulting I and Q channels ($b_{\mathrm{I}}(t)$ and $b_{\mathrm{Q}}(t)$) could be combined in baseband, thus providing optimum detection irrespective of the target distance. The CSD relies on the small-angle approximation ($\sin(x) = x$) [119] to recover the chest wall motion. Despite generating intermodulation products and higher order harmonics [120], for small displacements (in relation to the operating wavelength), the recovered signal $\widehat{d}(t)$ will be a good approximation of the true chest wall movement $d(t)$, and the relevant

frequency content will be preserved. Therefore, the CSD is mostly used at lower operating frequencies.

On the other hand, the AD can be used for precise phase recovery. As the name implies, it uses an arctangent operation to directly recover the input signal phase. An additional unwrap operation is necessary for removing possible phase discontinuities caused by the bounded image of the arctangent function. This operation is very sensitive to noise and interference, and may eventually accumulate errors, resulting in large distortions in the recovered displacement signal. In Chapter 4 we will further analyze this problem and present a novel solution for recovering the chest wall displacement.

Before extracting the desired phase information, possible direct current (DC) offsets must be compensated. Despite the high range resolution provided by FMCW devices, DC terms originating from other sources (other than the actual chest wall movement) may eventually be present in the target range bin and should be compensated. Given that the ideal chest wall (back-and-forth) movement describes an arc in the I/Q plane, this compensation is usually accomplished using an ellipse fitting algorithm. A detailed description of the AD, with an extensive review of DC offset calibration strategies, can be found in [117] and [121], respectively.

To avoid the aforementioned limitations, the so-called differentiate and cross-multiply (DACM) demodulation has also been proposed [120]. The DACM calculates the derivative of the arctangent function, followed by an integration step for recovering the phase. In its extended version, it can be efficiently implemented in a discrete form where the differentiation is approximated by a forward difference, and the integration is replaced by an accumulation. Finally, the so-called linear demodulation (LD) can also be used. It tries to suppress redundant information, by maximizing the variance of the input signal [4]. It is based on the principal component analysis (PCA) of the input matrix where its first principal component is used as the demodulated signal. As discussed in [122], these methods suffer from intermodulation products and higher-order harmonic interference when working at higher operating frequencies.

2.4.3 Filtering

The filtering block is responsible for improving the signal-to-interference-plus-noise ratio (SINR) before estimation. The idea is to attenuate the system's noise and try to eliminate any interfering components still present in the demodulated signal.

This includes one of the main challenges in monitoring vital signs: how to filter out the interfering effects of RBMs. In practical monitoring situations, the subject may often move

body parts like hands, legs, or torso, and even the entire body. The amplitude of these reflected signals is often much stronger than the millimeter-scale chest wall motion, which will potentially be masked by this interference. Since spontaneous RBM are inevitable, solving this problem is fundamental to reliable VSM in practical applications. In addition, in a real home or clinical environment, multiple moving objects (and additional people) will often be present, generating even large motions which may further interfere with the intended monitoring.

A lot of effort has already been devoted to RBM mitigation [123]. Several methods were proposed in the literature, and even though specific types of movements could be effectively canceled out, they usually require more complex systems. Most of the existing solutions rely on extra or duplicated hardware, thus suffering from practical limitations such as misalignment, synchronization, and cost [124]. This has limited the application of these techniques in practical environments. Solutions with a single and simple device that can reliably recover the vital-sign information under RBM scenarios are still rare.

Another direction of research basically tries to identify segments of vital sign data with RBMs, and simply discard these corrupted segments before estimation [94, 125–128]. However, depending on the processing window length and overlap, even very short RBMs may affect several seconds of a good signal. Therefore, rather than simply discarding segments of data, an approach that allows useful exploitation of these episodes with moderate RBMs is desired. In Chapter 5 we will present our contribution to the RBM problem. Particularly, rather than just discarding measurements under strong interference, we developed a novel random body movement mitigation technique based on the time-frequency decomposition of the recovered signal.

For enhancing the SNR of the displacement signal, several approaches were already investigated. For instance, many proposals are using autocorrelation-based methods [4, 104, 129]. The heartbeat signal can also be improved by calculating the derivatives of the displacement signal [107]. In [124], a matched filter approach was used with good performance under certain conditions.

Finally, in the filtering block, the displacement signal is also separated into the breathing and heartbeat components. In this way, the estimation can be performed independently on each of them. While simple bandpass filters are commonly used, recent works are exploiting more powerful separation techniques. Some examples include the independent component analysis (ICA) [130], the empirical mode decomposition (EMD) [131] and its variants - the ensemble empirical mode decomposition (EEMD) [132] and the complete ensemble EMD with adaptive noise (CEEMDAN) [133] -, the variational mode decomposition (VMD) [134], the nonnegative matrix factorization (NMF) [135], and the empirical wavelet transform (EWT) [136].

The filtered signals $\widehat{d}_{\mathrm{b}}(t)$ and $\widehat{d}_{\mathrm{h}}(t)$ will ideally be a good approximation of the true chest wall motion due to breathing and heartbeat, respectively, and can finally be used for frequency estimation.

2.4.4 Frequency estimation

The frequency estimation block is responsible for detecting the breathing/heartbeat cycles and calculating their period, or alternatively, for directly estimating the dominant frequency in which they occur, i.e. the breathing and heart rates.

After phase demodulation and filtering, the displacement signals will ideally contain only the periodic chest wall movements due to the breathing ($\widehat{d}_{\mathrm{b}}(t)$) and heartbeat ($\widehat{d}_{\mathrm{h}}(t)$). As the name implies, the aim of this block is to finally estimate the fundamental frequencies $\widehat{f}_{\mathrm{b}}$ and $\widehat{f}_{\mathrm{h}}$, which correspond to the breathing and heart rates, respectively. This is a well-known problem from spectral analysis, in which solutions can usually be categorized into parametric and non-parametric methods. The latter includes subspace techniques [137, 138], maximum likelihood [139, 140], and Bayesian estimation [141]. While these methods improve frequency resolution and thus estimation accuracy, they are computationally more complex than non-parametric methods [142]. In addition, the good performance of parametric techniques relies on some degree of certainty about the underlying models that generated the data. This can be an issue when considering the complexity behind the resulting chest/belly/shoulders movements when breathing or when the heart beats.

Besides their simplicity, non-parametric methods are known to be more adaptive in practical applications [143]. Several approaches have been recently proposed, based on different techniques such as wavelets [136, 144], the chirp Z-transform (CZT) [145, 146], the DFT [107, 147], the quadrature cosine transform (QCT) [148], and the short-time Fourier transform (STFT) [129, 149]. Among these, simple DFT-estimation is the most used [11]. In this case, the frequency estimates correspond to the locations of dominant peaks in the corresponding spectrum of the displacement signal. While this may be sufficient for accurate breathing rate estimation in quasi-ideal conditions, *i.e.*, without additional interference, it may not provide good results when considering more practical scenarios, especially for the heart rate estimation.

It is important to mention that DFT-based methods suffer from low-frequency resolution due to smearing and leakage problems caused by the limited data length. However, using longer processing windows to improve resolution may prevent the detection of relevant time-varying characteristics of the vital signs. While this can be an issue for specific applications, *e.g.* diagnosis, for long-term monitoring, the overlapped sliding

window approach can usually provide a good compromise between resolution and update rate. More recent approaches to overcome the frequency resolution issue include sparse reconstruction, stepwise atomic norm minimization, and the synchrosqueezing transformation [12].

Finally, the frequency estimation block should also deal with residual interfering components which were not properly filtered by previous processing steps. This is especially important when considering heart rate estimation. In many cases, the harmonics from the breathing signal overlap spectrally with the fundamental frequency component of the heartbeat signal. In this situation, the estimator should implement additional mechanisms to avoid wrong estimates originating from harmonic-interfered spectral regions.

In Chapter 6 we will present our contribution to the Frequency Estimation block, where we proposed a novel estimation framework to overcome the aforementioned challenges. In this case, we validated our solution with real data collected while imitating common working conditions in an office environment.

2.5 Simulation framework

As part of our preliminary study and literature review, we developed a simulation framework and an easy-to-use graphical user interface (GUI) using Matlab.

The idea was to explore existing models of the chest wall displacement signal and use them to generate simulated radar data in different operational conditions. Further, by processing these signals, we would be able to investigate the effects of different parameters, and also to compare existing signal processing techniques for radar-based VSM.

The GUI is divided into three screens, which will be described below:

- The first screen controls the signal generation. It is possible to define several simulation parameters, including the sampling frequency of the ADC, the radar operating frequency, the input SNR, the simulation time, and the duration of the generation window. In addition, it is also possible to emulate hardware imperfections in the form of I and Q channel imbalances (DC, amplitude, and phase offsets). The breathing and heartbeat displacement signals can be configured by choosing the corresponding models, the amplitude, and the range of frequencies. For instance, the user can select between sinusoidal models for both breathing and heartbeat, or the model from Albanese [28] for breathing, and the model from Nosrati [104] for the heartbeat. Finally, the plots allow visualizing of the generated data and its main properties. Fig. 2.4 shows the signal generation screen.

- The second screen is dedicated to signal processing and the obtained results. In this screen is possible to set up basic processing parameters (sampling frequency, duration, and overlap of processing windows), as well as the phase demodulation and specific techniques for filtering and enhancing the breathing and heartbeat signals. For instance, one can configure preprocessing techniques, bandpass filters, and/or estimation methods. After processing using the selected parameters and techniques, the figures show the obtained performance for both breathing and heart rate estimation, where the threshold intervals for the accuracy calculation can also be independently set up. Fig. 2.5 shows the signal processing screen.

- The third and last screen is a debug tool that shows the obtained results at each step in the signal processing chain. It includes the I/Q raw data, the recovered displacement after phase demodulation, the filtered displacements, and the corresponding frequency spectrum. It allows easy visualization if something is not working properly, and also helps to understand the effects of using different techniques. Fig. 2.6 shows the debug screen.

A selection of some results obtained with this tool was included in manuscript **C3**, which will be presented in Chapter 3.

2.6 Some experimental results

The first part of our experimental study was performed using devices that emulated controlled targets. These devices could be programmed for executing breathing-like movements, representing the chest wall displacement over time. The objective was to select appropriate phase demodulation algorithms and parameters, in order to precisely recover the displacement signal. Finally, human tests were performed in the laboratory, aiming to validate the complete signal processing chain.

For these experiments, we used a Texas Instruments (TI) mm-wave FMCW radar (AWR1642 [150]), operating at 77 GHz, with a 4 GHz bandwidth. As we are only considering single-target scenarios, the radar is configured for using a single transmit and receiver antenna. The total duration of each chirp was 64 μs, with an inter-frame period of 10 ms, corresponding to a slow-time sampling frequency of 100 Hz.

The following subsections will describe each scenario and present some of the obtained results.

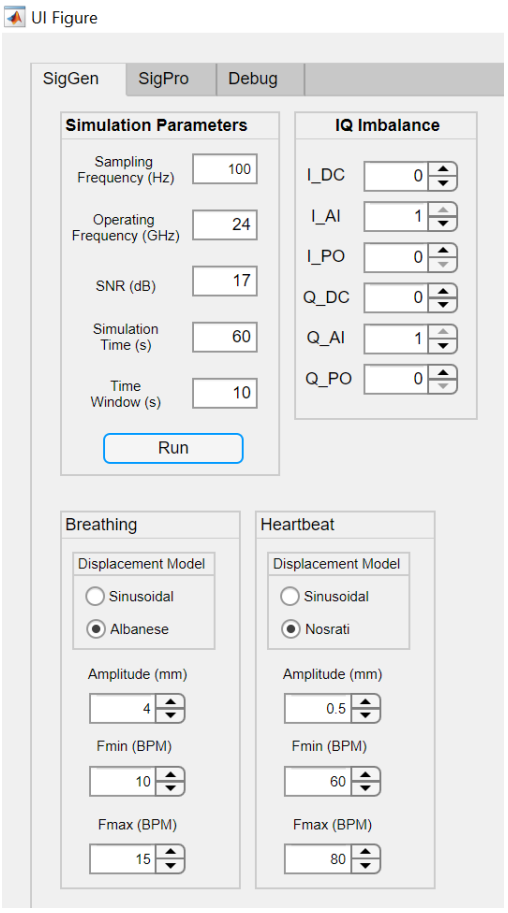

(a) Parameters for signal generation.

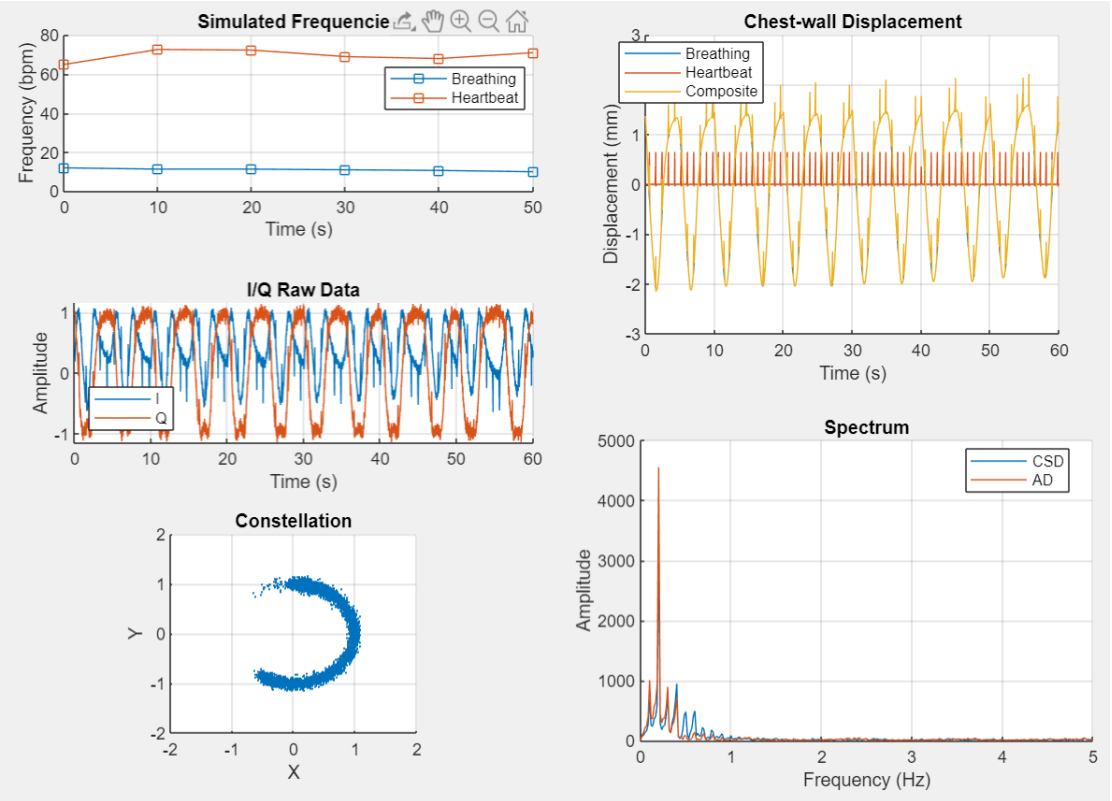

(b) Plots of the generated signals.

FIGURE 2.4: Matlab GUI: signal generation screen.

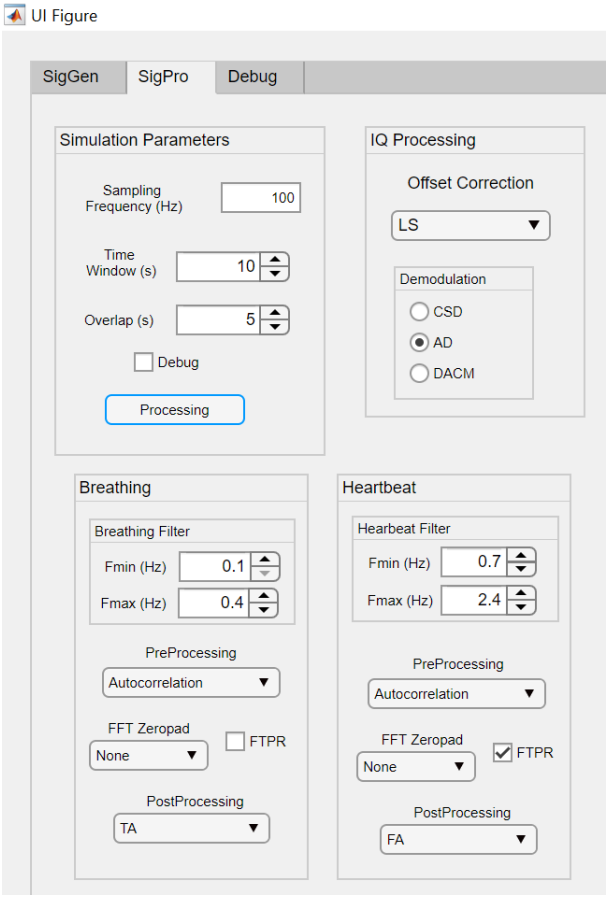

(a) Processing parameters.

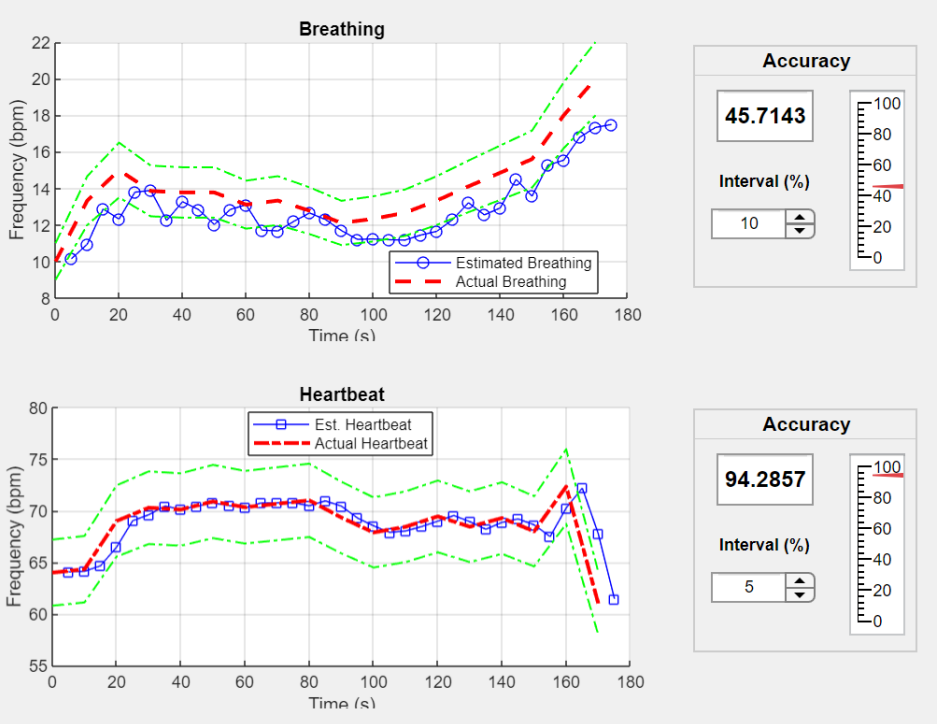

(b) Obtained results.

FIGURE 2.5: Matlab GUI: signal processing screen.

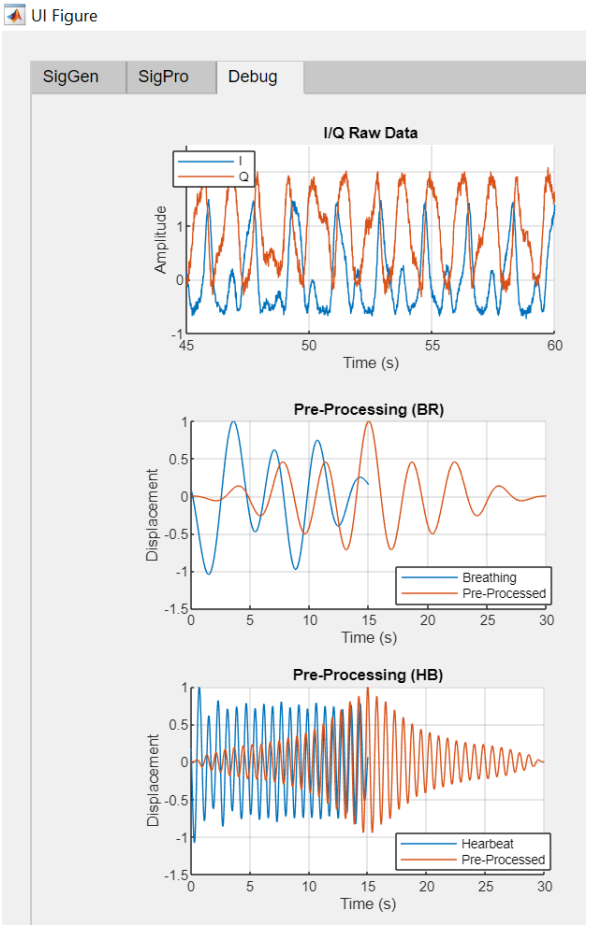

(a) Raw data and preprocessing.

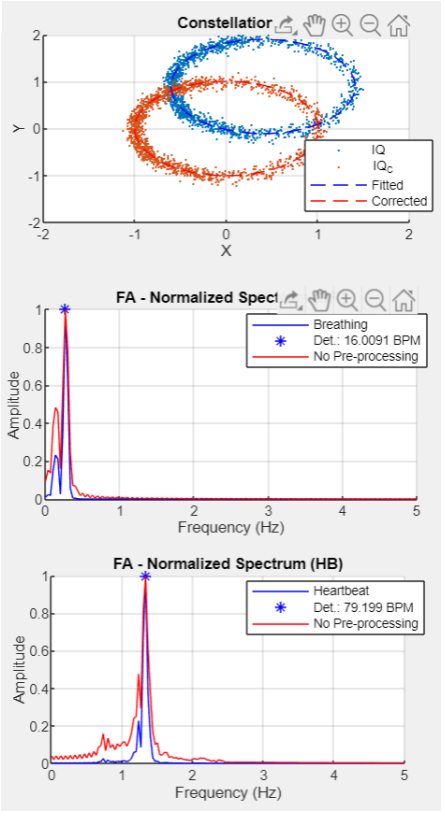

(b) Constellation and frequency analysis.

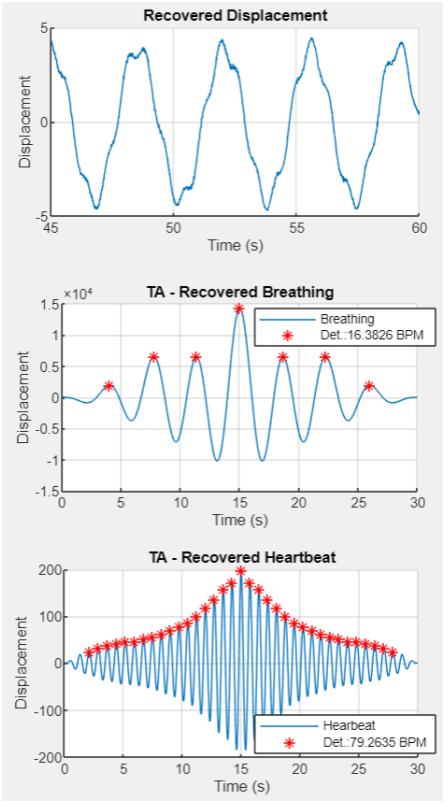

(c) Displacement and time analysis.

FIGURE 2.6: Matlab GUI: debug screen.

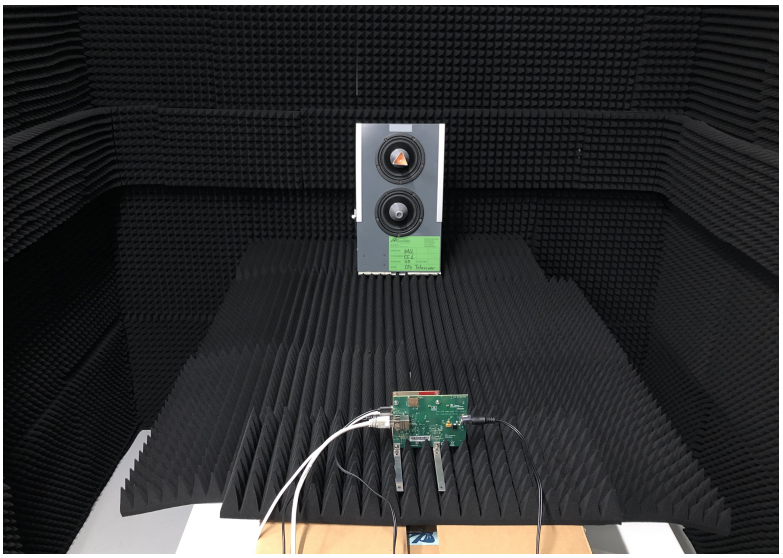

FIGURE 2.7: Setup for the tests with the speaker.

2.6.1 Speaker tests

The first set of tests was performed using a double-speaker prototype device, configured for executing a periodic movement, with control of its amplitude and vibration frequency. In this way, it is possible to emulate the amplitude and periodicity (frequency) of the chest wall movements from a single-scatter target. For providing ground-truth information regarding the actual movement, we used the optoNCDT 1320 [151] laser displacement sensor. The speaker was mounted just in front of the radar, at a distance of 1.5 m. The proposed setup can be seen in Fig. 2.7.

For these initial tests, we used only one of the speakers and placed a small corner reflector attached to its dust cap. It was configured for executing a periodic back-and-forth movement with a frequency of 0.4 Hz, which is equivalent to 12 bpm. The obtained results are depicted in Fig. 2.8, comparing the displacement measured by the laser sensor, and the one recovered by the radar using the AD. It can be seen that the radar was able to precisely recover the periodic movement, which contains approximately 4 full cycles in 20 seconds, corresponding to the programmed frequency of 12 bpm.

2.6.2 Live dummy tests

In order to emulate the more complex movement of a real target, the second set of tests was performed using a live dummy, developed for repetitive testing of breathing monitoring in a realistic scenario [152]. The size of the dummy is comparable to a newborn, and the torso tissue consists of a radar-reflective material with similar RCS. The dummy is integrated with a vacuum pump, which excites the torso to contract and

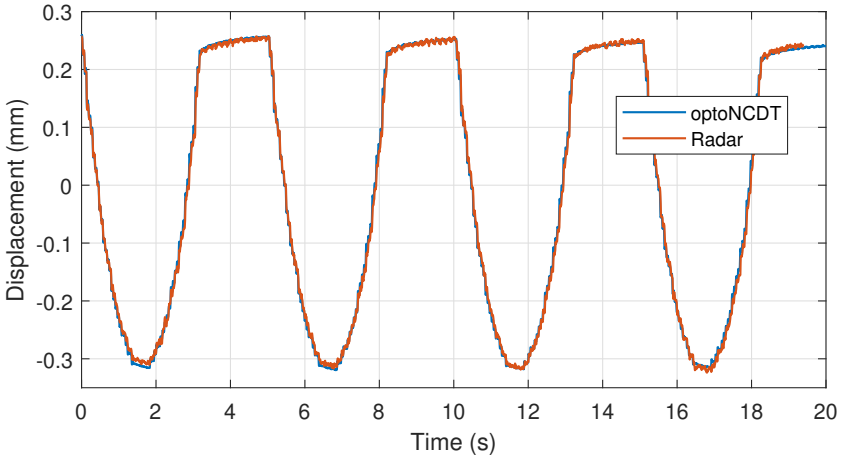

FIGURE 2.8: Recovered displacement signal from the speaker test.

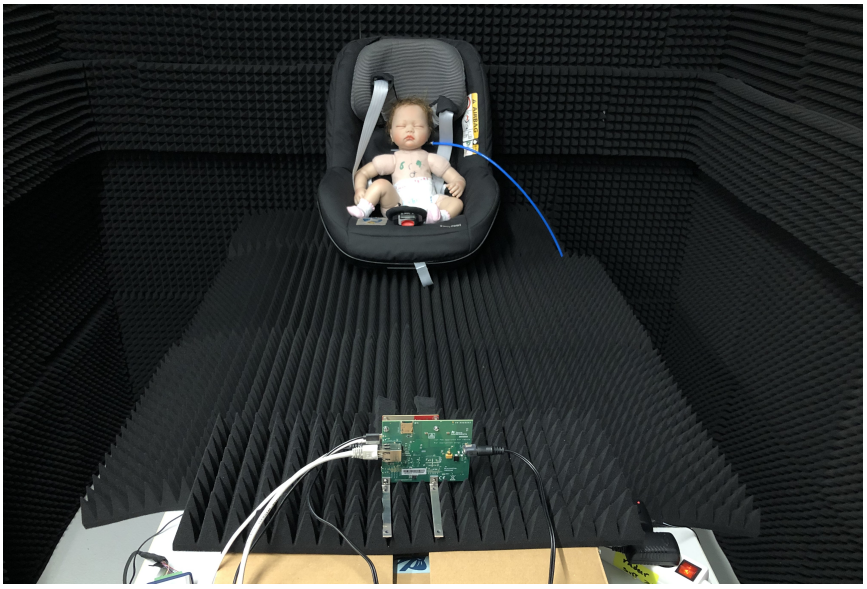

FIGURE 2.9: Setup for the tests with the live dummy. The pump is hidden on the right side of the seat.

expand cyclically. Fig. 2.9 shows the measurement setup, with the live dummy within a rear-facing child restraint system. The obtained results for a breathing rate of 25 bpm can be seen in Fig. 2.10, comparing the actual displacement measured by the laser sensor, and the one recovered by the radar. It can be seen how the radar was again able to precisely recover the movement. Small differences can still be perceived between the recovered signals and this is an expected effect. While the laser truly measures a single-scatter displacement, due to its limited resolution, the radar receives a superposition of signals reflected from many scatters located over the moving surfaces of the baby's chest and belly. Nevertheless, the periodic movement can still be clearly identified.

Additionally, Fig. 2.11 shows the spectrum of the recovered displacement signal using different phase demodulation techniques: the AD and the CSD. It can be seen how

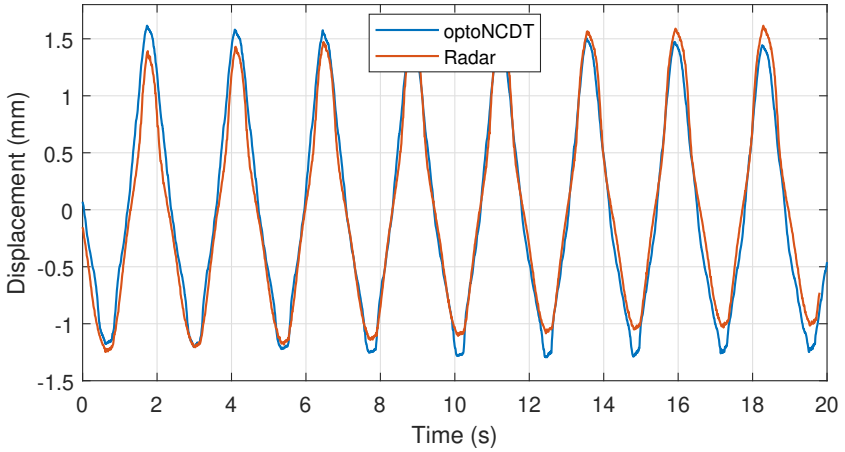

FIGURE 2.10: Recovered displacement signal from the live dummy test.

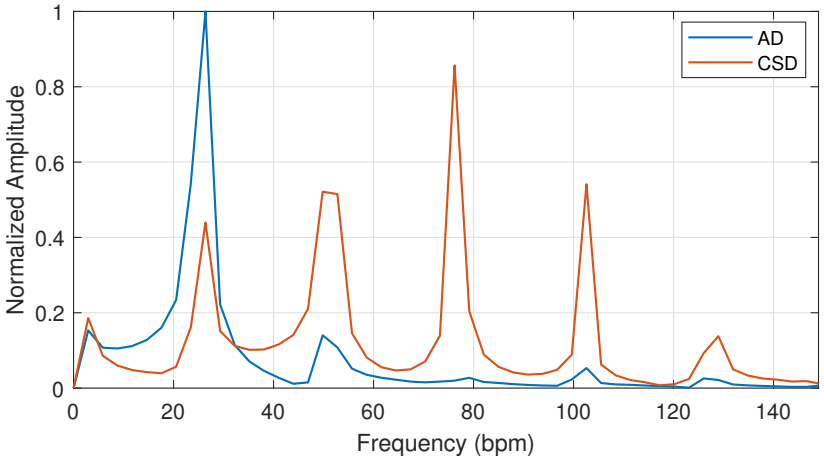

FIGURE 2.11: Live dummy normalized spectrum using AD and CSD.

the strong harmonics generated by the CSD may overshoot the main peak, making it difficult to identify the correct breathing frequency. This limitation of the CSD at higher operating frequencies will be further discussed in Chapter 3. On the other hand, the AD provides a clear spectrum where the dominant peak corresponds to the programmed breathing rate of 25 bpm. Nevertheless, a few harmonics can still be detected in the AD signal, and this spectral structure will be used for improving estimation in subsequent Chapters.

2.6.3 Human tests

For evaluating the final performance of the system, human experiments were also performed in a laboratory environment. Fig. 2.12 shows the measurement setup, where the subject was asked to stay seated in front of the radar, at a distance of 1.5 m. A wearable commercial device, named Hexoskin [153], was used as a reference for the chest

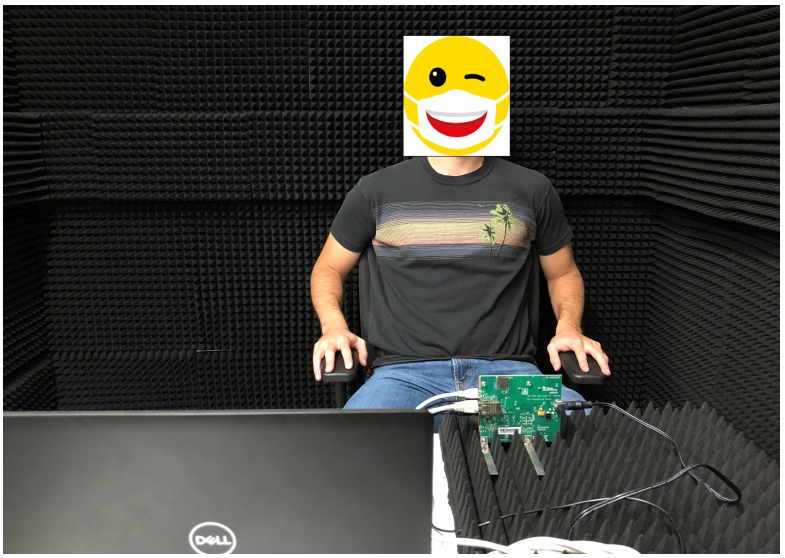

FIGURE 2.12: Setup for the tests with humans.

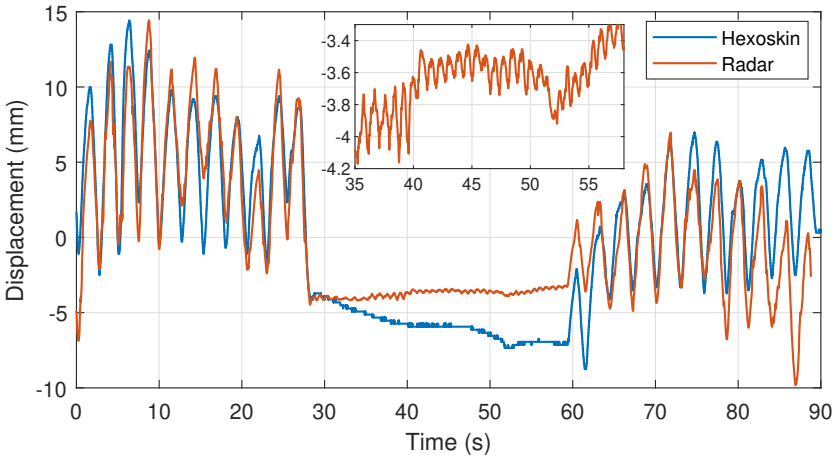

FIGURE 2.13: Chest wall displacement during the hold and release test.

wall movement and the actual breathing rate over time. This device has already been validated for breathing monitoring in different conditions [154].

The first test was a breath, hold, and release test, in which the subject was breathing for 30 seconds, held the breath for 30 seconds (inhaled), and finally breathed again in the last 30 seconds. Fig. 2.13 shows the obtained chest wall displacement, comparing radar data to the reference device. It can be seen the high correlation between both measurements, where breathe and hold moments can be easily identified. In addition, the inset figure shows that, when the subject is not breathing, the residual heartbeat movement becomes also clearly visible in the radar data.

In the last test, the subject was asked to stay seated in front of the radar, at the same distance, breathing normally for 10 minutes. Fig. 2.14 shows the final estimated values from radar and reference device. In this case, the estimation was performed using the

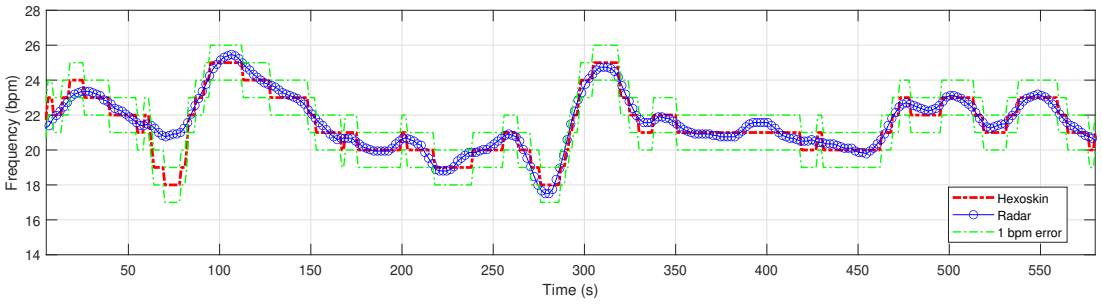

FIGURE 2.14: Estimated breathing frequency values for the 10-minute test. The red line is the reference sensor, with the ±1 bpm error interval in green.

simple nonlinear least squares (NLS) algorithm, which will be presented in Chapter 5. Most of the time (94.5%) the radar provided measurements within the ±1 bpm error interval, being capable of tracking the actual values even during fast variations of the breathing frequency. A complete description of these tests and results can be found in [155].

Chapter 3

Overview of recent techniques

3.1 Preamble

This chapter is the second part of our literature review. Here we present our first manuscript, which complements the previous chapter by delving deeper into a few topics and analyzing existing phase demodulation and estimation techniques. In this work, we describe a simulation framework and show selected results that allow easy performance comparison between recently proposed solutions for radar-based monitoring of vital signs. The idea was to go beyond an isolated theoretical analysis and understand the combined effects along the entire signal processing chain, for different combinations of scenarios, techniques, and parameters.

We conclude by investigating current limitations in the state of the art and introducing some of the challenges that will be addressed in the subsequent chapters.

3.2 Manuscript: Statistical Performance Analysis of Radar-Based Vital-Sign Processing Techniques

Gabriel Beltrão[1], Mohammad Alaee-Kerahroodi[1], Udo Schroeder[2], Dimitri Tatarinov[2], Bhavani Shankar M.R.[1]

[1] SnT - Interdisciplinary Centre for Security, Reliability and Trust, University of Luxembourg
[2] IEE S/A, Luxembourg

Published in: *Sensing Technology **886**. Lecture Notes in Electrical Engineering, pp. 101-112, Springer, Cham.*, 2022.
DOI: 10.1007/978-3-030-98886-9_8

This section is a copy of the paper referenced above.

Abstract

Radar-based vital-sign monitoring provides several advantages over standard methodologies. Despite the huge amount of recent work, the preference for particular technique(s) is in debt, due to lack of a formal comparison between them. In addition, collection of real data is a time-consuming process and therefore most of the proposed solutions are only evaluated under very limited scenarios. In this paper we present a simulation framework and a selection of results which allow easy performance comparison between radar-based vital-sign processing techniques. The proposed simulation tool scans over multiple breathing and heartbeat frequencies, and the combined effects along the entire signal processing chain can be analyzed, for different combinations of scenarios and techniques. The results have shown specific limitations for each method, thus indicating a need for proper selection based on operating conditions. In addition, while breathing estimation performance is only limited by noise, heartbeat estimation is limited by the presence of breathing harmonics and, despite promising results at specific breathing/heartbeat frequencies, the presented methods fail to fully mitigate this type of interference in all scenarios.

3.2.1 Introduction

Radar-based vital-sign monitoring provides several advantages over standard devices. Radar signals can penetrate through different materials and are not affected by the skin pigmentation or ambient light levels. In addition, radar devices are low-power, low-cost and privacy preserving [13]. These intrinsic characteristics have attracted the attention of the research community and, in line with recent technological advancements [112], a multitude of radar types are being used to address different applications such as sleep monitoring [89], rescue [90], in-car monitoring [156], and many others.

To comply with these different scenarios, a wide range of radar frequencies have already been used. While using a lower frequency improves electromagnetic penetration and allows easier extraction of the displacement signal, higher frequencies result in better phase sensitivity and increased target reflectivity [13]. However, the signal processing framework needs to be adjusted to each scenario, and setting up correct algorithms and parameters for each application therefore remains a complicated task. Despite the huge amount of recent work, there is still a lack of a formal and fair comparison between the basic vital-sign processing techniques. Particularly, given that each new proposal is evaluated in a very specific and limited scenario, it is difficult to compare their performance most of the time, and to address strengths and limitations of each technique. In addition, collection of real data is a time-consuming process and therefore most of the proposed solutions are only evaluated under very limited scenarios.

In this paper we aim to fill this gap by presenting a simulation framework and representative results which allow easy comparison between radar-based vital-sign processing techniques. The objective is to go beyond an isolated theoretical analysis, and understand the combined effects along the entire signal processing chain, for different combinations of scenarios, techniques and related parameters. The remainder of this paper is organized as follows. In section II, we introduce the signal modeling for vital-sign processing using radars. The simulation framework is presented in Section III, while Section IV presents our simulation results. Finally, in Section V, some conclusions are drawn.

3.2.2 Vital-Sign Models

The transmitted radar signal is modulated by the subtle chest-wall movements due to the breathing and heartbeat mechanisms, and is reflected with additional phase information related to this movement. Under ideal conditions, this time-varying phase can be written as

$$\Delta\theta(t) = \frac{4\pi d_b(t)}{\lambda} + \frac{4\pi d_h(t)}{\lambda}, \tag{3.1}$$

where λ is the operating wavelength, and $d_b(t)$ and $d_h(t)$ represent the displacement signal associated to the periodic chest-wall movement due to the breathing and heartbeat, respectively (different periods). While this signal is directly received from the radar's ADC in CW systems, in FMCW or PMCW systems it is the output of the range matched filter at the target range bin. In any case, the baseband I and Q signals from a target at nominal distance d_0 can be represented as

$$b_{\mathrm{I}}(t) = A_{\mathrm{I}} \cos\left(\theta_0 + \frac{4\pi d(t)}{\lambda}\right) + B_{\mathrm{I}} + n_{\mathrm{I}}(t), \tag{3.2}$$

$$b_{\mathrm{Q}}(t) = A_{\mathrm{Q}} \sin\left(\theta_0 + \frac{4\pi d(t)}{\lambda} + \varphi_{\mathrm{IQ}}\right) + B_{\mathrm{Q}} + n_{\mathrm{Q}}(t), \tag{3.3}$$

where A_{I} and A_{Q} represent the I/Q amplitude imbalance, φ_{IQ} is the I/Q phase imbalance, $\theta_0 = 4\pi d_0/\lambda$ is the constant phase shift, B_{I} and B_{Q} are DC offsets, and $d(t) = d_b(t) + d_h(t)$ represents the composite chest-wall movement. In addition, $n_{\mathrm{I}}(t)$ and $n_{\mathrm{Q}}(t)$ represent the noise component in each channel. Perfect recovery of the chest-wall motion $d(t)$ allows for a precise estimation of the breathing and heartbeat frequencies by simple analysis of the movement periodicity. However, in practice, the received radar signal is usually mixed with additional reflections from the external environment and noise. These interfering signals are usually much stronger than those induced by the chest-wall millimeter displacement, thus rendering the accurate recovery and subsequent vital-sign frequency estimation a challenging task.

Based on [28], the displacement due to breathing $d_b(t)$ can be modeled as a low-pass filtered periodic sequence of quadratic inspiration and exponential expiration, expressed as

$$d_b(t) = \begin{cases} \dfrac{-P_m}{T_i T_e} t^2 + \dfrac{P_m T}{T_i T_e} t, t \in [0, T_i] \\ \dfrac{P_m}{1 - e^{-\frac{T_e}{\tau}}} \left(e^{-\frac{(t-T_i)}{\tau}} - e^{-\frac{T_e}{\tau}} \right), t \in [T_i, T] \end{cases} \tag{3.4}$$

where P_m is a constant representing the pressure generated by the respiratory muscles, which controls the breathing displacement amplitude, T_i is the inspiration time, T_e is the expiration time, T is the breathing period, and τ is a time constant. The inspiratory and expiratory times are considered fixed fractions of T. Hence, the profile is fully parameterized by P_m and the actual breathing period T. The value of τ was assumed to be equal to 1/5 of the expiratory time and a value of 0.6 was used for the inspiratory-expiratory time ratio [28]. The standard physiological range of the breathing frequency is 10 to 25 bpm, while the amplitudes of the chest-wall motion can vary from 4 to 12 mm [15].

For modeling the heartbeat, a Gaussian pulse train can be used, based on the idea that the heartbeat is a short explosive motion, with pulsatile nature. The heartbeat displacement signal can thus be represented as [104]

$$d_h(t) = \sum_n a e^{-\frac{(t-T_n)^2}{2c^2}}, \tag{3.5}$$

where a is a normalization coefficient, c controls the pulse width, and T_n is the time interval between consecutive pulses. The standard physiological range of the heartbeat frequency goes from 60 to 100 bpm, while the amplitudes of the chest-wall motion can vary from 0.2 mm to 0.5 mm [15].

It is important to mention that the true chest-wall motion is a complex physiological phenomenon and it is unlikely that any model can fully characterize it in every situation. However, regardless of the displacement signal shape, its frequency content (spectral structure) is mainly determined by its inherent periodicity. The models used here are well-known and selected for illustrative purposes. In addition, the processing techniques described next are model agnostic and hence the chosen model does not disadvantage any one of them.

3.2.3 Simulation Framework

The composite displacement signal is used to generate the I and Q samples according to (3.2) and (3.3), and additive white Gaussian noise (AWGN) is added to the complex samples according to a predefined SNR value. In addition, the parameters A_{I}, A_{Q} and φ_{IQ} can be used for modelling I/Q imbalance scenarios.

Fig. 3.1a shows 20 seconds of the generated displacements for both breathing and heartbeat motion, and the composite movement according to the described models. The amplitude and frequency were selected to be 10 mm and 12 bpm for breathing, and 0.5 mm and 60 bpm for the heartbeat.

Given that standard amplitudes for the heartbeat displacement are usually 10 to 20 times smaller than the breathing displacement [50], the heartbeat main frequency component may eventually be masked by interfering harmonics from the breathing movement. Within the simulation framework, the amplitude relation between then can be independently controlled by the parameters P_m and a in (3.4) and (3.5) respectively, which will determine the signal-to-interference ratio (SIR) for heartbeat detection, where $SIR = a/P_m$.

The simulator allows for scanning over multiple breathing and heartbeat frequencies, as well as SIR and SNR values, in a Monte Carlo approach. For all iterations of signal generation and processing, the final estimation root-mean-square error (RMSE) is calculated, taking into consideration the entire signal processing chain. In this way, the techniques can be evaluated not only with respect to the noise, but also in relation to the combined effects of different methods and parameters. Finally, the performance can also be analyzed considering the influence of breathing over the heartbeat signal and vice-versa.

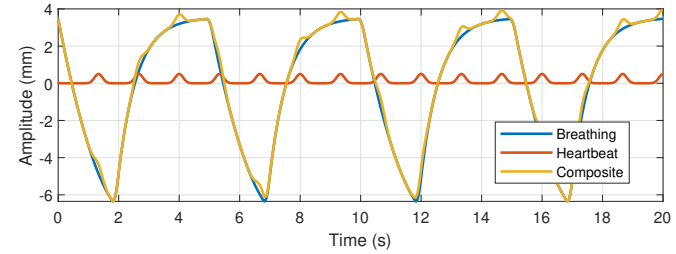

(a)

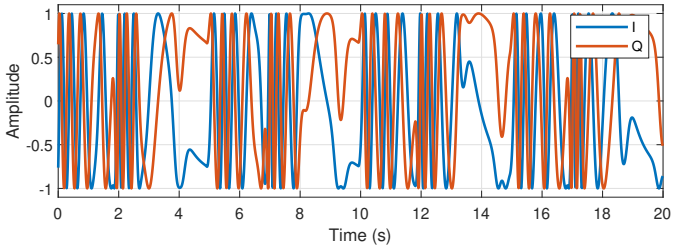

(b)

FIGURE 3.1: Simulated displacement (a) and I/Q (b) signals.

3.2.4 Simulation Results

3.2.4.1 Phase Demodulation

The initial signal processing step is commonly known as phase demodulation. It is essentially the process where the received I and Q signals are combined with the aim to recover the displacement signal $d(t)$. Among several methods, the two widely used are the AD [117] and the CSD [116].

Complex-Signal Demodulation The CSD relies on small displacements (in relation to the operating wavelength) for recovering an approximation of the chest-wall motion. In this case, the displacement signal can be reconstructed as

$$x(t) = b_{\mathrm{I}}(t) + \mathrm{j} \cdot b_{\mathrm{Q}}(t) = \overline{x} + \exp\left\{\mathrm{j}\left[\theta_0 + \Delta\theta(t)\right]\right\}, \tag{3.6}$$

where $\overline{x} = B_{\mathrm{I}} + \mathrm{j}B_{\mathrm{Q}}$ represents a combined DC offset. Despite additional higher order harmonics, for small displacements (in relation to the operating wavelength), the recovered signal $x(t)$ approximates the true chest-wall movement $d(t)$, and the relevant frequency content is preserved.

Arctangent Demodulation On the other hand, the AD can be used for precise phase recovery. The AD directly extracts the phase of the received signal and, under ideal

conditions, it recovers the displacement signal as

$$x(t) = \frac{\lambda}{4\pi} \cdot \text{unwrap}\left(\arctan \left[\frac{b_{\text{Q}}(t)}{b_{\text{I}}(t)} \right] \right), \tag{3.7}$$

where the unwrap is necessary for removing possible phase discontinuities caused by the restricted codomain of the arctangent function. This operation is very sensitive to noise and interference, and may eventually accumulate errors, resulting in large distortions on the recovered displacement signal.

DACM To avoid the aforementioned limitations, the so called DACM demodulation has also been proposed [120]. The DACM calculates the derivative of the arctangent function, followed by an integration step for recovering the phase. Its extended version can be efficiently implemented in the discrete form

$$x[n] = \sum_{k=2}^{n} \frac{b_{\text{I}}[k](b_{\text{Q}}[k] - b_{\text{Q}}[k-1]) - b_{\text{Q}}[k](b_{\text{I}}[k] - b_{\text{I}}[k-1])}{b_{\text{I}}[k]^2 + b_{\text{Q}}[k]^2}, \tag{3.8}$$

where the differentiation is approximated by a forward difference, and the integration is replaced by an accumulation.

Linear Demodulation Finally, the LD tries to suppress redundant information, and maximize the variance in the input signal [4]. It is based on the PCA of the input matrix

$$M_{IQ} = \begin{bmatrix} b_{\text{I}}(t) \\ b_{\text{Q}}(t) \end{bmatrix}, \tag{3.9}$$

where its first principal component is used as demodulated signal.

Fig.3.2 shows the final RMSE for each of these demodulation techniques, considering breathing estimation at 24 GHz and 60 GHz. In all cases, simple DFT-based estimation was used, where the estimated frequency is selected as the one yielding the maximum value of the DFT spectrum. The breathing frequencies are being scanned from 10 bpm to 25 bpm with intervals of 1 bpm. The relevant simulation parameters are summarized in Table 3.1[1], and will be used in the following simulations, unless explicitly stated otherwise.

At 24 GHz, both the CSD and LD are robust to the noise, with small errors even for negative values of the SNR. The SNR threshold for correct operation is much higher for the AD, as well as for the DACM. At higher frequencies, when the displacement

[1] In this paper, we decided to use "wide" filters intentionally, in order to not interfere with the desired analysis.

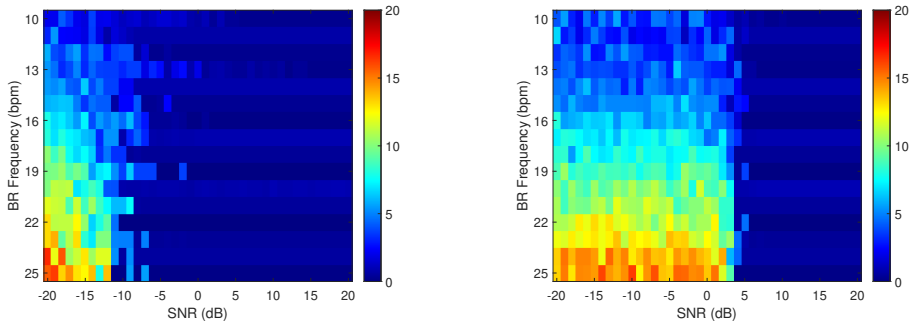

(a) CSD

(b) AD

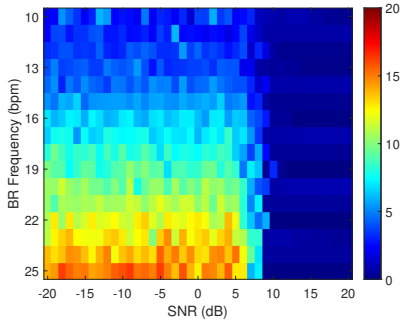

(c) DACM

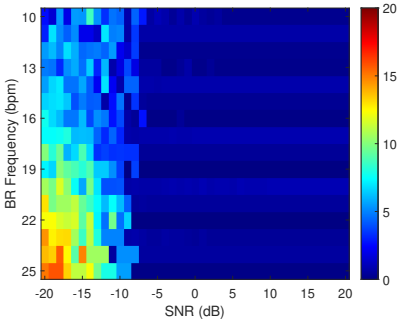

(d) LD

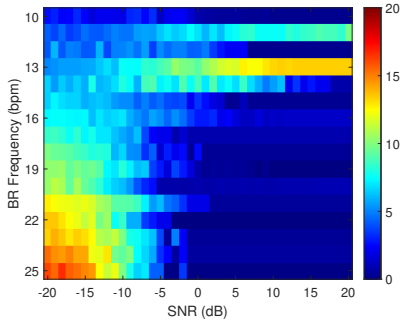

(e) CSD

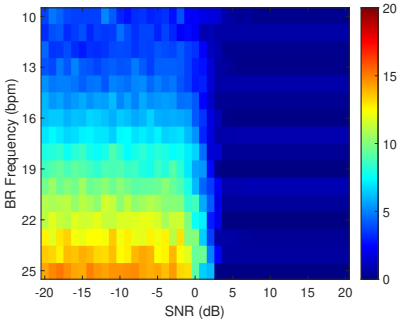

(f) AD

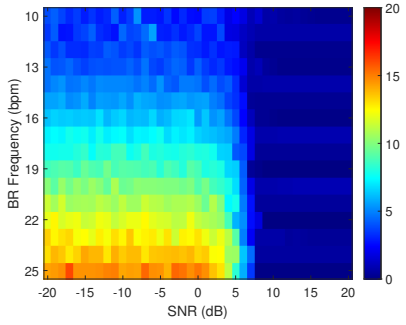

(g) DACM

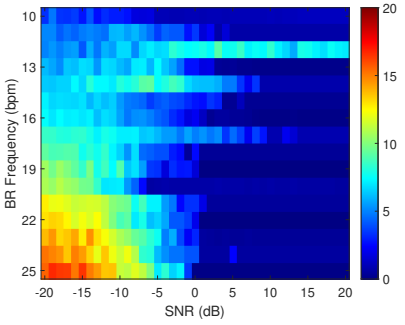

(h) LD

FIGURE 3.2: RMSE (bpm) for breathing estimation considering different demodulation techniques at 24 GHz (a-d) and 60 GHz (e-h).

amplitude is comparable to the operating wavelength, the CSD approximation does not hold anymore. At this point, intermodulation products and higher order harmonics

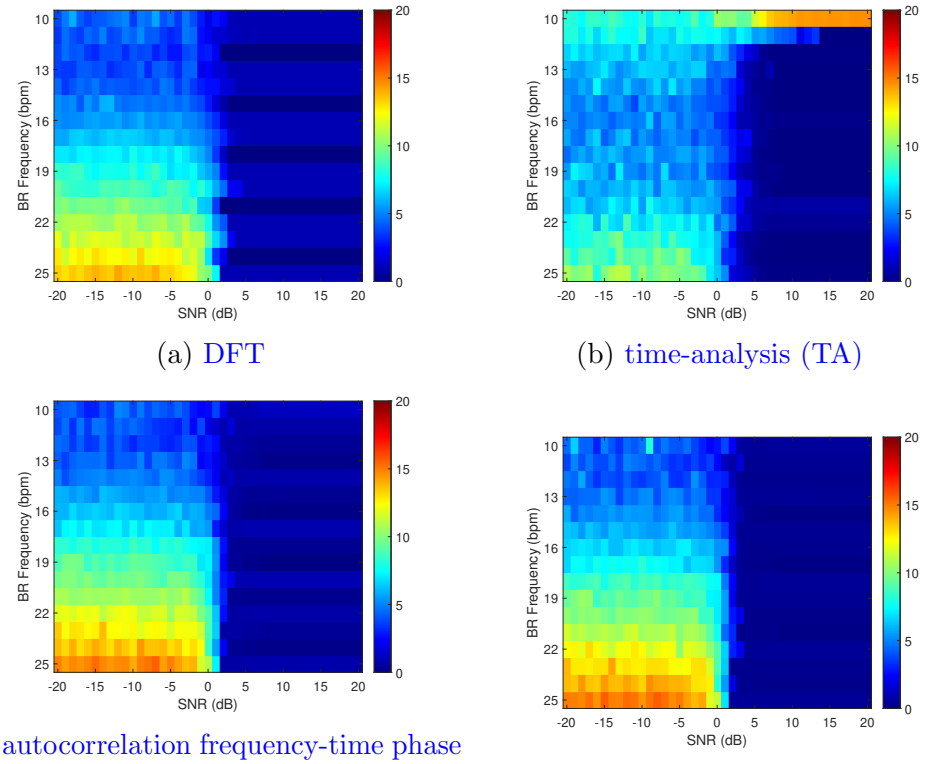

(a) DFT

(b) time-analysis (TA)

(c) autocorrelation frequency-time phase regression (ACC-FTPR)

(d) NLS

FIGURE 3.3: RMSE (bpm) for breathing estimation considering the AD and different estimation techniques at 60 GHz.

start to dominate the spectrum, eventually being higher than the fundamental frequency component, which leads to estimation errors. The same effect seems to affect the LD. On the other hand, both AD and DACM presented better performance at 60 GHz.

3.2.4.2 Breathing Estimation

Fig.3.3 shows the final RMSE considering the AD and different estimation techniques at 60 GHz (from now on, all the presented results will be related to this setup). In Fig. 3.3b the estimation was performed by TA of the displacement signal, where the average distance between peaks provides an estimate of the signal periodicity [157]. In Fig. 3.3c the ACC-FTPR technique from [104] was used. It is based on spectral estimation over the displacement signal autocorrelation, with the resolution being further improved by phase-regression using the complex sample of the dominant peak. Lastly, the NLS approach recently proposed in [155] was used in Fig. 3.3d. In this case, not only the dominant peak in the spectrum is used for estimation, but also its inherent harmonics which could eventually be detected.

In this idealized case of breathing estimation without any external interference, the performance is limited only by noise and, after the SNR threshold, all techniques reach

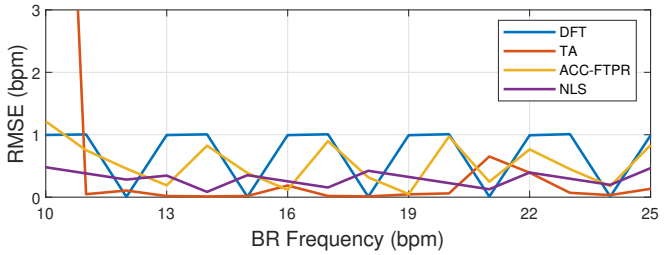

(a)

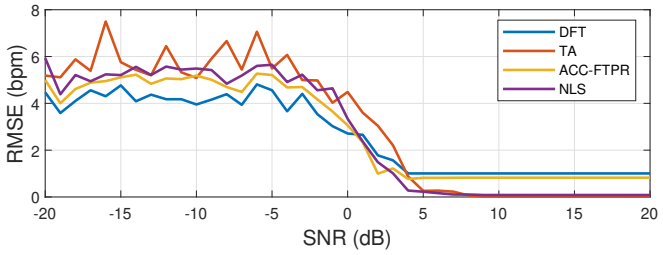

(b)

FIGURE 3.4: (a) RMSE as a function of the reference breathing frequency. (b) RMSE as function of the SNR.

TABLE 3.1: Standard simulation parameters.

Parameter	**Value**
Sampling frequency (Hz)	100
Processing window (s)	20
Breathing bandpass filter (Hz)	0.1-0.7
Heartbeat bandpass filter (Hz)	0.75-3
Zero-padding (samples)	2048
Breathing range (bpm)	10-25
Heartbeat range (bpm)	50-110
SNR range (dB)	-20 to +20
Number of trials	100

very low error values (always better than 1 bpm). However, by looking closer to the results in Fig. 3.4, it can be seen that the techniques have improved the frequency resolution and reduced the final error in relation to the standard DFT estimation. While Fig. 3.4a shows the error as a function of the reference breathing frequency, for the best SNR (20 dB), Fig. 3.4b shows the error as a function of the SNR, for a reference breathing frequency of 18 bpm. In addition, despite better results at higher SNR values, the TA-based estimation has poorer performance in the presence of noise and thus needs a higher SNR for correct estimation.

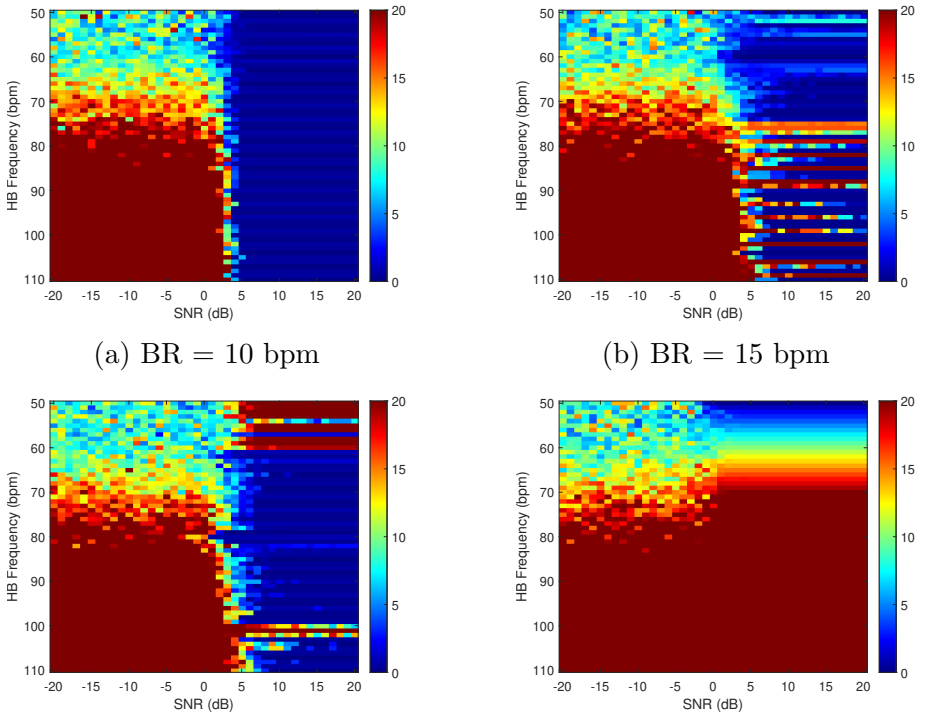

(a) BR = 10 bpm (b) BR = 15 bpm

(c) BR = 20 bpm (d) BR = 25 bpm

FIGURE 3.5: RMSE (bpm) for heartbeat estimation considering different breathing frequencies, with a SIR of 1/12.

3.2.4.3 Heartbeat Estimation

On the other hand, heartbeat estimation performance is influenced not only by the SNR, but mainly by the presence of high-order breathing harmonics. Fig. 3.5 shows the heartbeat estimation performance at 60 GHz, using the AD and standard DFT estimation, and considering different breathing frequencies for a SIR of 1/12. It can be seen that for smaller values of breathing frequency the amount of harmonic interference is low and the heartbeat frequency can be precisely estimated given the minimum required SNR. However, for higher breathing frequencies, the interfering harmonics become dominant until a point where the heartbeat component is completely masked. At this point, the DFT estimation is in fact measuring breathing harmonics rather than the heartbeat frequency. This dynamic can be explained as follows: for lower breathing frequencies, the heartbeat estimation is competing with higher orders (5th, 6th and so on) of breathing harmonics which are already strongly attenuated. On the other hand, for higher breathing frequencies, the second and third harmonics are already over the heartbeat frequency range. These harmonics can be much stronger than the main heartbeat frequency component and thus prevent accurate estimation. In addition, Fig. 3.6 shows the results now considering a single breathing frequency of 12 bpm, but varying the SIR from 1/5 (Fig. 3.6a) to 1/20 (Fig. 3.6d). It can be seen in this case that, depending on the

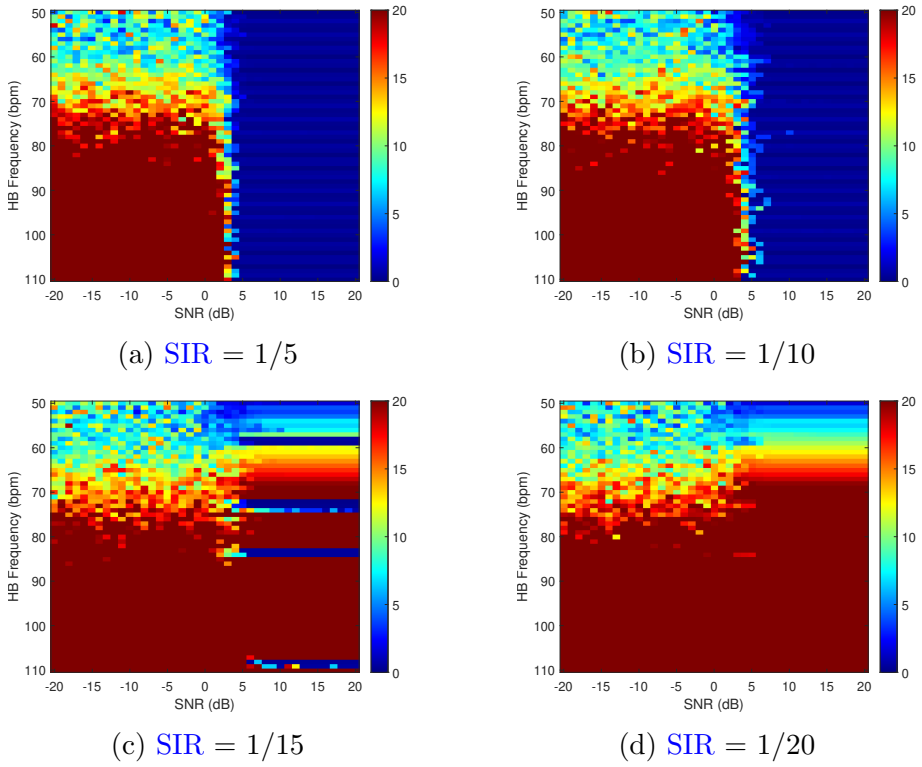

(a) SIR = 1/5 (b) SIR = 1/10

(c) SIR = 1/15 (d) SIR = 1/20

FIGURE 3.6: RMSE (bpm) for heartbeat estimation considering different SIR, with a breathing frequency of 12 bpm.

SIR, even a smaller breathing frequency can generate harmonics capable of masking the heartbeat component and prevent correct estimation.

Fig. 3.7 shows the heartbeat estimation performance considering different estimation methods, when the breathing frequency is 12 bpm and the SIR is 1/15. In Fig. 3.7a, standard DFT estimation was used with no additional harmonic processing. In Fig. 3.7b, an algorithm for selecting spectrum peaks was used (DFT_PS), exploiting the knowledge of the already estimated breathing frequency and its harmonic-related positions. Instead of just selecting the maximum spectral peak in the heartbeat region, the algorithm looks for the higher peak which is not in a possible harmonic position. In Fig. 3.7c a simpler implementation of the RELAX algorithm [158] was used. In this case, the breathing harmonic components are iteratively estimated and removed from the displacement signal, until heartbeat peaks can be found. Lastly, Fig. 3.7d shows the results when spectral estimation is performed in the region of the second heartbeat harmonic (DFT_2nd). This algorithm was originally proposed in [99], and is based on the fact that the second heartbeat harmonic will probably be limited only by noise while the main heartbeat frequency component can be masked by low-order harmonics of breathing. Both DFT_PS and RELAX presented good performance with accurate estimation, except when the heartbeat frequency overlaps with the breathing harmonics positions. The DFT_2nd solves the overlap problem, however it has a higher SNR threshold and fails for higher

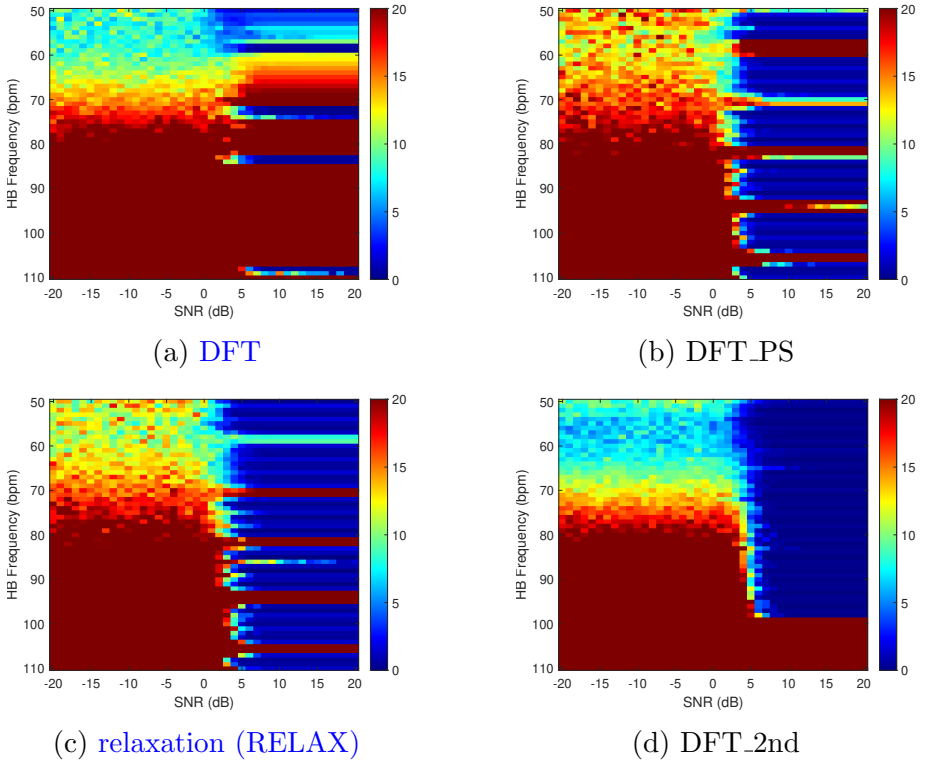

(a) DFT (b) DFT_PS

(c) relaxation (RELAX) (d) DFT_2nd

FIGURE 3.7: RMSE (bpm) for heartbeat estimation considering different estimation methods, with a breathing frequency of 12 bpm, and a SIR of 1/15.

heartbeat frequencies, when the main heartbeat frequency component is within the second harmonic region (ambiguity).

In order to provide a complete picture of the harmonic relations, Fig. 3.8 finally shows the RMSE for heartbeat estimation for all combinations between breathing and heartbeat frequencies, when the SNR and SIR are respectively 20 dB and 1/15. Despite relatively good performance for specific frequency combinations, most of the time all techniques fail to provide accurate estimation, specially for higher frequency values. This indicates that robust solutions would need more powerful methods to deal with the harmonics problem.

3.2.5 Conclusions

In this paper we presented a simulation framework and representative results to ease the comparison between radar-based vital-sign processing techniques. The proposed simulation tool allows for scanning over multiple breathing and heartbeat frequencies, and the resulting RMSE is calculated using a Monte Carlo approach. In this way, the combined effects along the entire signal processing chain could be analyzed, for different combinations of scenarios, techniques and parameters.

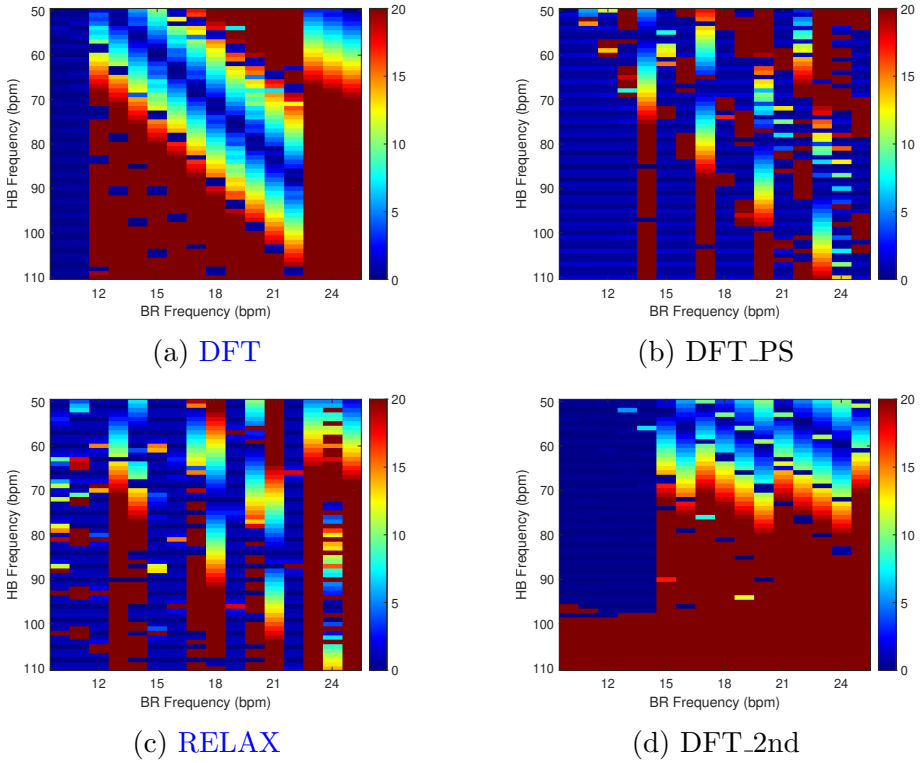

(a) DFT (b) DFT_PS

(c) RELAX (d) DFT_2nd

FIGURE 3.8: RMSE (bpm) for heartbeat estimation considering different estimation methods, and all combinations of breathing and heartbeat frequency. The SNR and SIR were 20 dB and 1/15, respectively.

We compared different demodulation techniques and the results have shown specific limitations for each method, thus indicating the need for a proper selection considering the operating frequency and expected SNR. In addition, in ideal conditions (no external interference), breathing estimation performance is only limited by noise and standard techniques may provide accurate results, with minor performance difference between them. On the other hand, the performance of heartbeat estimation is limited by the presence of breathing harmonics and, despite promising results at specific frequencies, the presented methods fail to fully mitigate this interference, specially at higher breathing/heartbeat frequencies. This indicates that specific harmonic mitigation techniques are thus needed in order to provide robust heartbeat estimation over all conditions.

Chapter 4

Phase Demodulation

4.1 Preamble

The desired vital sign information is embedded in the phase of the received radar signal. After detecting the monitored subject, the preprocessing block extracts the corresponding signal which was modulated by the chest movements. The phase demodulation block then aims to recover these movements from the selected signal.

As we will show soon, conventional phase demodulation methods have limitations in practical situations, especially when dealing with interfering RBMs. It is important to mention that if the interfering signal is not spectrally overlapped with the vital sign information, it can be easily filtered by conventional spectral analysis. However, inaccurate phase demodulation may introduce nonlinear errors that can hinder filtering and prevent subsequent frequency estimation even under the simplest interference.

To enable robust phase demodulation in practical scenarios, in this chapter we present our second manuscript, with a new algorithm for recovering the chest wall motion from radar data. It exploits the novel framework of Unlimited Sampling (US) to greatly extend the resilience of the recovery process. In this way, accurate demodulation can be achieved, even under strong RBM interference.

4.2 Manuscript: Unlimited Sampling for Radar-based Vital Sign Monitoring

Gabriel Beltrão[1], Thomas Feuillen[1], Bhavani Shankar M.R.[1],
Mohammad Alaee-Kerahroodi[1], Udo Schroeder[2]

[1] SnT - Interdisciplinary Centre for Security, Reliability and Trust, University of Luxembourg
[2] IEE S/A, Luxembourg

Invited paper in: *Asilomar Conference on Signals, Systems, and Computers*, 2022.
DOI: (to be published)

This section is a copy of the paper referenced above.

Abstract

This paper tackles the contactless recovery of vital sign information from backscattered signals using a radar device. These sensors do not require any physical contact with the patient, which makes them extremely suitable for healthcare applications such as the long-term monitoring of patients or elderly care. In this context, the information regarding the breathing and heart rate is embedded within the phase of the received radar signal and inherently suffers from a 2π ambiguity. For sensors operating at millimeter-wave, common recovery methods rely on algorithms that unwrap the phase. These methods, however, do not possess strong recovery guarantees and often fail when encountering quick phase variations (e.g., random body movements and larger chest displacements). This can hinder accurate estimation and possibly prevent the proper medical diagnosis. This paper proposes to do away with these limitations by using the framework of Unlimited Sampling (US) to address the recovery of the signal embedded in the phase. Compared to other unwrapping algorithms, the US framework provides perfect recovery guarantees in practical settings. Furthermore, we show through simulations that the US-based recovery algorithm greatly extends the resilience of the recovering process when encountering random body movements at comparable sampling rates.

4.2.1 Introduction

Due to the rapid aging of the population worldwide, a lot of effort is being dedicated to providing more efficient healthcare solutions. Recently, there has been renewed interest in the contactless monitoring of vital signs such as breathing and heart rate. Continuously monitoring this information is crucial for long-term patient care, especially when conventional cabled or wearable devices cannot be used.

In this context, radar devices are emerging as a promising technology. Radar signals can penetrate through different materials and are not affected by skin pigmentation

or ambient light levels. In addition, radar devices preserve privacy [13], and can be low-power and low-cost. These characteristics make radar sensors very suitable for several healthcare applications, including sleep monitoring [89], assisted living [91], diagnosis [92], newborn monitoring [159], and many others.

The information regarding the vital signs is embedded within the phase of the received radar signal and inherently suffers from a 2π ambiguity. For sensors operating at millimeter-wave, recovery methods rely on the AD [92, 117, 160], which requires an additional unwrap operation to unfold the phase. The conventional unwrap algorithm, however, does not possess recovery guarantees and often fails when encountering quick phase variations, usually caused by interfering RBMs or even larger chest displacements. These recovery errors can hinder accurate estimation and possibly prevent the proper medical diagnosis.

To overcome these limitations, in this paper we propose a new algorithm that uses the framework of US [161, 162] to address the recovery of the signal embedded in the phase. Compared to the conventional unwrap algorithm, the US provides perfect recovery guarantees in practical settings [161–163]. Furthermore, we show through simulations that the US-based recovery algorithm greatly extends the resilience of the recovering process when encountering random body movements at comparable sampling rates.

The remainder of this paper is organized as follows. In section 4.2.2, we introduce the signal modeling for vital sign processing using radars. In Section 4.2.3 we describe a widely used unwrap-based phase demodulation method and highlight its limitations. In Section 4.2.4 we present the US framework and how it can be used to overcome these issues. Finally, in Section 4.2.5, we show in a simulation setting the gain provided by the US-based recovery algorithm, whereas, in Section 4.2.6, a few conclusions are drawn.

4.2.1.1 Notation

Throughout this paper, we are adopting the following notation: lower case boldface for vectors $\boldsymbol{x}$ and upper case boldface for matrices $\boldsymbol{X}$. The letter j represents the imaginary unit (i.e., $\mathrm{j} = \sqrt{-1}$), with the absolute value given by $|(\cdot)|$. The Euclidean norm of the vector $\boldsymbol{x}$ is denoted by $\|\boldsymbol{x}\|$. For any complex number x we use $\Re$ and $\Im$ to denote, respectively, the real and the imaginary parts of x. The first order difference of a signal $\boldsymbol{s}$ is denoted by $(\Delta \boldsymbol{s})[k] \stackrel{\text{def}}{=} s[k+1] - s[k]$, whereas the N-th order difference $\Delta^N \boldsymbol{s}$ is obtained by the recursive application of the finite-difference operator. Finally, S is the anti-difference operator.

4.2.2 Vital Sign Models

The transmitted radar signal is modulated by the subtle chest wall motion due to the breathing and heartbeat mechanisms. The vital sign information is then embedded in the received radar signal as an additional phase modulation related to the chest wall movement. The complex slow-time signal received from the monitored subject at nominal distance d_0 can be represented as

$$s(t) = \exp\left\{\mathrm{j}\left(\theta_0 + \frac{4\pi d(t)}{\lambda}\right)\right\}, \tag{4.1}$$

where $\theta_0 = 4\pi d_0/\lambda$ is a constant phase shift. The time-varying phase component of the received signal can be written as

$$\frac{4\pi d(t)}{\lambda} = \frac{4\pi}{\lambda}\big(d_{\mathrm{b}}(t) + d_{\mathrm{h}}(t) + d_{\mathrm{rbm}}(t)\big), \tag{4.2}$$

where λ is the operating wavelength, and $d_{\mathrm{b}}(t)$ and $d_{\mathrm{h}}(t)$ represent the chest wall motion due to the breathing and heartbeat, respectively. The additional body movement is represented by d_{rbm}, with the subscript RBM here to highlight its random and unknown pattern in practical settings. The amplitudes of the chest wall motion vary from 4 to 12 mm when breathing, and 0.2 mm to 0.5 mm when the heart beats [15]. At rest, the standard physiological range of the breathing rate goes from 10 to 25 breaths per minute, whereas, for the heart rate, it goes from 60 to 100 beats per minute.

In ideal conditions, perfect recovery of the chest wall motion $d(t)$ would allow for precise estimation of the breathing and heart rates by simple analysis of the movement periodicity. However, in practice, the received radar signal is usually tainted by reflections from the external environment and additional RBMs from the monitored subject. These interfering signals are usually much stronger than those induced by the chest wall millimeter displacement, thus rendering the accurate recovery of vital signs challenging. It is important to note these RBMs cannot be avoided in practical situations. Therefore, contactless monitoring can only reach its full potential if it can be seamlessly integrated without added restrictions on the patients. This is why developing methods that are robust to large RBMs is of paramount importance for radar-based monitoring of vital signs [76, 112, 124].

4.2.3 Phase Demodulation

Phase demodulation is essentially the process where the complex samples of the slow-time signal are combined, in order to recover the displacement signal from the phase variation

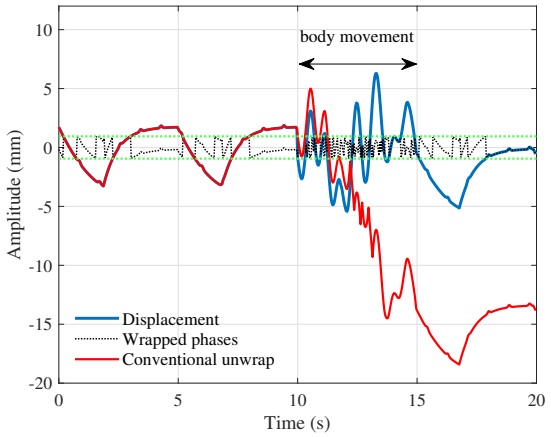

FIGURE 4.1: Chest wall displacement contaminated with additional body movement: true displacement, wrapped phases around $\pm\lambda/2$, and recovered signal using the conventional unwrap algorithm.

over time. Several techniques have already been proposed for that, including the complex-signal demodulation (CSD) [116, 144, 164] and the linear demodulation [4, 93, 165]. As discussed in [122], these methods suffer from intermodulation products and harmonic interference when working at higher operating frequencies. To avoid these issues and enable precise phase recovery, the AD is commonly used. In this case, the recovered displacement signal can be obtained using

$$\widehat{d}(t) = \frac{\lambda}{4\pi} \cdot \text{unwrap}\left(\arctan \left[\frac{\Im(s(t))}{\Re(s(t))} \right] \right). \tag{4.3}$$

As the phase is bounded by $[-\pi, \pi]$, displacements larger than $\lambda/4$ will result in discontinuities. To reconstruct the phase and estimate the signal of interest, the AD requires an additional unwrap operation.

The conventional unwrap algorithm is commonly used, and it has a very straightforward implementation. Whenever the phase jump between two consecutive samples is greater than or equal to π radians, it corrects the new sample by adding $\pm 2\pi$, so that the difference becomes less than π. However, this algorithm is very sensitive to interference. It often fails when dealing with signals that exhibit quick phase variations, which can be due to RBMs or even faster chest displacements. In these cases, unwrap errors can be accumulated and result in large distortions in the recovered displacement signal. Figure 4.1 shows a 20-second segment of a simulated chest wall displacement signal, contaminated with a short segment of RBM interference. Initially, when only the breathing and heartbeat signals are present, the wrapped phases can be accurately recovered. However, in the presence of additional RBMs, the conventional unwrap fails and large distortions are then introduced in the recovered signal.

The well-known Itoh's condition [166] defines theoretical bounds for the performance of the conventional unwrap algorithm. It states that a necessary condition for successfully recovery is that the maximum amplitude of the first-order difference of input samples should be limited by λ. In other words, the maximum phase (displacement) variation between adjacent time samples should be smaller than the operating wavelength, *i.e.*

$$\forall k \in [K], \left|d[k+1] - d[k]\right| \leqslant \lambda, \tag{4.4}$$

where k is the sample index for a signal with K samples. If this is satisfied, phase changes greater than π indicate that the phase should be corrected simply by adding or subtracting 2π. Increasing the sampling frequency will generate highly correlated samples with a lower first-order difference. So the performance of conventional unwrap is dependent on the slow-time sampling frequency. This can usually lead to substantial oversampling. However, Itoh's condition is a necessary but not sufficient condition for successful reconstruction. Under practical settings and reasonable amplitude of random body movements, the conventional unwrap operation used in the AD completely fails to recover the chest wall displacement signal.

4.2.4 Unlimited Sampling

The previous section introduced the inherent challenge that arises when estimating vital signs from radar measurements, *i.e.*, the information of interest is embedded in the phase of the received signal. Considering the limitations of the classic unwrap method, we introduce here the use of the US framework for recovering the vital sign information.

The US is a novel framework that breaks away from the limitations of the classic unwrapping method, that is Itoh's condition, by leveraging the fact that the signals of interest are bandlimited. It was originally proposed for tackling ADC saturation by co-designing the sensing architecture and the algorithms that fold the signal; thus giving an *unlimited* dynamic range. Earlier publications [161–163] first demonstrated theoretical recovery capabilities using US-enabled devices, whereas recent publications are demonstrating its potential in real settings [167–169]. In this work, we leverage this new framework in the context of recovering the phase for radar-based monitoring of vital signs.

Let us consider the following acquisition model. Let $g(t) := 2d(t)$ be the signal of interest, sampled at a rate $\frac{1}{T}$, using a modulo-based acquisition system $\mathscr{M}_\lambda(\cdot)$ with a dynamic range of λ ($\pm\lambda/2$). The acquired folded signal is thus

$$y[k] = \mathscr{M}_\lambda(g(kT)), \tag{4.5}$$

where the link between (4.5) and (4.1) is given by

$$\mathscr{M}_\lambda(g(kT)) = \frac{\lambda}{2\pi}\angle s(kT), \tag{4.6}$$

with $\frac{1}{T}$ being the slow-time sampling rate. While the conventional unwrap only has a necessary condition for reconstruction, the US provides the following result:

Theorem 4.1 (Unlimited Sampling Theorem, [162])**.** *Let $g(t)$ be a finite energy, bandlimited signal with maximum frequency Ω and let $y[n]$, $n \in \mathbb{Z}$ in (4.5) be the modulo samples of $g(t)$ with sampling rate $\frac{1}{T}$. Then a sufficient condition for the recovery of $g(t)$ from $y[n]$ is that $T \leqslant \frac{1}{2\Omega e}$ (up to additive multiples of 2λ) where e denotes Euler's constant.*

It is interesting to see that the sampling rate $\frac{1}{T}$ required for perfect reconstruction neither depends on the amplitude of the signal nor, and more strikingly, on the dynamic range λ used for the folded acquisition (*e.g.* the radar's wavelength). Herein lies the main advantage of using the US framework; only the knowledge that the signal is bandlimited is sufficient to guarantee its perfect reconstruction. One can also see the result in Theorem 4.1 as an extension of the Nyquist sampling theorem to folded signals. Along with this result, the authors in [162] also developed an iterative reconstruction algorithm that provides perfect estimates $\widetilde{d}[k]$ from the folded measurements $y[k]$.

Algorithm 1 Unlimited Sampling Algorithm

Data: $y[k]$ and $\lambda\mathbb{Z} \ni \beta_r \geqslant 2\|d\|_\infty$.
Result: $\widetilde{d}[k] \approx d[k]$.

1) Compute $N = \left\lceil \frac{\log \lambda/2 - \log \beta_r}{\log(T\Omega e)} \right\rceil$.
2) Set $z_{(0)}[k] = \left(\mathscr{M}_\lambda(\Delta^N y) - \Delta^N y\right)[k]$.
3) for $n = 0 : N-2$
   - (i) $z_{(n+1)}[k] = \left(\mathsf{S} z_{(n)}\right)[k]$.
   - (ii) $z_{(n+1)} = \lambda \left\lceil \frac{\lfloor 2z_{(n+1)}/\lambda \rfloor}{2} \right\rceil$ (rounding to $\lambda\mathbb{Z}$).
   - (iii) With $J = 12\beta_r/\lambda$, compute κ_n. $\kappa_n = \left\lfloor \frac{\mathsf{S} z_{(n+1)}[1] - \mathsf{S} z_{(n+1)}[J+1]}{24\beta_r} + \frac{1}{2} \right\rfloor$
   - (iv) $z_{(n+1)}[k] = z_{(n+1)}[k] + \lambda\kappa_{(n)}$.

   end
4) $\widetilde{d}[k] = \frac{1}{2}\left[\left(\mathsf{S} z_{(N-1)}\right)[k] + y[k] + m\lambda\right]$, $m\mathbb{Z}$.

This algorithm relies on the fact that finite differences and modulo operations can somewhat commute at high order [162, Prop. 2]. In this sense, one can also see the US framework as an extension of Itoh's condition to higher orders.

Finally, the recovered displacement signal using the US-based recovery can be expressed as

$$\widehat{d}(t) = \mathrm{US}\left(\frac{\lambda}{2\pi}\arctan\left[\frac{\Im(s(t))}{\Re(s(t))}\right]\right), \tag{4.7}$$

where the US operator represents a function that executes the US algorithm.

4.2.5 Simulation Results

In order to assess the performance gain provided by the proposed US-based recovery method, Monte Carlo simulations were carried out.

Based on [28], the chest wall displacement due to breathing $d_{\mathrm{b}}(t)$ is modeled as a low-pass filtered periodic sequence of quadratic inspiration and exponential expiration. For modeling the heartbeat displacement $d_{\mathrm{h}}(t)$, a Gaussian pulse train is used [104], based on the idea that the heartbeat is a short explosive motion with a pulsatile nature. The initial phase of both displacements is generated randomly on each run. As an example, the breathing rate and amplitude were defined as 13 bpm and 12 mm, respectively, whereas for the heartbeat, we used 70 bpm and 0.5 mm, respectively.

The RBM interfering signal $d_{\mathrm{rbm}}(t)$ is constructed using three different models related to different types of body movements:

- First, the *ramp* body movement was defined as

$$d_{\mathrm{rbm}}(t) = a_{\mathrm{rbm}}\frac{(t-t_i)}{(t_f-t_i)}, \tag{4.8}$$

  where a_{rbm} is the movement's amplitude, and $t \in [t_i, t_f]$, with t_i and t_f being the initial and final time of the movement, respectively. This model could represent, for instance, a simple torso movement to the front.

- The second body movement follows a *sine* function and is defined as

$$d_{\mathrm{rbm}}(t) = a_{\mathrm{rbm}}\sin\left(2\pi f_{\mathrm{rbm}}(t-t_i)+\phi\right), \tag{4.9}$$

  where f_{rbm} is the movement's frequency and $\phi \in \mathcal{U}(-\pi,\pi)$ is the random initial phase. Here we are modeling a rocking (back-and-forth) motion of the torso, with controllable amplitude and frequency.

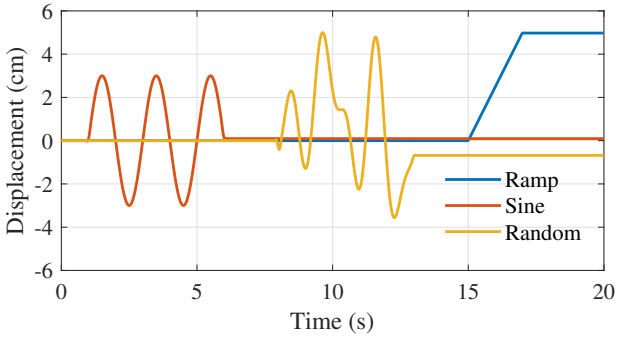

FIGURE 4.2: Illustration of simulated body movements.

- And finally, the *fully random* body movement, which is defined as

$$d_{\text{rbm}}(t) = a_{\text{rbm}} \frac{z(t)}{\|z(t)\|_\infty}, \tag{4.10}$$

  where $z(t)$ is a real signal whose spectrum is bandlimited at f_{rbm}, with each component of the non-zero spectrum being of unit amplitude with a random phase in $[0, 2\pi]$. This model does not impose any particular structure and more closely resembles an actual interfering body motion.

Figure 4.2 shows examples of the displacements generated by these models. The purpose of using these different models is twofold. First, by using the first and second models, we show that our approach can deal with body movements that are commonly occurring in day-to-day life and that can be easily modeled. Second, to avoid narrowing our study to specific movements, and to properly showcase the resilience of the US recovery to a broad range of movements, the *fully random* movement is used. Indeed, actual body movements have an inherent limit in their frequency content as they do not exhibit infinite acceleration. This makes the bandlimited RBM model appealing as it fits both the physics of the problem and the requirement of Theorem 4.1.

The composite displacement signal $d(t)$ is low-pass filtered and used to generate the slow-time complex samples according to (4.1), with the phase shift θ_0 being modeled as a random variable, *i.e.* $\theta_0 \in \mathcal{U}(-\pi, \pi)$. At each iteration, the generated signal is processed using the AD with the conventional unwrap operation or the proposed US-based recovery. From now on, we will refer to these methods simply as AD or US, respectively.

The reconstruction is tested for different amplitudes of the RBM, as well as for different slow-time sampling rates, in a Monte Carlo approach. The normalized recovery error (NRE) is then calculated as

$$\text{NRE} = 10 \log_{10} \left(\frac{\|\boldsymbol{d} - \widehat{\boldsymbol{d}}\|}{\|\boldsymbol{d}\|} \right), \tag{4.11}$$

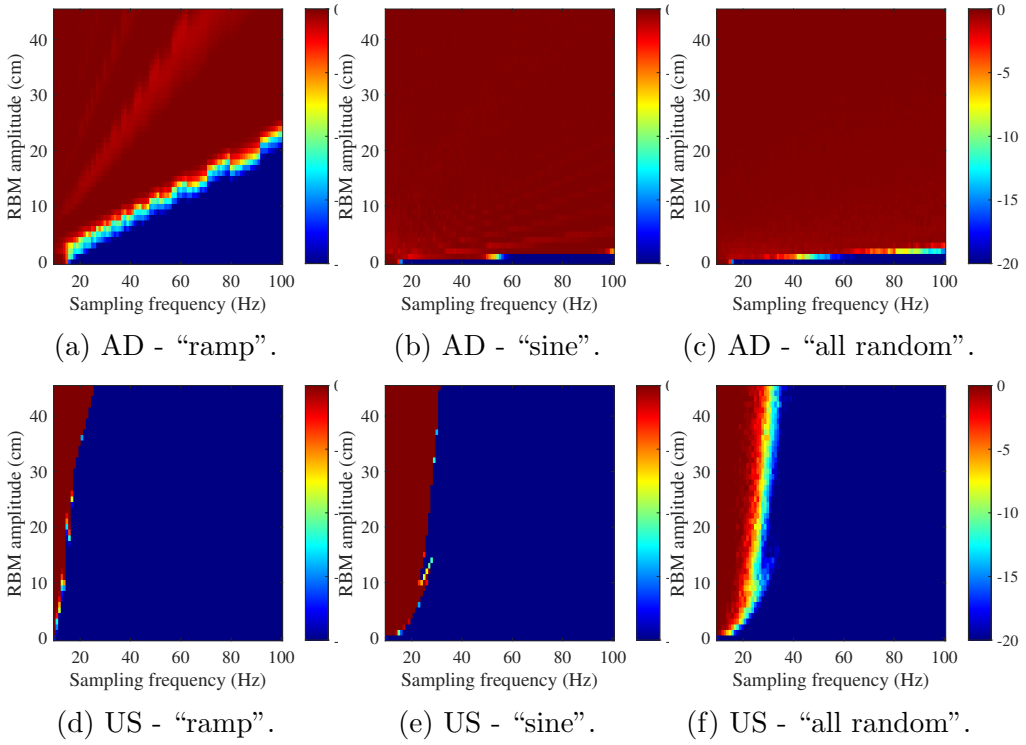

(a) AD - "ramp". (b) AD - "sine". (c) AD - "all random".

(d) US - "ramp". (e) US - "sine". (f) US - "all random".

FIGURE 4.3: Normalized recovery error (in dB) for different body movements.

where $\boldsymbol{d}$ and $\widehat{\boldsymbol{d}}$ represent the vectors with the true and recovered displacement signals, respectively. The final performance for each method is evaluated by averaging the NRE over all iterations, with 1000 runs being performed for each scenario. In this initial work, we are only evaluating the noiseless case.

Figure 4.3 shows the average NRE as a function of the slow-time sampling frequency and RBM amplitude, considering all the three simulated body movements, using an operating frequency of $f_c = 60$ GHz ($\lambda = 5$ mm). For easy interpretation of the results, the blue areas represent a perfect recovery of the displacement signal, while the red ones indicate regions of failure. The duration of the processing window was 20 seconds, and each movement started at the tenth second, with a duration of 2 seconds.

Figure 4.3a shows the performance of conventional unwrap for the *ramp* body movement. It can be seen that it follows the linear behavior stated in (4.4), *i.e.*, for precise phase recovery, the slow-time sampling rate needs to be increased linearly according to the amplitude of the interfering body movement. Figure 4.3d shows the performance when using the US framework. In this case, for recovering RBMs with the same amplitude, a much smaller slow-time sampling frequency can be used. In fact, after reaching a minimum value for the slow-time sampling frequency, the proposed algorithm can precisely recover the displacement signal, independent of the RBM amplitude. The

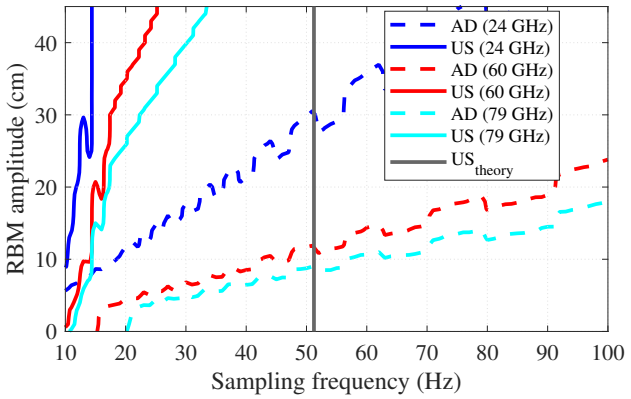

FIGURE 4.4: Normalized recovery error (threshold at -20 dB) for the ramp body movement, at different operating frequencies.

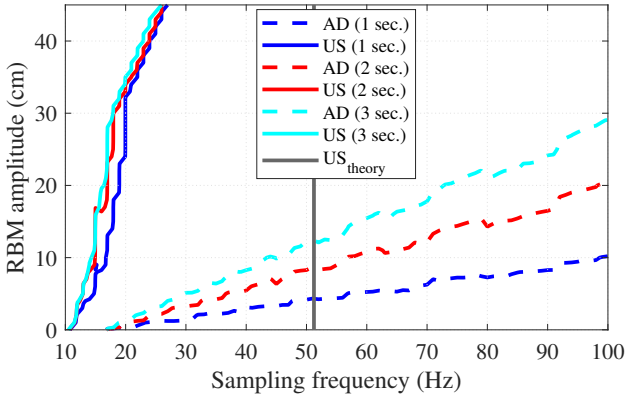

FIGURE 4.5: Normalized recovery error (threshold at -20 dB) for the ramp body movement, with different durations.

required sampling for perfect reconstruction only depends on the bandwidth of the signal of interest (not on its amplitude), which is consistent with Theorem 4.1.

Figures 4.3b and 4.3c show the performance of conventional unwrap for the *sine* and *fully random* body movements, with $f_{\text{rbm}} = 0.3$ Hz. In these cases, given the more complex behavior of the additional interference, even smaller amplitudes of RBMs completely prevent successful recovery of the displacement signal, which would require much higher sampling rates. On the other hand, it can be seen in Figs. 4.3e and 4.3f, that the US-based method provides a large improvement compared to conventional unwrap, with minor degradation at larger amplitudes of the RBM. It only fails when the slow-time sampling frequency is lower than 20 Hz and 30 Hz for the *sine* and *fully random* body movements, respectively. Therefore, it extends the resilience of the recovery process when encountering random body movements at comparable sampling rates.

It is important to mention that, if f_{rbm} does not overlap with vital sign frequencies, accurate recovery of the displacement signal using the US would allow easy filtering of the RBM interference by conventional spectral analysis. However, incorrect demodulation

using the conventional unwrap algorithm may introduce nonlinear errors that can hinder filtering and prevent subsequent estimation, even under the simplest RBM interference.

Figure 4.4 shows −20 dB threshold lines in the NRE (perfect recovery below the lines), for the *ramp* body movement with the same parameters as before, now at different operating frequencies. It can be seen that, under the RBM interference, the AD performance decreases at higher operating frequencies. At 60 GHz and 79 GHz for instance, the AD cannot recover RBMs with amplitudes larger than 20 cm, even if oversampling at 100 Hz. Conversely, the US method provides perfect recovery of a 20 cm RBM using a slow-time sampling frequency lower than 25 Hz or 35 Hz, at 60 GHz and 79 GHz, respectively.

Finally, Fig. 4.5 shows the −20 dB threshold lines for the same *ramp* body movement, but now with different durations. Reducing the duration to reach the same amplitude is equivalent to increasing the movement velocity. In these cases, the AD with conventional unwrap follows Itoh's condition with performance degradation at higher velocities, whereas unwrapping with the US method is independent of the velocity variation and can provide perfect recovery until 45 cm with less than 30 Hz of slow-time sampling frequency. This sampling rate is also below the upper-bounded sampling rate predicted by Theorem 4.1 represented by the gray line in Fig. 4.4 and Fig. 4.5.

4.2.6 Conclusion

We proposed in this paper the use of a novel framework for recovering vital signs from radar measurements. The proposed method relies on the US framework, for being able to tackle the recovery of signals whose measurements are folded. We first introduced the AD with the conventional unwrap operation, which has limitations to recover the embedded phase, especially under the presence of interfering body movements. Leveraging the fact that these movements are, because of their human nature, bandlimited, we showed that the US provides an attractive alternative for the successful recovery of the displacement signal. The simulation results confirmed that the required sampling rate for the US to succeed was far inferior to the conventional unwrap and, more importantly, independent of the amplitude of the movement. Future work will extend this initial analysis to noisy scenarios and, further, to practical measurements using radar sensors.

Chapter 5

Filtering

5.1 Preamble

In this chapter, we will focus on the filtering stage. As discussed in Section 2.4.3, the goal of this block is to filter any interfering components still present in the chest wall displacement signal, thus allowing accurate estimation of the breathing and heart rates in the subsequent signal processing stage.

Here we present a manuscript that shows our work at the NICU, where we monitored the respiration of premature babies in a real clinical environment. For the first time, different scenarios common to the NICU daily routine were investigated, irrespective of the amount of RBMs or external interference.

By using a novel RBM mitigation technique, the proposed radar-based solution was able to precisely recover the chest wall motion. This allowed clear identification of different breathing patterns and reliable breathing rate estimation most of the time. These results can be interpreted as a proof-of-principle that a radar-based approach has the potential for contactless breathing monitoring in NICUs.

5.2 Manuscript: Contactless radar-based breathing monitoring of premature infants in the neonatal intensive care unit

Gabriel Beltrão[1], Regine Stutz[2], Franziska Hornberger[2], Wallace A. Martins[1], Dimitri Tatarinov[3], Mohammad Alaee-Kerahroodi[1], Ulrike Lindner[2], Lilly Stock[2], Elisabeth Kaiser[2], Sybelle Goedicke-Fritz[2], Udo Schroeder[3], Bhavani Shankar M.R.[1], Michael Zemlin[2]

[1] SnT - Interdisciplinary Centre for Security, Reliability and Trust, University of Luxembourg
[2] Department of General Pediatrics and Neonatology, Saarland University Medical School, Homburg.
[3] IEE S/A, Luxembourg

Published in: Nature *Scientific Reports* **12**, 5150, 2022.
DOI: 10.1038/s41598-022-08836-3

This section is a copy of the paper referenced above.

Abstract

Vital signs monitoring systems are essential in the care of hospitalized neonates. Due to the immaturity of their organs and immune system, premature infants require continuous monitoring of their vital parameters, and sensors need to be directly attached to their fragile skin. Besides mobility restrictions and stress, these sensors often cause skin irritation and may lead to pressure necrosis. In this work, we show that a contactless radar-based approach is viable for breathing monitoring in the Neonatal Intensive Care Unit (NICU). For the first time, different scenarios common to the NICU daily routine are investigated, and the challenges of monitoring in a real clinical setup are addressed through different contributions in the signal processing framework. Rather than just discarding measurements under strong interference, we present a novel random body movement mitigation technique based on the time-frequency decomposition of the recovered signal. In addition, we propose a simple and accurate frequency estimator which explores the harmonic structure of the breathing signal. As a result, the proposed radar-based solution is able to provide reliable breathing frequency estimation, which is close to the reference cabled device values most of the time. Our findings shed light on the strengths and limitations of this technology and lay the foundation for future studies toward a completely contactless solution for vital signs monitoring.

5.2.1 Introduction

Nearly 15 million infants are born annually before the 37^{th} week of pregnancy, meaning that about 10% of all births worldwide are premature [170]. Due to their immature organ systems and associated functions, as well as their immune system, these infants are at a

higher risk of infections, chronic diseases and respiratory problems. The immaturity of breathing regulation and lungs often lead to apnea-bradycardia and respiratory distress syndromes. This is commonly followed by bronchopulmonary dysplasia in 27% of the infants born at less than 30 weeks of gestation [171–174]. Consequently, further development of these premature infants has to continue *ex-utero*, and they usually have to spend several weeks at a NICU.

During this period, continuous monitoring of their underdeveloped organs is necessary. Often, newborns are dependent on parenteral nutrition, respiratory support, and invasive diagnostic interventions which, albeit being essential for survival, may cause stress to the child. Basic vital parameters such as respiration, heart rate and oxygen saturation also need to be monitored. To this end, several sensors are directly attached to their fragile skin and connected to the monitoring systems through cables. Besides mobility restrictions, these sensors often cause skin irritation and may eventually lead to pressure necrosis [5–10].

In order to promote the development of premature babies, a number of efforts have been made toward non-invasive monitoring and diagnostic solutions. The use of sensors that can monitor a variety of vital signs without a cable connection, but bonded to the skin, is being investigated in [175, 176]. Current studies are also investigating the potential of different non-contact techniques for non-invasive diagnostics in children. Efforts are underway to detect pathological changes in body excretions by analyzing volatile organic compounds [177, 178]. There are approaches using optical methods to monitor the pulse rate and oxygen saturation without direct skin contact and cable connection, based on e.g. dynamic light scattering [179], video [84] or photoplethysmography [180, 181]. Of high relevance for preterm infants is also the diagnosis of respiratory pathologies and classification regarding periodic breathing and apneas [182, 183]. This task is addressed using different non-contact techniques, which require redundant measurements of various vital signs, e.g. respiration motion, heart rate, oxygen saturation or nasal breathing [184–186].

The contactless monitoring of the cardiorespiratory activity neither confines nor inhibits the patient, reduces hygiene risks and does not cause any discomfort, irritation or skin damage [15, 75]. In this context, radars have already been proven to be a promising technology [12, 16, 76], being intrinsically low-power, low-cost and privacy preserving. Unlike camera-based systems [83, 87], radar signals can penetrate through different materials (such as plexiglass, clothing, mattresses and blankets), and are not affected by skin pigmentation or ambient light levels. However, due to the reduced transmitted power, these signals can be easily buried in the background noise, or masked by stronger external interference, including body movements from the monitored patient [93]. This

interference is a major challenge for accurate estimation in contactless solutions as well as for cabled devices. Specific signal processing techniques are thus needed in order to ensure reliable and robust measurements.

Recent works [94, 125] have demonstrated that an ultrawideband radar can provide reliable breathing rate estimates for neonates under specific conditions. However, these investigations were limited to a single scenario, where the neonates were lying over an open-air crib, always in supine position. In addition, radar performance was evaluated only during minimal movements of the monitored patients. In this article, we take one step further by using a simpler CW radar device, and investigating premature infants under different scenarios common to the NICU routine, irrespective of the amount of movement or external interference. The specificity of the monitored patients in a real clinical setup creates several challenges which were addressed through different contributions in the proposed signal processing framework. Particularly, rather than just discarding measurements under strong interference [94, 125–128], we present a novel random body movement mitigation technique based on the time-frequency decomposition of the recovered signal. Additionally, we propose a simple and accurate frequency estimator, which explores the harmonic structure of the breathing signal.

5.2.2 Problem formulation

The activity of the cardiovascular and respiratory systems causes some physical and physiological effects on the human body. The chest wall moves during the inspiration/expiration cycle as a result of the diaphragm and intercostal muscle movement. This small and periodic displacement can be detected by radar, allowing accurate estimation of the breathing rate under certain conditions. Figure 5.1a illustrates the basic operational principle of a CW radar. The transmitted signal propagates through the free space and reaches every object in the radar's field-of-view, being reflected back with additional phase information regarding each object's position. The received signal can thus be modeled as a scaled and time-shifted version of the transmitted signal, in which the phase variation over time contains valuable information regarding the scene movement. This time-varying phase $\theta(t)$ can usually be recovered as

$$\theta(t) = \frac{4\pi d(t)}{\lambda}, \tag{5.1}$$

where λ is the radar operating wavelength, and $d(t)$ represents the displacement signal which, ideally, would correspond only to the chest wall motion due to the breathing mechanism. As seen by the radar, this movement is mainly originated by the reflected points over the chest moving surface, but it may additionally include residual motion

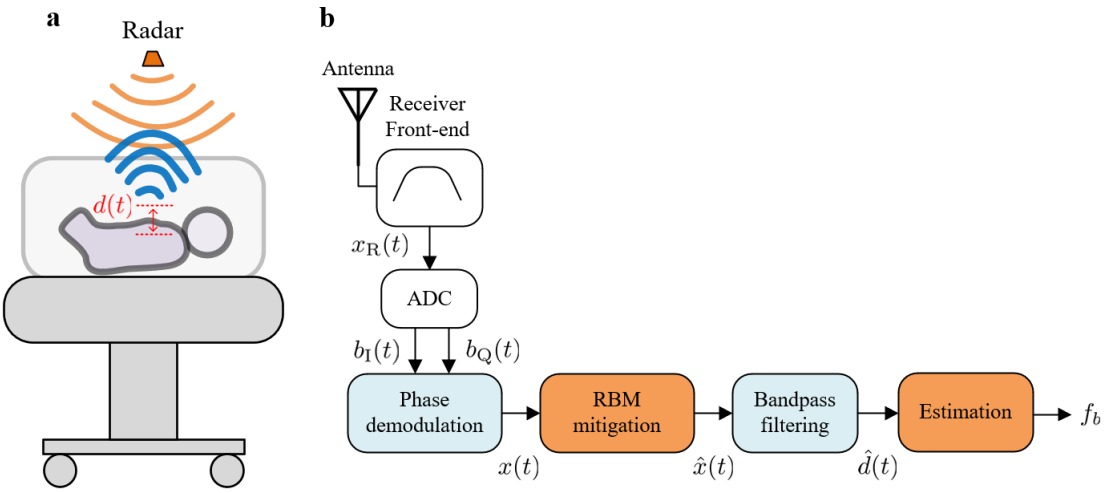

FIGURE 5.1: **Continuous-wave radar for breathing monitoring in the NICU.** **a**, Basic operational principle. **b**, Block diagram of the signal processing chain. Before estimation, the received signals from the ADC are phase demodulated and further processed in the RBM mitigation unit.

from the belly, sides and the back, depending on the patient relative position. In healthy adults, standard amplitudes for this motion range between 4 mm to 12 mm [102], with breathing rates varying from 5 to 25 breaths per minute (bpm) [187]. For premature infants, these amplitudes can be smaller than 1 mm, while the average breathing rate can normally reach 60 bpm [30], and go up to 80 bpm under specific conditions [31].

Perfect recovery of the chest wall motion $d(t)$ would allow precise estimation of the breathing frequency f_b by simple analysis of the movement periodicity. However, in a real clinical setup, besides unavoidable hardware imperfections, the received radar signal is usually mixed with additional reflections from the external environment, arising not only from different body movements of the monitored patient, but also from every moving object in the scene. These interfering signals are usually much stronger than those induced by the chest wall millimeter displacement, and this makes accurate recovery and subsequent estimation of the breathing frequency a challenging task. In addition, when considering premature infants, the reduced amplitudes of the chest wall motion, and the wider range of possible breathing rates pose an additional signal processing challenge in relation to previously reported research with adults.

5.2.3 Clinical setup and protocol

The study was performed in the Department of Pediatrics, at the Saarland University Medical Center (Homburg, Germany). Figure 5.2a shows a premature neonate being monitored with the conventional method. Besides the sensors attached to the chest and abdomen, and connected by cables to the central monitoring unit (for oxygen saturation,

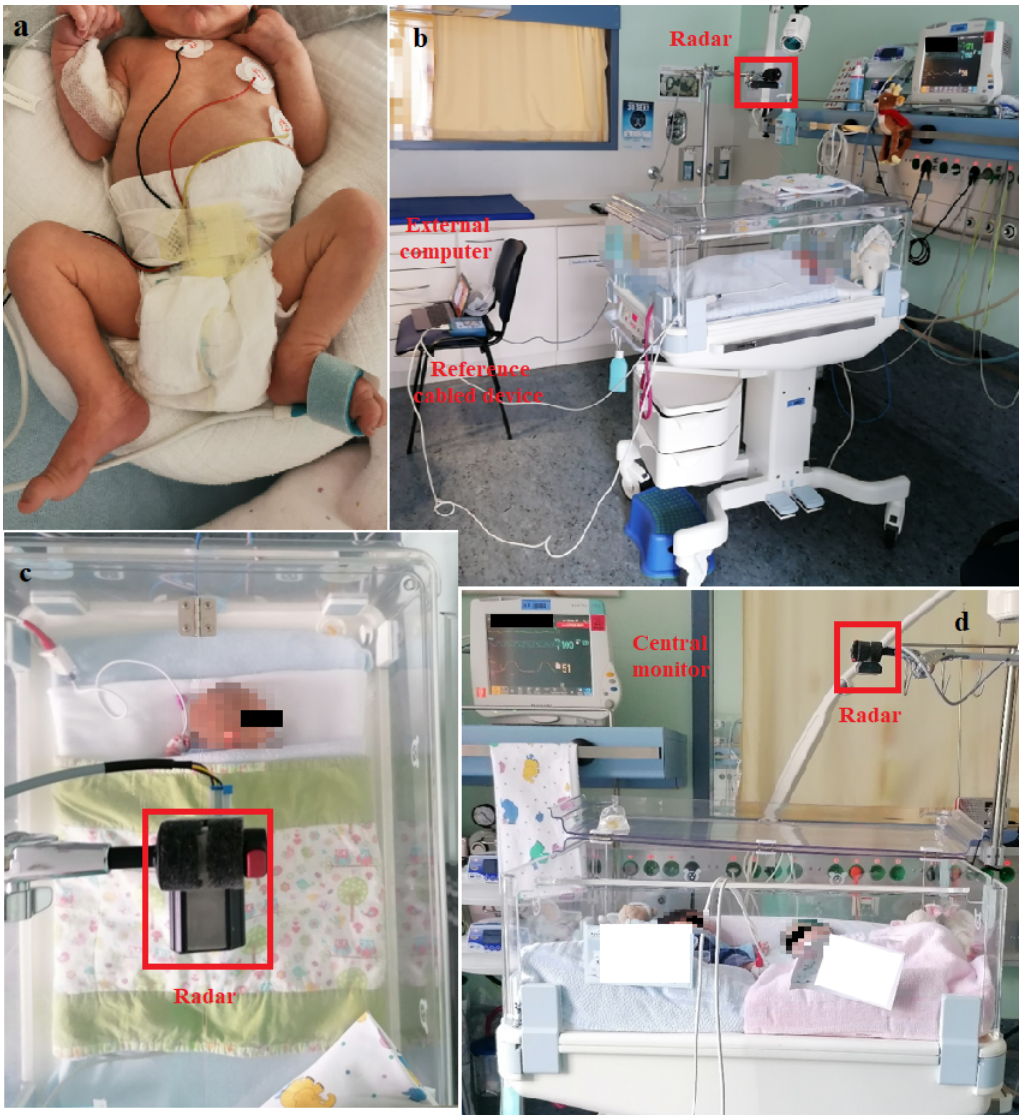

FIGURE 5.2: **Clinical setup.** **a**, Conventional monitoring of premature neonate: connection by cables to the central monitoring unit (heart rate, oxygen saturation, respiration), and an additional peripheral venous catheter. **b**, NICU room view. Both radar and the reference cabled device were controlled from the external computer. **c**, Close top view. The radar was attached to a low-vibration tripod, 45 cm away from the infant. **d**, Close side view with twins sharing the same bed.

heart rate, and respiration), an additional peripheral venous catheter and a gastric tube are also necessary in this stage. The clinical setup, including the neonatal cot, the radar device, and the reference monitoring system is shown in Figure 5.2b-d. The radar is certified for operation in the 24-GHz ISM band, and it was installed outside the cot, attached to a low-vibration tripod. The relative distance to the monitored infant was around 45 cm to 50 cm. Due to the radar's inherent capabilities, no modification to the cot structure was necessary, and the plastic cover could remain closed during the measurements. In Fig. 5.2d, twins are sharing the same bed, with only one being monitored with the contactless method. Cobedding of twins is a common procedure in

the NICU, with several studies reporting physiological benefits to the infants [188, 189].

A total of 12 premature infants were included in the study. The Supplementary Table 1 shows a summary of the patient's information. They were selected on the basis of medical opinion, and taking into account the medical safety of participating in the study. For each infant, the measurements were carried out in three different days, at noon (after feeding), over a period of 25 minutes each. Their natural position was not changed during each measurement. Besides the supine (with the chest facing the radar), prone (with the back facing the radar) and side positions, we have also investigated cobedding cases with only one infant being monitored using the contactless method. The idea was to investigate the different effects when collecting radar data from the chest/abdomen and back. Additionally, if monitoring twins is possible, and what would be a safe distance (in terms of radar interference) between them. The basic principle that guided the data collection protocol was to ensure seamless operation at the NICU. A detailed description of the patient's protocols is shown in Supplementary Tables 2a-d, including all interventions and additional transients manually annotated during the measurements.

5.2.4 Signal processing background

Figure 5.1b shows the basic block diagram of the signal processing chain. The initial signal processing step for CW systems is commonly known as phase demodulation. It is essentially the process where the received in-phase and quadrature (I and Q) signals from the radar's ADC are combined with the aim to recover the displacement signal $d(t)$. Among several methods, the two most used are the AD [117] and the CSD [116]. While the AD enables precise recovery of the chest wall motion, it is highly sensitive to hardware calibration, and to the presence of DC offsets, noise, and external interference. The CSD is more robust to these effects, but it relies on small displacements for recovering an approximation of the breathing motion (please refer to the Methods[1]).

Figure 5.3 shows examples of the recovered breathing motion from radar data, in comparison to the actual (reference) displacement acquired from the cabled device. Initially, to precisely reconstruct the chest wall displacement, we selected "clean" segments of data (no external interference), and the AD was used in both cases. While Fig. 5.3a depicts a normal breathing pattern obtained at supine position, Fig. 5.3b shows an occurrence of the Cheyne-Stokes (periodic) breathing pattern [36], with the infant at prone position. This special form of breathing is physiologically found in neonates, and is defined by a cyclic variation between hyperpnea and hypopnea [190–192], i.e. repetitive

[1] In Section 5.2.8

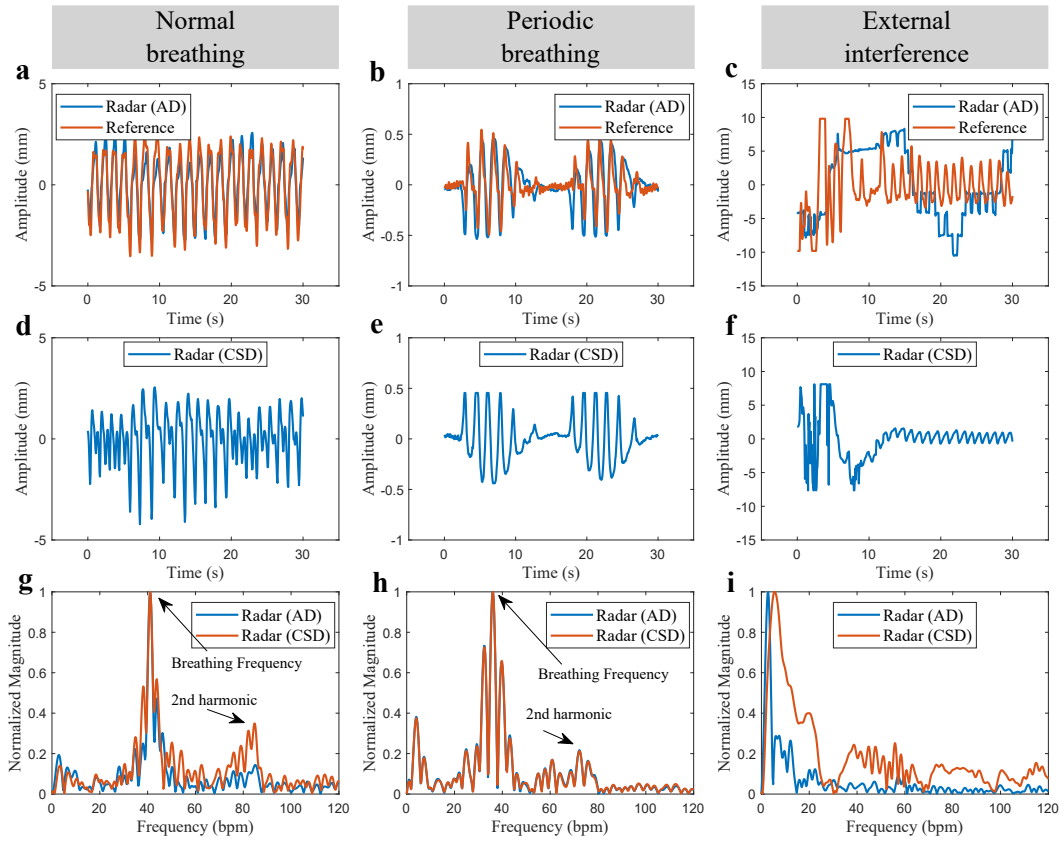

FIGURE 5.3: **Recovered chest wall motion with different breathing patterns.** **a**, Normal breathing pattern, under good conditions (no interference). **b**, Periodic (Cheyne-Stokes) breathing pattern. **c**, Normal breathing pattern corrupted by external interference and ADC saturation. **d-f**, Approximation using the CSD. **g-i**, Spectrum comparing AD and CSD.

short cycles of pauses and breaths. Despite small differences between the recovered radar signals and the reference device, the periodic breathing movement can still be clearly identified in both cases. The small amplitudes of the chest wall motion can also be visualized, with displacements around 2 mm in supine position and 0.5 mm in prone position. These amplitudes are well below typical values for adults reported in previous research [50, 54, 193].

The approximated breathing motion, obtained with the CSD, is shown in Fig. 5.3d,e. Despite noticeable differences when compared to the AD, Fig. 5.3g,h show that both techniques yield signals with the same fundamental frequency, corresponding to the average breathing frequency. Given the small displacements we aim to detect, and the challenging conditions of this real clinical environment, the CSD was adopted in our solution for long-term monitoring. The harmonic structure of the breathing signal can also be visualized, with the second harmonic being clearly distinguishable. This harmonic structure can be used for improving estimation, as we will show latter. However, as depicted in Fig. 5.3c,f,i, under external interference and eventual ADC saturation, both

demodulation methods fail to reconstruct the chest wall motion. The spectrum becomes dominated by the interference components, which will then prevent accurate breathing frequency estimation. Therefore, additional processing is necessary in order to attenuate these interfering effects.

5.2.5 Random body movement mitigation

Most research on contactless vital sign monitoring with radar sensors focus on a single-person setup under ideal motionless conditions [95]. In practical monitoring situations, the subject may often move body parts like hands, legs or torso, and even the entire body. These unwanted but unavoidable movements are usually called RBMs. The amplitude of their reflected signals is often much stronger than the millimeter-scale breathing motion, which will potentially be masked by this interference. Since spontaneous RBMs are inevitable, solving this problem is fundamental to reliable vital sign detection in practical applications.

Several methods for RBM mitigation were already proposed [123], and even though specific types of movements could be effectively cancelled out, they usually require more complex systems. Most solutions rely on additional or duplicated hardware, thus suffering from practical limitations such as misalignment, synchronization, and cost [116, 194, 195]. Another direction of research basically tries to identify segments of vital sign data with RBMs, and simply discard these corrupted segments before estimation [94, 125–128]. However, depending on the processing window duration, even very short RBMs will affect several seconds of good signal. Therefore, rather than simply discarding segments of data, an approach which allows useful exploitation of these episodes with moderate RBMs is desired. Recent work has begun to address RBMs using a single sensor and within more challenging scenarios [93]. Nonetheless, experimental validation is still performed under controlled situations, with RBMs being emulated through predefined behavior, which results in limited interference over the desired signal.

First, let us assume that RBMs are sparse, i.e. they are not frequent and, when they occur, their duration is small in relation to the observed time window. This contrasts with the constant and periodic nature of the breathing movement. Additionally, their amplitudes are usually much stronger than the standard breathing signal. These specific time and frequency features will be present in the spectrogram of the recovered signal, which can be analyzed toward identifying and possibly removing this interference. For addressing this, we will use the NMF [196, 197], a matrix decomposition technique usually employed for extracting features from a set of nonnegative data. If $x(t)$ (Fig. 5.1b) is the recovered signal containing the chest wall motion and eventual RBM interference, its

magnitude spectrogram $|\boldsymbol{X}|$ can be obtained through the STFT of $x(t)$. The NMF will then decompose $|\boldsymbol{X}|$ as

$$|\boldsymbol{X}| \approx \boldsymbol{W}\boldsymbol{H} = \sum_{i=1}^{K} \boldsymbol{w}_i \boldsymbol{h}_i^{\mathrm{T}}, \tag{5.2}$$

where the matrices $\boldsymbol{H}$ and $\boldsymbol{W}$ contain, respectively, the associated time and frequency basis components of $|\boldsymbol{X}|$, with K being a predefined number of basis. In other words, $\boldsymbol{W}$ can be seen as the set of frequency templates of $|\boldsymbol{X}|$, while $\boldsymbol{H}$ contains the timing information related to the activation of each of these templates. If we look into the time activation matrix $\boldsymbol{H}$, the basis components with sparse behavior and higher amplitudes will often indicate the epochs when the RBM interference is present. Despite the unpredictable frequency spectrum, which will eventually overlap with breathing frequencies, the RBM distinct time behavior can be captured by the NMF time activation bases $\boldsymbol{H}$, whereas the corresponding basis in $\boldsymbol{W}$ will retain its frequency content. This allows additional flexibility for filtering the RBM interference when compared to standard spectral analysis methods. We can thus reconstruct the filtered spectrogram $\widehat{|\boldsymbol{X}|}$, by simply adding back all the $\boldsymbol{w}_i \boldsymbol{h}_i^{\mathrm{T}}$ matrices, except for the ones containing the interfering components.

Figure 5.4a shows a 60-second processing window for illustrative purposes, where the recovered signal $x(t)$ (after CSD) is corrupted by segments of RBMs, with its normalized spectrogram $|\boldsymbol{X}|$ in Fig. 5.4b. In the case of the CSD, the spectrogram is calculated based on the complex samples of the recovered signal $x(t)$, and therefore considers both I and Q channels simultaneously. The NMF decomposition into $K = 11$ frequency ($\boldsymbol{W}$) and time basis ($\boldsymbol{H}$) components is depicted in Fig. 5.4c,d. Each color represents a pair of basis components, with the frequency content in Fig. 5.4c, and the corresponding time activation in Fig. 5.4d. It can be seen that (please refer to the green and blue bases for instance), due to its random nature, the RBM interference has frequency components spread over the entire spectrum, overlapping with the breathing frequency region. While a variety of frequencies can be visualized in $\boldsymbol{W}$, the sparse and strong bases corresponding to RBMs can be clearly identified in $\boldsymbol{H}$ (please refer to the Methods[1]). Removing the selected bases allows the reconstruction of the filtered spectrogram in Fig. 5.4e, where the breathing frequency variation over time (around 45 bpm) is now evident. After the inverse STFT, the RBM filtered time signal is depicted in Fig. 5.4f. Finally, Fig. 5.4g shows the bandpass spectrum of both the original and the RBM filtered signals. The corresponding detected values are highlighted respectively with the blue and red markers. The dashed black line shows the reference value for the average breathing frequency associated with this processing window. Because of the strong RBM interference, the

[1] In Section 5.2.8

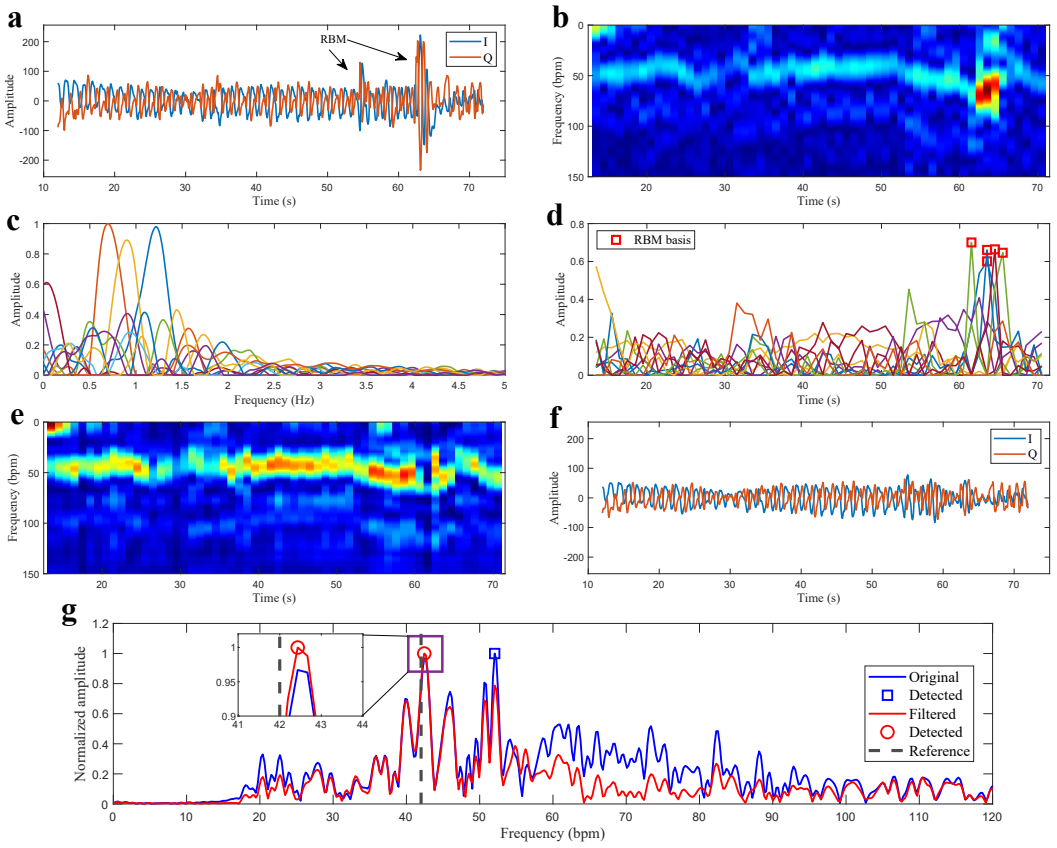

FIGURE 5.4: **NMF for random body motion mitigation.** **a**, I and Q samples of the displacement signal $x(t)$, corrupted by RBMs. **b**, Normalized spectrogram $|\boldsymbol{X}|$. The RBM interference clearly dominates the spectrum and would jeopardize estimation. **c**, NMF decomposition into the frequency basis components in $\boldsymbol{W}$. **d**, NMF decomposition into the time basis components in $\boldsymbol{H}$. **e**, RBM filtered spectrogram $|\widehat{\boldsymbol{X}}|$. **f**, I and Q samples of the RBM filtered time signal $\widehat{x}(t)$. **g**, Bandpass spectrum of the original and RBM filtered signals.

maximum value of the original spectrum would indicate an erroneous breathing frequency of 52.1 bpm, very distant from the true value of 42 bpm. After RBM filtering with the NMF, the modified spectrum indicates a closer value of 42.4 bpm, where the estimation error would be only 0.4 bpm.

5.2.6 Breathing rate estimation

Different models have already been proposed for representing the back-and-forth breathing movement $d(t)$, from simple sinusoidal approximations [98, 99], to more complicated patterns as described in [28, 102]. The breathing movement is a complex phenomenon which involves different patterns of motion, not only from the chest wall surface, but also from the belly, shoulders and back [96, 97]. Therefore, it is difficult to identify time-domain models that fully characterize it in a robust way, for every subject and monitoring scenario. However, due to the inherent periodic nature of breathing, any

function representing this movement can eventually be decomposed into Fourier terms, containing the fundamental frequency and harmonics that correspond to the breathing rates we aim to estimate. Hence, the displacement signal can be modeled as a sum of harmonically related complex sinusoids, having frequencies that are integer multiples of the fundamental breathing frequency. To better exploit this harmonic structure, in this section we propose a simple and accurate NLS estimator [198], which is asymptotically efficient for large processing windows, even in colored noise scenarios [199].

Initially, for removing any residual DC values, and possible high frequency noise components, the RBM-filtered displacement signal $\widehat{x}(t)$ is further filtered using a bandpass Kaiser window ($\beta = 6.5$), from 0.3 Hz to 3 Hz ($18 - 180$ bpm). This corresponds to the physiological range of breathing frequencies, also including possible harmonics. The bandpass filtered signal $\widehat{d}(t)$ will ideally be an accurate approximation of the true chest wall motion $d(t)$ (Fig. 5.1), and can finally be used for breathing frequency estimation.

Before estimation, for improving the SNR [104, 200, 201], we calculate the autocorrelation function $r(t)$ of the bandpass filtered signal. The estimation is first performed in time domain, directly over the autocorrelated signal. An initial (coarse) estimation is obtained through a peak detection algorithm, where the time distance between peaks provides an estimation of the time between each breath. Eventually, detected peaks can be excluded if the distance to its neighbors correspond to a frequency outside the expected physiological range. The initial breathing frequency is thus calculated as the inverse of the time between selected peaks, averaged over the entire processing window. This initial estimation will be used to simplify the NLS algorithm.

The following step is to calculate the NLS frequency estimates $\widehat{\omega}$, which are obtained by maximizing the similarity between $\widehat{d}(t)$ and the displacement signal model in (5.12). Under certain conditions (please refer to the Methods[1]), the solution to this problem (the resulting cost function in (5.17)) can be efficiently implemented using the Fast Fourier Transform (FFT) and a linear grid search algorithm [202], where the estimator reduces to a summation of breathing harmonics over the power spectral density of $\widehat{d}(t)$. The initial time domain estimation is used for limiting the search range, thus avoiding stronger low-frequency components which may still be present in real data. This strategy also reduces the computational effort to perform the grid search.

Experimental results

The initial measurements were used for setting up the ideal distance between radar and the monitored infant (Supplementary Fig. 1). From a total of 30 measurements at the

[1] In Section 5.2.8

adjusted position (around 45 cm), 3 were excluded due to recording issues with the devices. The remaining sequences were processed using sliding windows of 30 seconds, with 28 seconds of overlap, leading to updated breathing rate estimates every 2 seconds. This resulted in approximately 20,250 estimates, from 675 minutes of analyzed data. The measurements proceeded irrespective of the amount of movement or external interference. The sequences include moments with hiccups, yawn, cry, grunt, periodic breathing, and also additional movements from the NICU room, e.g. medical interventions and visitors (Supplementary File 3). All the data processing was performed using Matlab [203].

Figure 5.5 shows examples of I and Q samples from the radar's ADC, the estimated breathing frequency values, and the reference values from the cabled device. In Fig. 5.5a, the monitored infant was sleeping calmly, in supine position, and a nurse was present in the NICU room during the entire measurement, 2.5 meters away from the baby. These conditions resulted in good radar measurements with low level of interference. On the other hand, Fig. 5.5b shows one example where the infant was lying in prone position. In this case, several segments of strong interference can be visualized in the I/Q input data. Besides the infant moving freely and grunting, a nurse was also present during this measurement, from minute 9 and onwards. Figure 5.5c corresponds to one of the twin cases. A direct intervention over the monitored infant was registered around the third minute, for fastening the oxygen saturation sensor. The second twin was sleeping calmly during the entire measurement. The distance between them was around 20 cm. Figure 5.5d shows another example of a highly interfered sequence, where the monitored infant was constantly moving and accompanied by the mother, just 1 meter away. In this case, long segments of strong interference (and eventual ADC saturation) can be visualized.

Importantly, when the babies were moving, a high level of saturation was also observed in the reference cabled device data. During saturation, the ADC clips the input signal at the maximum allowed magnitude, generating segments of constant amplitude that increase the low-frequency content of the current processing window. This limitation results in a rapid decrease in the reference breathing frequency values (valleys), followed by an immediate recovery to the correct values just after saturation ends (these valleys are highlighted in Fig. 5.5b,d). This anomalous behavior is not related to any physiological pattern, and indicates that the reference device is not reliable in these moments. Consequently, for calculating the performance metrics, we have only considered the processing windows correspondent to non-saturated data segments of the reference device. This resulted in 18 valid measurements and approximately 4,964 valid breathing rate estimates. The measurements from the side position resulted in low SNR and unreliable estimates that were also discarded. On the other hand, radar saturation is being considered inherent to the measurement setup. Therefore, radar data segments with saturated I and/or Q samples are being considered valid and processed.

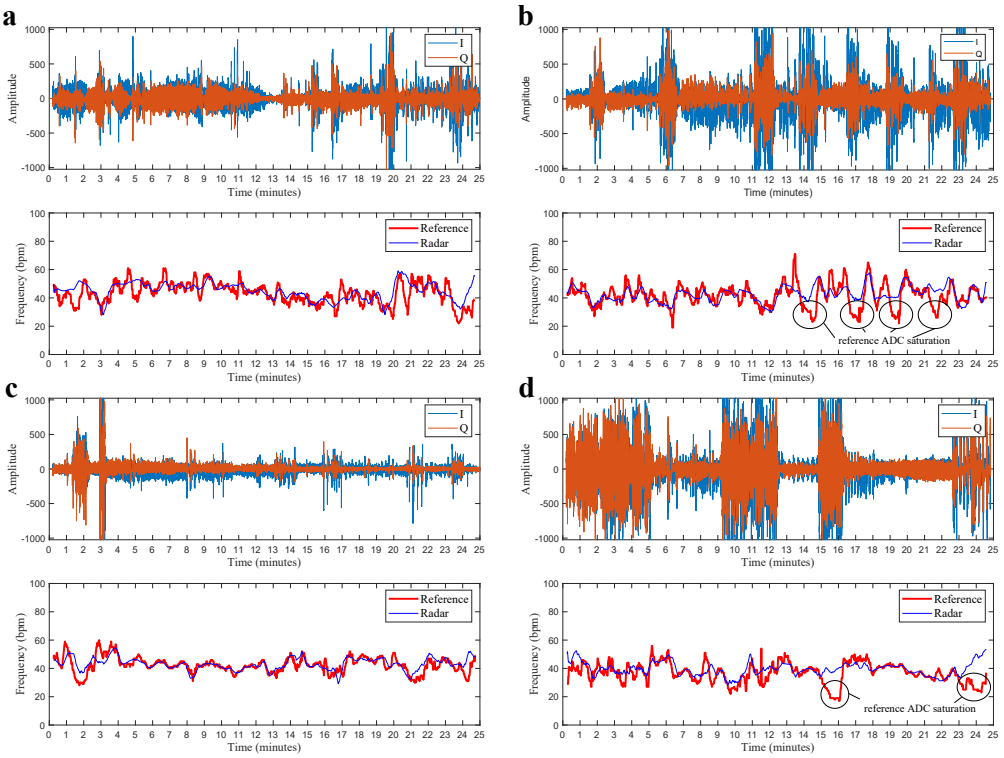

FIGURE 5.5: **Radar input data and estimated breathing rate.** All sequences were processed with the complete proposed solution (NLS+NMF), and each one represents a different monitoring scenario. **a**, Single infant in supine position (chest facing the radar). **b**, Single infant in prone position (back facing the radar). **c**, Twins in the same bed, spaced by 20 cm, with the monitored infant in prone position. **d**, Highly interfered sequence.

A summary of the obtained results is presented in Fig. 5.6. Figure 5.6a-d shows the final average accuracy, in each of the investigated scenarios, namely: (a) supine position (11 measurements), (b) prone position (7 measurements), (c) single infant in the warming bed (14 measurements) and (d) twins sharing the same bed (4 measurements). These scenarios are not exclusive. Supine and prone scenarios include single/twins cases and vice-versa. The bars compare the performance of three different algorithms: (i) conventional estimation using the DFT [107, 147, 204], representing the benchmark; (ii) the proposed NLS estimation (NLS); and (iii) the complete proposed solution (NLS+NMF), including the NMF-based RBM mitigation algorithm. The same preprocessing steps (phase demodulation and bandpass filtering) were used in all cases. The accuracy is being calculated as the percentage of time (in terms of valid processed windows) during which the final estimation from the radar is within a predefined error interval. For each case, the 3, 6 and 10 bpm accuracy intervals were considered. For instance, a 6 bpm accuracy of 80% means that the magnitude of the error between radar estimation and the reference device was smaller than 6 bpm for 80% of the time.

It can be seen that the proposed techniques provided substantial improvement in all

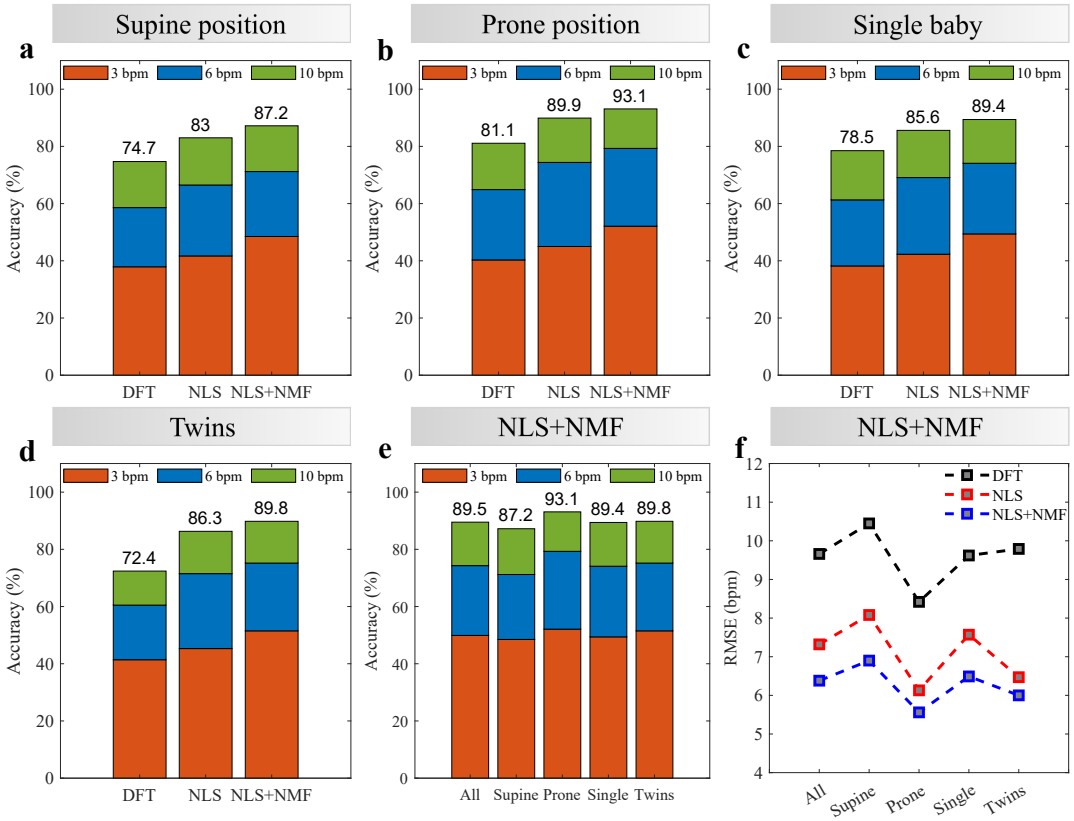

FIGURE 5.6: **Summary of results, considering all processed sequences for each scenario, and comparing different techniques: standard DFT estimation (DFT), the proposed NLS estimation (NLS), and the complete proposed solution, with RBM mitigation (NLS+NMF).** Average accuracy for different techniques. **a**, Supine position. **b**, Prone position. **c**, Single infant in the cot. **d**, Twins sharing the cot. **e**, Average accuracy for different scenarios, considering the complete proposed solution (NLS+NMF). **f**, Average RMSE for different scenarios and different techniques.

cases, with up to 17% of enhancement, and reaching a maximum 6 and 10 bpm accuracy of 79.3% and 93.1% respectively, in prone position. Figure 5.6e directly compares the performance of the complete proposed solution in each scenario, also including the average result of all processed sequences. An interesting outcome is related to the fact that the prone position produced on average the best results, even though the displacements verified from the back were smaller than the ones from the chest/abdominal region. This could be a result of the more uniform breathing motion of the posterior chest wall, since the ossification of the ribs begins at the back. Due to the higher flexibility of the anterior chest wall, abdominal and thoracic movements yield a more heterogeneous motion, thus making radar estimation more difficult. In addition, the prone position might lead to reduced body movements, thus reducing interference. Lastly, single and twin cases provided on average similar results, thus indicating that a second infant in the cot may not directly impact radar performance.

The RMSE of each sequence was also calculated, and the average values for each scenario

are presented in Fig. 5.6f, comparing the proposed techniques with the conventional DFT estimation. The RMSE is defined as

$$\text{RMSE} = \sqrt{\frac{1}{N}\sum_{n=0}^{N-1}(B_n - \widehat{B_n})^2}, \tag{5.3}$$

where B_n and $\widehat{B_n}$ represent, respectively, the reference and estimated breathing rates (in bpm), in the n^{th} processing window. It can be seen how the proposed solution outperforms the standard approach, providing significant and robust improvement over the different scenarios, reducing the RMSE in all cases. The overall RMSE considering all valid measurements was 6.38 bpm. The measurements in prone position resulted in the best performance, with a RMSE close to 5 bpm. Supplementary File 4 shows the Bland-Altman analysis considering all scenarios and also comparing the standard DFT estimation and the complete proposed solution.

The performance can also be analyzed considering only the moments without RBMs or, at least, with reduced external interference. For identifying these moments we can use the RBM mitigation algorithm and look for the processing windows where no interfering components were captured by the time activation bases $\boldsymbol{H}$. Given that spurious noise or additional frequency components may eventually be identified and filtered out as RBMs, we accepted as "minimal movement windows" the ones in which a maximum of 2 bases were excluded by the algorithm. Figure 5.7 shows the obtained performance considering only these moments. The average 10 bpm accuracy for all measurements was higher than 97%, with the 6 bpm accuracy being higher than 80% in all scenarios. The average RMSE was 4.3 bpm, with the best result close to 4 bpm in prone position. In this case, all scenarios presented very similar performance, both in terms of accuracy and RMSE. The percentage of minimal movement windows in prone position was almost twice the number in supine position. This difference may confirm that the prone position leads to reduced random body movements and this is one of the reasons for the better results in this scenario.

This remaining RMSE is expected and can be explained if we take into consideration the premature conditions of the monitored infants (Supplementary Table 1), where the immaturity of their respiratory system and the diagnosed conditions may lead to irregular breathing patterns and thus hinder estimation. In addition, some transients may not be detected as RBMs due to their specific characteristics, which may not agree with our assumption of strength and sparsity (for instance, hiccups which are periodic, or other continuous movements). Finally, some inaccuracy is also expected from the reference device, as these sensors (please refer to the Methods[1]) suffer from imprecision

[1] In Section 5.2.8

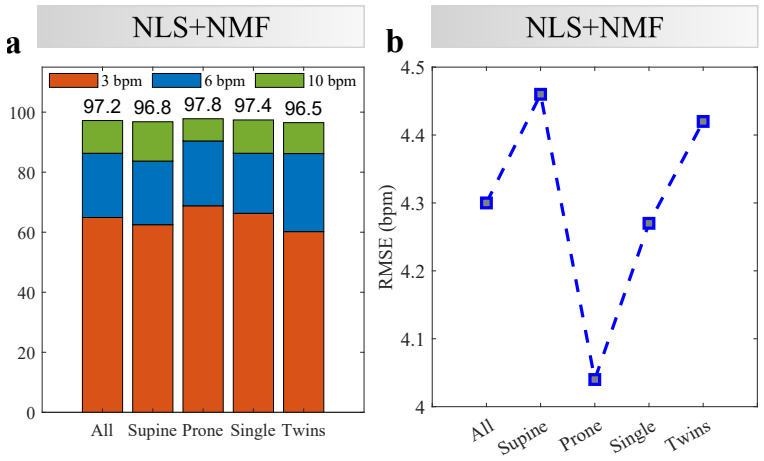

FIGURE 5.7: **Average performance during minimal movement windows. a** Accuracy for different scenarios. **b**, Average RMSE for different scenarios.

and cardiac interference, specially in neonates with higher breathing rates and limited lung aeration [45, 94].

5.2.7 Conclusions

The proposed radar-based solution was able to precisely recover the chest wall motion, allowing clear identification of different breathing patterns. This capability is the first step toward breathing frequency estimation, and early non-invasive diagnosis of neonatal respiratory problems. In addition, most of the time the proposed algorithms provided reliable breathing frequency estimates, effectively reducing the effects of the RBM interference. The best performance was achieved when the infants were in prone position, with the 6 and 10 bpm accuracy reaching almost 80% and 93%, respectively. The overall RMSE was smaller than 7 bpm, with the best result close to 5 bpm in prone position. During minimal movements, the 10 bpm accuracy was higher than 97%, with the 6 bpm accuracy being higher than 80% in all scenarios. The average RMSE was 4.3 bpm, with the best result close to 4 bpm in prone position. These results can be interpreted as a proof-of-principle that the proposed radar-based approach has the potential for contactless breathing monitoring in the NICU. However, more experiments are underway to further reduce the vulnerability to artifacts, e.g. by using optimized algorithms of data processing and redundant technologies.

Finer radar calibration and a more precise setup adjustment would improve raw data quality and reduce ADC saturation. Further improvement of radar's input data can still be achieved by shifting from CW to MIMO and FMCW architectures. This change would allow not only range isolation from external interference, but also to steer the radar's beam (field-of-view) directly to the monitored patient. The motion robustness can still

be improved by tailoring the NMF algorithm according to the specific characteristics of the random body movement interfering signal. One particular case of interest would be the sparse NMF.

Finally, follow-up studies with more mature and healthy children of different ages would allow to identify pathologies, age-specific characteristics or confounding factors, and to adapt the experimental design accordingly. The best average results obtained at prone position point to the necessity of additional investigation on different clinical setups, where the radar could be also positioned under the mattress. Furthermore, with the aim to develop a complete contactless solution, an investigation of the radar capabilities for heart rate monitoring in this challenging environment is necessary as well as moving to real-time processing.

5.2.8 Methods

Notation. We are adopting the following notation: lower case boldface for vectors $\boldsymbol{x}$, and upper case boldface for matrices $\boldsymbol{X}$. The letter j represents the imaginary unit (i.e., $\mathrm{j} = \sqrt{-1}$), with the absolute value and angle operators given by the symbols $|(\cdot)|$ and $\angle(\cdot)$. The transpose, conjugate, and conjugate transpose operators are denoted respectively by the symbols $(\cdot)^{\mathrm{T}}$, $(\cdot)^*$, and $(\cdot)^{\mathrm{H}}$. The sets of N-dimensional vectors of complex and real numbers are represented by $\mathbb{C}^N$ and $\mathbb{R}^N$. The Euclidean norm of the vector $\boldsymbol{x}$ is denoted by $||\boldsymbol{x}||$. The Hadamard product is denoted by $\odot$.

Ethics Statement. The study was designed in accordance to the Declaration of Helsinki, and approved by the regional ethics committee of Saarland (Saarbrücken, Germany), with reference number 276/17. Written informed consent was obtained from the parents prior to the data collection, and all the documentation and collected data were pseudonymized.

Radar system. The CW radar device used in this study is a prototype variant of the IEE's VitaSense® sensor [152], operating in the 24-GHz ISM band, with an illumination area of 76.5° in azimuth, and 35.5° in elevation. At the monitored distances, the low transmitted power leads to energy absorption rates 20 times below that of a cell phone [205]. The ADC sampling rate was 16 Hz, and the data acquisition was controlled by proprietary software on the external computer.

Reference cabled device. Throughout all measurements, the infants were connected to a reference monitor commonly employed in the NICU. In addition, respiration, heart rate and oxygen saturation signals were recorded using the VitaGuard® 3100 device

[206], cable-connected using 3 Kendall® neonatal 4203 electrodes [207]. This device measures the breathing movement through the electrodes attached to the infant's chest (impedance pneumography), and provides the breathing rate with a resolution of 1 bpm, and an update rate of 1 second. The synchronization between reference and estimated frequency values was performed offline, based on the correlation between these signals. After processing an entire measurement (25 minutes), the resulting array with radar estimated frequency values is compared to the longer array with reference values, in a sliding window approach. The synchronization index was selected in order to maximize the correlation between these arrays. This procedure was performed automatically, using a Matlab routine.

CW radar operational principle. The transmitted CW signal can be written as

$$x_{\mathrm{T}}(t) = \sqrt{A_{\mathrm{T}}}\cos(2\pi f_{\mathrm{c}} t + \phi(t)), \tag{5.4}$$

where A_{T} and f_{c} are, respectively, the transmitted signal power and operating frequency, and $\phi(t)$ is the transmitter phase noise (local-oscillator). This signal is phase modulated by the target's motion, and reflected to the radar for processing. The received signal from a target at nominal distance d_0 can be written as

$$x_{\mathrm{R}}(t) = \sqrt{A_{\mathrm{R}}}\cos\left(2\pi f_{\mathrm{c}} t - \frac{4\pi d_0}{\lambda} - \frac{4\pi d(t)}{\lambda}\right), \tag{5.5}$$

with A_{R} being the received power, λ the operating wavelength, and $d(t)$ representing the target motion. After demodulation and analog-to-digital conversion, and assuming correct I/Q imbalance compensation, the baseband I and Q signals can be represented as [92]

$$b_{\mathrm{I}}(t) = \cos\left(\theta_0 + \frac{4\pi d(t)}{\lambda}\right) + B_{\mathrm{I}}, \tag{5.6}$$

$$b_{\mathrm{Q}}(t) = \sin\left(\theta_0 + \frac{4\pi d(t)}{\lambda}\right) + B_{\mathrm{Q}}, \tag{5.7}$$

where $\theta_0 = 4\pi d_0/\lambda$ is the constant phase shift, and B_{I} and B_{Q} are DC offsets.

Under ideal conditions, the AD can be used for precise phase recovery. In this case, the displacement signal is reconstructed as [117]

$$x(t) = \frac{\lambda}{4\pi} \cdot \mathrm{unwrap}\left(\arctan\left[\frac{b_{\mathrm{Q}}(t)}{b_{\mathrm{I}}(t)}\right]\right) = \theta_0 + d(t), \tag{5.8}$$

where the unwrap operation is necessary for removing possible phase discontinuities, caused by the restricted range of the arctangent function (wrapped phases around $(-\pi, \pi]$ are expected when displacements are greater than $\lambda/4$). Before extracting the desired phase information, the DC components (B_{I} and B_{Q}) must be compensated [147]. Given that the ideal chest wall (back-and-forth) movement describes an arc in the I/Q plane, this compensation is usually accomplished using an ellipse fitting algorithm. However, small displacements (small arcs), noise and/or external interference, usually compromise the fitting process, and lead to inaccurate DC compensation. In addition, the unwrap operation is also very sensitive to noise and interference, and may eventually accumulate errors, resulting in large distortions on the recovered displacement signal.

Using the CSD, the displacement signal can be reconstructed as [116]

$$x(t) = b_{\mathrm{I}}(t) + \mathrm{j} \cdot b_{\mathrm{Q}}(t) = \overline{x} + \exp\left\{\mathrm{j}\left(\theta_0 + \frac{4\pi d(t)}{\lambda}\right)\right\}, \tag{5.9}$$

where $\overline{x} = B_{\mathrm{I}} + \mathrm{j}B_{\mathrm{Q}}$ represents the combined DC offset. However, in this case, this DC term does not affect the relevant components of the recovered signal, and, in practice, it can be easily extracted by subtracting the average of the time-domain processing window. Despite additional higher order harmonics, for small displacements (in relation to the operating wavelength), the recovered signal $x(t)$ approximates the true chest wall movement $d(t)$, and the relevant frequency content is preserved. Therefore, besides being more robust to the DC offsets and external interference, the CSD simplifies the demodulation procedure. A detailed description of AD and CSD methods can be found in [117] and [118].

Nonnegative matrix factorization. The magnitude spectrogram $|\boldsymbol{X}| \in \mathbb{R}^{F \times T}$ of the recovered displacement signal is obtained through the STFT of $x(t)$, where F and T are, respectively, the number of frequency and time bins used in the STFT operation. Given that we aim to reconstruct the time version of the RBM-filtered signal, the STFT weighting window must comply with the constant overlap-add property [208].

The NMF is thus applied to the magnitude of $\boldsymbol{X}$, and the factorization can be achieved through an optimization problem given by

$$\begin{aligned} &\underset{\boldsymbol{W},\boldsymbol{H}}{\text{minimize}}\, \mathcal{L}\left(\boldsymbol{X},\, \boldsymbol{W}\boldsymbol{H}\right) \\ &\text{subject to}\, \boldsymbol{W} \succeq 0,\, \boldsymbol{H} \succeq 0, \end{aligned} \tag{5.10}$$

with $\boldsymbol{H} \in \mathbb{R}^{K \times T}$ and $\boldsymbol{W} \in \mathbb{R}^{F \times K}$. The symbol "$\succeq$" denotes entry-wise non-negativeness and $\mathcal{L}(\cdot, \cdot)$ represents a generic similarity metric between $|\boldsymbol{X}|$ and $\boldsymbol{W}\boldsymbol{H}$. The Euclidean

(Frobenius) distance is commonly used and, in doing so, simple gradient descent can be used for minimizing the objective function [197]. The predefined number of basis components K should be selected considering the different frequency components that may be present in the calculated spectrogram, including the breathing frequency and eventual RBM interference. For the long-term monitoring, we have empirically selected $K = 11$.

The identification of the time activation basis corresponding to the RBMs is based on an adaptive amplitude threshold. The breathing pattern is affected by several factors (subject, gender, age, health condition, posture) and efficient interference detection requires an adaptive strategy. The RBM interference can be characterized by its distinct behavior which contrasts with the constant and periodic nature of breathing. Therefore, subsequent to NMF decomposition, we are looking for strong (stronger than average) and sparse (short duration in relation to the processing window) time activation basis $\boldsymbol{h}_i$ in $\boldsymbol{H}$. This can be accomplished simply by comparing the local energy in each time component of $\boldsymbol{h}_i$, with the average energy in $\boldsymbol{H}$ for the current processing window (under regular conditions, that would correspond to the average breathing energy). This average energy acts as the threshold and, by the nature of its computation, it changes for each window and reflects the signal strength therein. Therefore, the threshold will be automatically adjusted for each processing window accordingly. Additionally, the sparsity is verified by checking if the remaining components of that selected basis have negligible amplitude.

The magnitude of the RBM-filtered spectrogram can be reconstructed as

$$|\widehat{\boldsymbol{X}}| = \sum_{i=1}^{K} s_i \boldsymbol{w}_i \boldsymbol{h}_i^{\mathrm{T}}, \tag{5.11}$$

where s_i indicates whether the i^{th} basis corresponds to RBMs or not, i.e. $s_i = 0$ when RBM is present in basis $\boldsymbol{h}_i$, or $s_i = 1$ otherwise. In order to synthesize the time-domain filtered signal $\widehat{x}(t)$, it is first necessary to obtain the phase of the filtered spectrogram. A common practice is to use a Wiener-like filtering approach, which translates into reusing the phase of the original mixed spectrogram $\boldsymbol{X}$ [209]. The inverse STFT is finally applied to $\widehat{\boldsymbol{X}} = |\widehat{\boldsymbol{X}}| \odot \angle \boldsymbol{X}$, replicating the same window configuration (duration, weights and overlap) as in the initial STFT. In this work we are using standard rectangular windows with 3 seconds of duration, 2 seconds of overlap and zero-padding to 256 samples.

The RBM method is applied to every processing window. The method is capable of automatically detecting and removing the RBM interference, based on the adaptive amplitude threshold and the sparsity check. No manual annotation is needed. In the absence of RBMs or other interfering effects, the recovered signal will contain only the constant and periodic chest wall movement, and the resulting time activation bases $\boldsymbol{H}$

will reflect that. In this case, the adaptive amplitude threshold will not identify any candidate basis containing RBMs, and the filtered signal will be approximately the same as in the input of the RBM block.

NLS estimation. The breathing displacement signal $d(t)$ can be modeled as a sum of L_k harmonically related complex sinusoids, having frequencies that are integer multiples of a fundamental frequency $\omega_k > 0$. After sampling for $n \in \{0, \cdots, N-1\}$, such a signal can be written as [199]

$$d(n) = \sum_{k=1}^{K} d_k(n) = \sum_{k=1}^{K} \sum_{l=1}^{L_k} a_{k,l} \mathrm{e}^{\mathrm{j}\omega_k l n}, \tag{5.12}$$

where $a_{k,l} = A_{k,l}\mathrm{e}^{\mathrm{j}\phi_{k,l}}$ is the complex amplitude of the lth harmonic, L_k represents the number of harmonics (the model order), and K refers to the number of components (point scatters).

The NLS estimates are obtained by minimizing the Euclidean norm of the difference between the recovered and filtered displacement signal $\widehat{d}(t)$, and the displacement signal model in (5.12). First, let us consider a single source k, and define $\boldsymbol{d}_k = [\ d_k(0)\ \cdots\ d_k(N-1)\ ]^{\mathrm{T}} \in \mathbb{C}^N$, the vector consisting of N consecutive samples of $d_k(n)$, which can be expressed as

$$\boldsymbol{d}_k = \boldsymbol{Z}_k \boldsymbol{a}_k, \tag{5.13}$$

with $\boldsymbol{a}_k = [\ A_{k,1}\mathrm{e}^{\mathrm{j}\phi_{k,1}}\ ...\ A_{k,L_k}\mathrm{e}^{\mathrm{j}\phi_{k,L_k}}\ ]^{\mathrm{T}}$ being the vector containing the complex amplitudes of the harmonics, and the matrix $\boldsymbol{Z}_k \in \mathbb{C}^{N \times L_k}$ having a Vandermonde structure, being constructed from the L_k complex sinusoidal vectors as

$$\boldsymbol{Z}_k = [\ \boldsymbol{z}(\omega_k)\ \boldsymbol{z}(2\omega_k)\ ...\ \boldsymbol{z}(L_k\omega_k)\ ], \tag{5.14}$$

with $\boldsymbol{z}(\omega) = [\ 1\ \mathrm{e}^{\mathrm{j}\omega}\ ...\ \mathrm{e}^{\mathrm{j}\omega(N-1)}\ ]^{\mathrm{T}}$. Writing $\widehat{d}(t)$ as the vector $\widehat{\boldsymbol{d}} = [\ \widehat{d}(0)\ \cdots\ \widehat{d}(N-1)\ ]^{\mathrm{T}} \in \mathbb{C}^N$, the NLS estimates $\widehat{\omega}_k$ and $\widehat{\boldsymbol{a}}_k$ are finally obtained by solving the problem [202]

$$\underset{\omega_k, \boldsymbol{a}_k}{\text{minimize}}\ ||\widehat{\boldsymbol{d}} - \boldsymbol{Z}_k \boldsymbol{a}_k||^2. \tag{5.15}$$

By first minimizing (5.15) with respect to the complex amplitudes $\boldsymbol{a}_k$ we obtain the estimate $\widehat{\boldsymbol{a}}_k = (\boldsymbol{Z}_k^{\mathrm{H}}\boldsymbol{Z}_k)^{-1}\boldsymbol{Z}_k^{\mathrm{H}}\widehat{\boldsymbol{d}}$, which when plugged into (5.15) leads to [202]

$$\widehat{\omega}_k = \arg\max_{\omega_k} \widehat{\boldsymbol{d}}^{\mathrm{H}} \boldsymbol{Z}_k (\boldsymbol{Z}_k^{\mathrm{H}}\boldsymbol{Z}_k)^{-1} \boldsymbol{Z}_k^{\mathrm{H}} \widehat{\boldsymbol{d}}. \tag{5.16}$$

Assuming $N \gg 1$, then $\boldsymbol{Z}_k^{\mathrm{H}} \boldsymbol{Z}_k \approx N \cdot \boldsymbol{I}_{L_k}$. Thus, considering only a single dominant breathing scatter (i.e. $K = 1$, so that we can drop the index k), we have

$$\widehat{\omega} \approx \arg\max_{\omega} ||\boldsymbol{Z}^{\mathrm{H}} \widehat{\boldsymbol{d}}||^2. \tag{5.17}$$

The matrix product $\boldsymbol{Z}^{\mathrm{H}} \widehat{\boldsymbol{d}}$ can be efficiently implemented using an FFT algorithm and a linear grid search over the candidate frequencies $\left\{0, \frac{2\pi}{N}, \cdots, \frac{2\pi}{N}(N-1)\right\}$. The estimator thus reduces to a summation of the breathing harmonics over the power spectral density of the recovered displacement signal $\widehat{d}(t)$. Usually, a few harmonics may be present in $\widehat{d}(t)$. However, the small motion amplitudes of the monitored patients imply a reduced SNR, where higher-order harmonics will often be masked by noise. Therefore, in this work, we have adopted $L_k = 2$. Additionally, the search interval was limited to ± 5 bpm around the initial time domain estimation.

Data Availability

The original dataset analyzed during the current study is available for download at https://radarmimo.com/.

Code Availability

Matlab reading functions for both radar and reference device are available for download at https://radarmimo.com/. Please refer to the Supplementary File 1 for a brief description of the codes.

Supplementary File 1: Matlab codes

- readRadarRaw.m: simple function for reading radar .csv files with the raw data in I and Q format.
- testReadRadarRaw.m: procedure for test the reading of radar files and plot.

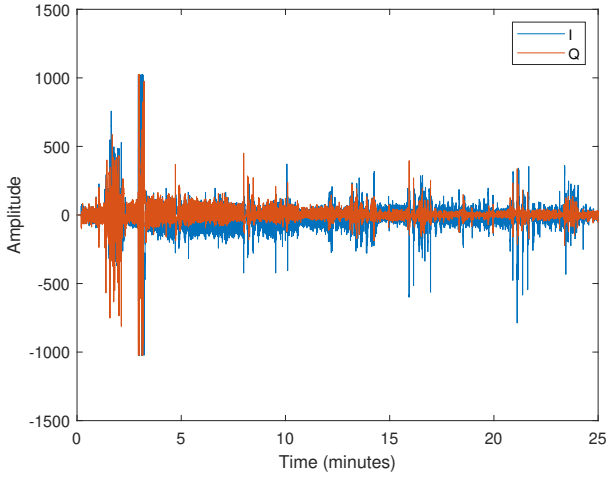

FIGURE 5.8: **Radar raw data in I and Q format.**

- readReferenceData.m: simple function for reading the reference device .edf files, with the raw data and reference frequency values.
- testReadReferenceData.m: procedure for test the reading of reference files and plot.

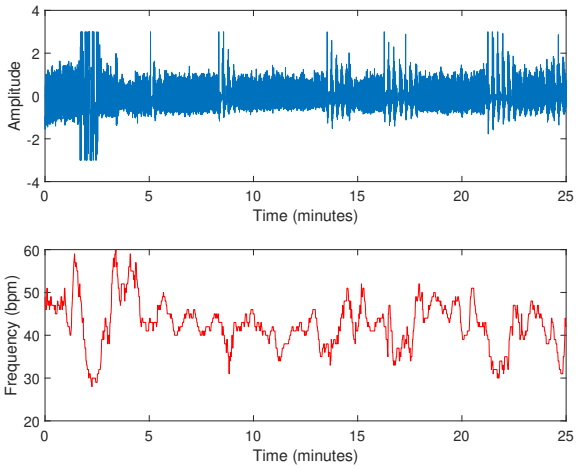

FIGURE 5.9: **Reference cabled device raw data (top) and correspondent frequency values (bottom).**

Supplementary File 2: Patient's information

- Supplementary Table 1: Summary of patient's information.

patient	01	02	03	04	05	06	07	08	09	10	11	12
sex	m	f	m	m	m	m	m	f	m	f	m	m
gestation age [weeks]	28	28	36	32	28	28	34	34	35	26	27	30
gestation weight [g]	1495	1250	2080	1990	850	760	2430	2210	1490	990	1145	1940
gestation length [cm]	40	38	45	46	36	35	48	48	37	34	38	41
age at measurement [days]	63 ± 1	63 ± 1	10 ± 1	9 ± 2	91 ± 1	91 ± 1	14 ± 1	14 ± 1	18 ± 2	50 ± 2	52 ± 1	28 ± 1
body weight at measurement [g]	2650	2618	2165	2165	2165	2165	2165	2165	2165	2165	2165	2165
body length at measurement [cm]	47	47	46	46	-	-	50	50	45	-	45	50
measurements per patient	3	3	3	3	3	3	3	3	3	3	3	3
time per measurement [min]	25	25	25	25	25	25	25	25	25	25	25	25
diagnosis												
respiratory distress syndrome	x	x	-	-	x	x	x	-	-	x	x	-
apnea bradycardia syndrome	x	x	-	x	x	x	x	x	x	x	x	x
bronchopulmonary dysplasia	-	-	-	-	-	-	-	-	-	x	x	-
respiratory adaptive disorder	-	-	-	-	-	-	-	x	x	-	-	x

- Supplementary Fig. 1: Radar distance in each measurement.

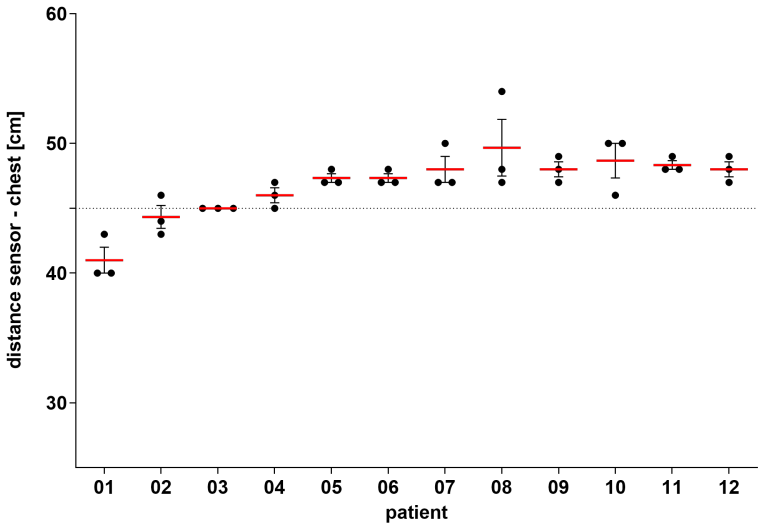

FIGURE 5.10: **Radar distance in each measurement.**

Supplementary File 3: Patient's protocols

- Supplementary Table 2a: patient's protocols (1-3). [1]

measure-ment	co-bedding	position during measurement			lid	interventions	transients
		prone	supine	side			
1.1	yes		x		half-opened	12:34-13:25: nurse at sibling 17:39-18:33: mother at sibling 21:30-22:01: mother at patient	03:17-09:07: hiccups 24:02-25:00: crying
1.2	yes	x			half-opened	06:26-06:49 nurse at patient	04:05-04:26: unsettled 07:00-08:00: unsettled 11:39-12:00: grunting 14:35-15:13: movement 17:57-18:15: movement
1.3	yes		x		half-opened	18:17-19:00: mother at patient	09:12-10:20: movement / yawn 11:50-12:35: movement 14:50-16:30: movement 22:20-24:42: grunting/movement
2.1	yes		x		half-opened	20:00-20:35: nurse at bed	02:48-03:20 sibling unsettled 06:15-07:40 unsettled 08:28-10:50 movement/grunting 11:39-12:00 sibling movement 14:00-14:45: grunting / movement 15:30-15:35: grunting 17:00-18:00: sibling crying 24:00-25:00: yawn
2.2	yes		x		half-opened	16:25-25:00: nurses present in room	02:20-03:25: movement full body 03:25-05:47: movement hand 06:23-07:50: movement / yawn 09:28: pulls cables 10:07-11:50: movement 13:31-14:29: movement hand 18:12-22:35: movement hand
2.3	yes		x		half-opened	05:06-05:30: mother at patient	03:14-04:00: unsettled 07:00-07:30: movement / yawn 09:00-10:00: unsettled 10:48-13:00: unsettled 14:00-16:30: unsettled 18:17-19:05: unsettled 23:04-23:58: unsettled 24:28-25:00: yawn
3.1	no	x			closed	04:40-05:10: nurse at bed	07:00-08:00: movement 10:10-11:05: movement/yawn 16:54-17:26: unsettled 18:38-19:00: movement hand 19:08-19:30: movement/yawn 21:30-22:07: movement/yawn
3.2	yes	x			closed	-	03:50-04:05: sibling movement 08:30-09:15: movement/yawn 09:40-10:40: sibling movement 11:06-11:28: movement/yawn 12:18-12:58: sibling movement 18:13-18:33: movement 19:46-20:07: movement/grunting 21:48-22:05: movement
3.3	yes			x	closed	-	02:47-03:13: movement hand 04:03-04:29: sibling movement 06:47-07:26: unsettled 09:44-10:47: sibling movement 11:07-11:26: movement/yawn 13:24-16:27: sibling movement 20:07-20:39: sibling movement 21:47-22:23: movement 22:45-25:00: sibling movement

[1] The timestamps indicate the moments they happened, starting from the beginning of the measurement (00:00" to 25:00").

- Supplementary Table 2b: patient's protocols (4-6). [1]

measure-ment	co-bedding	position during measurement			lid	interventions	transients
		prone	supine	side			
4.1	no		x		closed		03:00-03:10: movement/yawn 15:10-15:40: unsettled 16:32-16:42: twitch 18:52-19:00: movement 19:43-21:27: movement/grunting 23:28-23:57: movement 24:04-25:00: twitch
4.2	no		x		closed	02:54: nurse walks along the bed 06:52: nurse walks along the bed 07:39-08:13: nurse at the bed 09:31: nurse walks along the bed 13:10: nurse walks along the bed 15:50: nurse walks along the bed 17:28: nurse walks along the bed 20:40: nurse at the bed	03:27-05:03: movement 06:00-06:30: hands movement
4.3	no	x			closed	01:07: nurse walks along the bed 05:13: nurse walks along the bed 06:03: nurse walks along the bed	03:36: grunting 05:35-05:50: yawn / movement 07:34-07:58: movement 09:00-09:30: yawn/movement 09:37-11:43: unsettled 12:21-13:20: movement hand 13:20-14:10: movement 15:20-15:40: movement head 16:25-19:00: movement hand 21:00-24:24: movement
5.1	no		x		closed	20:47-25:00: four nurses present in the room	04:23-06:28: grunting / movement 08:57-11:42: unsettled 13:12-13:36: unsettled 13:55-15:42: movement 19:36-20:25: yawn / movement 24:19-24:29: movement
5.2	no		x		closed	-	00:16-03:54: crying 04:06-04:35: crying 09:26-11:46: movement/crying 15:07-16:26: movement 23:53-24:15: movement
5.3	no	x			closed	-	02:20-04:45: unsetted / grunting 06:58-07:30: grunting / movement 10:20-12:13: unsettled / grunting 14:17-14:50: grunting 15:59-16:20: unsettled / movement 18:33-19:12: grunting/movement 23:35-24:06: grunting/movement
6.1	no		x		closed	12:43-13:22: nurse moves bed 16:58-17:23: nurse at the bed	02:56-04:28: movement/grunting 05:05-05:20: movement 06:31-07:40: grunting / yawn 08:17-10:00: movement 12:25-15:55: movement 18:12-18:58: grunting/movement 21:09-22:25: movement 23:30-24:33: grunting 24:23-25:00 crying
6.2	no	x			closed		05:52-06:35: unsettled 11:13-12:10: grunting / movement 14:10-14:50: grunting / movement 16:42-17:14: grunting 18:59-19:43: unsettled 22:50-23:28: unsettled
6.3	no		x		closed		04:22-05:36: grunting / movement 08:39-08:57: yawn 09:04-09:43: grunting / movement hands 10:32-11:30: movement 11:45-12:16: unsettled 14:11-16:03: grunting / movement 18:11-19:21: movement 21:07-22:23: movement

[1] The timestamps indicate the moments they happened, starting from the beginning of the measurement (00:00" to 25:00").

- Supplementary Table 2c: patient's protocols (7-9). [1]

measure-ment	co-bedding	position during measurement			lid	interventions	transients
		prone	supine	side			
7.1	no		x		closed	-	05:10-05:35: unsettled 11:06-12:45: movement 17:04-17:34: unsettled
7.2	yes		x		closed	-	02:07-02:29: unsettled 02:44-03:54: sibling unsettled 08:19-10:01: yawn / movement 11:22-11:47: sibling unsettled 14:18-14:45: sibling unsettled 15:09-15:17: movement 16:27-16:42: unsettled 18:55-19:08: sibling unsettled 19:50-20:18: unsettled
7.3	yes	x			closed	02:50-03:15: fasten O2-Sensor	01:38-02:14: unsettled
8.1	no		x		closed	-	all time hands movement 05:41-06:39: movement 08:19-09:01: yawn / movement 13:02-13:17: yawn / movement 16:00-16:48: yawn / movement 17:38-18:00: movement 19:21-20:21: yawn / movement 22:18-22:35: yawn / movement
8.2	yes		x		closed	-	02:53-03:33: grunting / movement 05:14-06:04: grunting / movement 12:18-13:08: grunting / movement 16:15-17:02: movement 19:15-20:17: unsettled / movement
8.3	yes	x			closed	06:00-06:41: nurse at sibling	02:34-02:53: grunting / movement 06:20-06:47: unsettled 10:34-11:08: grunting
9.1	no		x		closed	-	11:12-11:28: yawn 12:56-13:11: grunting 15:13-15:42: unsettled / movement 19:32-19:56: grunting 20:00-20:12: movement
9.2	no		x		closed	-	01:05-02:38: movement / grunting 04:11-04:18: grunting 04:58-06:49: movement 11:00-11:11: movement 12:04-12:51: movement 15:07-15:37: movement 19:49-20:51: movement 22:13-22:27: grunting 23:40-25:00: movement / grunting
9.3	no		x		closed	-	01:00-01:59: grunting / movement 03:49-03:57: grunting / movement 08:55-09:38: grunting / movement 10:27-10:59: grunting / movement 15:01-16:03: grunting / movement 17:45-18:02: grunting / movement 18:52-19:11: grunting / movement 23:23-24:19: grunting / movement

[1] The timestamps indicate the moments they happened, starting from the beginning of the measurement (00:00" to 25:00").

- Supplementary Table 2d: patient's protocols (10-12). [1]

measure-ment	co-bedding	position during measurement			lid	interventions	transients
		prone	supine	side			
10.1	no		x		closed	-	01:13-01:37: movement 03:24-04:25: yawn / grunting / movement 06:43-07:37: movement / grunting 10:58-11:28: grunting / movement 15:18-16:27: yawn / movement 18:30-19:27: movement
10.2	no	x			closed	-	05:49-06:37: grunting / movement 09:10-09:23: movement 11:07-11:46: movement 12:45-13:09: movement / grunting 14:33-15:13: grunting 20:04-20:10: yawn / movement 22:58-23:04: yawn
10.3	no	x			closed	-	04:01-05:13: movement 09:28-09:45: movement / grunting 13:18-13:56: grunting / movement 17:17-18:14: grunting / movement 21:07-22:14: grunting / movement
11.1	no		x		closed	-	02:04-03:21: grunting / movement 05:16-05:33: yawn / movement 09:29-10:05: yawn / movement 12:47-14:20: grunting / yawn / movement 18:31-18:46: grunting / movement 18:47-19:29: grunting 20:59-21:33: movement 23:52-24:23: grunting / movement
11.2	no		x		closed		02:24-03:46: yawn / movement 06:28-06:37: grunting 07:11-07:56: movement 09:13-09:41: movement 11:27-11:52: yawn / movement 15:24-16:58: movement / grunting 21:39-22:31: movement / grunting
11.3	no		x		closed	09:48-10:35: nurse walks along the bed	02:30-02:52: movement 05:55-06:12: grunting / movement 20:47-21:05: grunting / movement 23:15-24:31: movement
12.1	no	x			closed	05:00: nurse walks along the bed 06:22: nurse walks along the bed	02:36-03:29: movement / yawn 09:02-09:51: movement / grunting 09:58-19:44: hiccups 11:21-12:10: movement 15:50-16:45: yawn / movement 17:24-17:37: movement 18:35-19:29: movement 20:15-20:43: movement 22:00-22:26: yawn / movement
12.2	no	x			closed	-	01:38-02:26: grunting 07:32-08:02: grunting / movement 09:34-09:40: movement 10:37-11:05: yawn / movement 15:33-16:01: grunting 17:03-17:16: grunting 18:43-18:53: yawn 20:30-20:42: grunting 23:36-25:00: hiccups
12.3	no		x		closed	01:12-01:17: mother walks along the bed 10:47-11:16: nurse at bed	01:21-02:31: movement 04:55-05:02: yawn / movement 07:46-09:02: movement / yawn 09:15-09:24: movement 10:40-11:18: movement 13:08-13:37: movement 15:33-16:04: movement / grunting 16:11-16:53: yawn / movement 16:58-17:24: crying 19:07-20:01: movement

[1] The timestamps indicate the moments they happened, starting from the beginning of the measurement (00:00" to 25:00").

Supplementary File 4: Bland-Altman's analysis

Figure 5.11a shows the Bland-Altman plot considering all measurements for the complete solution. The mean bias was 0.262, with 95% upper and lower limits of agreement (LOAs) of 12.01 bpm and -11.48 bpm, respectively. Figure 5.11b shows the Bland-Altman plot considering all valid estimates for a single measurement (7.3), in prone position (please refer to the Supplementary File 3). It also compares the performance using standard DFT estimation and the complete proposed solution. The mean bias was -0.296, with LOAs of 7.64 bpm and -8.24 bpm, respectively.

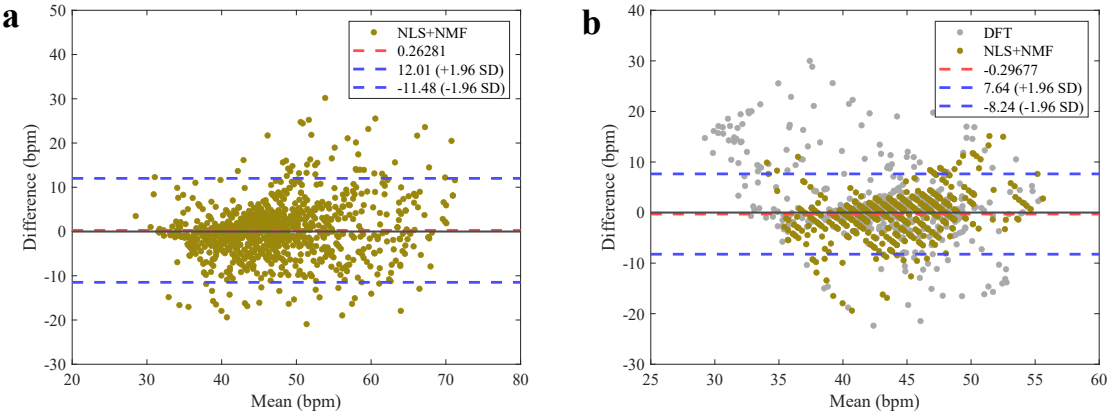

FIGURE 5.11: **Bland-Altman analysis. a,** All measurements for the complete solution. **b,** Single measurement, comparing the standard DFT estimation and the proposed solution.

Chapter 6

Frequency Estimation

6.1 Preamble

In this chapter, we will present our last manuscript. We now focus on the frequency estimation block, in which the aim is to finally estimate the breathing rate and/or the heart rate. It connects to the previous chapter by assuming that most of the interfering components (including stronger RBMs) were already filtered, and the resulting signal contains only the desired chest wall displacement due to breathing or heartbeat.

As discussed in Chapter 3, higher-order harmonics from the breathing signal may interfere with heart rate estimation and should be considered in the estimator design. In addition, residual interfering movements may also still be present, especially if these have smaller amplitudes and continuous nature. These characteristics make them more difficult to identify and extract before estimation. Therefore, the estimator should provide additional robustness to deal with them.

In the presented manuscript, we proposed a novel signal processing framework to overcome these challenges. In this case, validation was performed with real data collected while imitating common working conditions in an office environment.

6.2 Manuscript: Adaptive nonlinear least squares framework for contactless vital sign monitoring

Gabriel Beltrão[1], Wallace A. Martins[1], Bhavani Shankar M.R.[1], Mohammad Alaee-Kerahroodi[1], Udo Schroeder[2], Dimitri Tatarinov[2],

[1] SnT - Interdisciplinary Centre for Security, Reliability and Trust, University of Luxembourg
[2] IEE S/A, Luxembourg

Published in: *IEEE Transactions on Microwave Theory and Techniques (Early Access)*
DOI: 10.1109/TMTT.2022.3222384

This section is a copy of the paper referenced above.

Abstract

The respiratory and heart rates are critical physiological parameters and conventional contact-based monitoring techniques may cause discomfort and epidermal damage, being therefore inadequate for long-term monitoring. Despite recent advances, accurate contactless vital sign monitoring is still challenging in practical scenarios, especially in relation to heart rate estimation. In this work, we propose a comprehensive framework for vital sign processing in frequency-modulated continuous-wave radar systems and evaluate its performance with real data imitating common working conditions in an office environment. First, to improve the signal-to-noise ratio before estimation, we propose a novel slow-time phase correlation processing, which allows early integration of the vital sign energy at nearby range bins. Subsequently, we present an adaptive nonlinear least-squares framework that explores the harmonic structure existing in the recovered displacement signal. An additional Kalman filter stage is designed to select among multiple estimates from different search regions, thus conferring adaptivity and robustness against harmonic interference and noise. This approach largely provides estimates within the predefined error intervals, being capable of tracking the true breathing and heart rate values even during continuous small body movements. The final accuracy and root-mean-square error values have shown enhanced estimation, outperforming conventional spectral estimation and other recently proposed methods in almost all scenarios.

6.2.1 Introduction

People are living longer. Between 2015 and 2050, the proportion of the world's population over 60 years will nearly double, and outnumber children under the age of 5 [1]. Due to the rapid aging of the population worldwide, a lot of effort is being dedicated to providing efficient and more accessible healthcare solutions.

In this context, continuous monitoring of vital signs plays a crucial role in the early detection of conditions that affect the well-being of a patient. The respiratory and

heart rates are critical physiological parameters and by continuously monitoring this information it is possible to detect drowsiness [2], sleep apnea [3] and even depression [4]. However, conventional monitoring devices, usually connected by cables, besides restricting mobility, may cause discomfort and epidermal damage, being therefore inadequate for long-term monitoring.

On the other hand, contactless radar-based vital sign monitoring provides several advantages over standard devices. Unlike cameras, radar signals can penetrate through different materials and are not affected by skin pigmentation or ambient light levels [88]. Unlike wearable sensors, radar systems do not require users to wear or carry any additional equipment. In addition, radar devices preserve privacy [13], and can be low-power and low-cost. These inherent characteristics have drawn the attention of the research community, and a variety of radar types are now being used to address different healthcare applications, including sleep monitoring [89], life detection and rescue [90], assisted living [91], diagnosis [92], and many others.

CW radars have been extensively employed for vital sign monitoring [54, 78, 111]. These devices have the advantages of low transmitted power, simple hardware structure, and high sensitivity, which explain their widespread use across various areas. Within this group, unmodulated CW systems have the simplest architecture, but with the limitation that no distance information in relation to the target is acquired. In addition, other moving objects may interfere with the CW radar signal, making it more difficult to isolate the target information from interfering objects [13]. For being able to estimate the target distance (range), typical approaches use UWB and FMCW radars. Recently, the application of millimeter-wave FMCW radars to short-range vital sign monitoring has been widely investigated [147, 210, 211]. Such radars benefit from high range resolution and Doppler sensitivity, yet with simple architecture, that allows using relatively simple circuits and low-cost ADCs [113]. Furthermore, the mass production from the automotive industry has resulted in the large availability of inexpensive radar modules with increased capabilities and functionalities [157].

Despite recent advances, accurate vital sign monitoring is still challenging in practical scenarios, especially in relation to heart rate estimation. Radar-based vital sign processing relies on the phase analysis of the back-scattered signal, corresponding to the chest wall periodic displacement due to the breathing and heartbeat mechanisms. The recovered displacement signal is usually composed not only of the breathing and heartbeat fundamental frequencies but also of their associated harmonics. The challenge stems from the fact that the tiny heartbeat-induced motion is typically several times smaller than the one originated from breathing. Therefore, the heartbeat signal can be easily buried in the background noise or masked by higher-order harmonics of the breathing signal. This

harmonic interference in the heartbeat signal has been extensively reported as one of the main issues in radar-based vital sign monitoring [112, 212–214] and, as discussed in [122], depending on the SIR, and the specific combination of fundamental breathing/heartbeat frequencies, most techniques fail to provide robust heart rate estimation. Furthermore, additional frequency components and intermodulation products may also be present in the recovered signal, originated from different sources including radar non-linearities, phase-demodulation issues [117], and random body movements from the monitored subject [124]. These interfering elements tend to be dominant in the neighborhood of the heartbeat fundamental frequency, often preventing detection and hindering estimation.

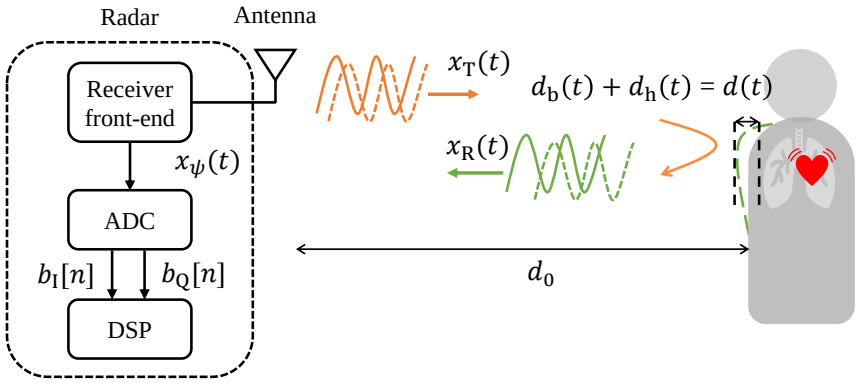

FIGURE 6.1: Contactless radar-based vital sign monitoring. Basic operational principle. For simplicity, a single ADC channel is being shown.

In this paper, we propose a comprehensive framework for vital sign processing based on a millimeter-wave FMCW radar system, and we evaluate its performance using real data collected while imitating typical working conditions in an office environment. First, to improve the SNR before estimation, we propose a novel slow-time phase correlation processing, which allows for the integration of displacement signals at nearby range bins, while still preserving its relevant frequency content. Early integration of these correlated signals allows useful exploitation of the vital sign energy, without the need of processing each range bin independently, as suggested in [132]. Subsequently, we present an adaptive nonlinear least squares (ANLS) framework that explores the harmonic structure existing in the recovered displacement signal. For estimating the breathing rate, we simplify the NLS algorithm recently proposed in [155, 159] and adaptively adjust the search region over the NLS objective function according to previous estimates from adjacent processing windows. For the heart rate estimation, we extend the basic NLS approach and, to avoid the harmonic interference from breathing, we explore the original idea in [99] by generating multiple heart rate estimates based on the heartbeat's own harmonics. However, it is impossible to know which of these estimates are reliable and, to overcome this, we designed an additional Kalman filter stage that uses the gating process (based on its own prediction) to select the best heart rate estimate, thus avoiding low-SNR,

ambiguous or harmonic-interfered candidates. Due to the efficient NLS implementation, based on the fast Fourier transform (FFT), the proposed method can overcome the SNR limitations reported in [99], without significantly increasing the computational burden.

The remainder of this paper is organized as follows. In Section 6.2.2, we introduce the basic operational principle and system modeling for contactless radar-based vital sign monitoring using FMCW radars. The signal processing framework is presented in Section 6.2.3, whereas in Section 6.2.4 we describe our proposal for robust and accurate breathing and heartbeat frequency estimation. Finally, Section 6.2.5 presents some experimental results and, in Section 6.2.6, the conclusions are drawn.

Notation

Throughout this paper, we are adopting the following notation: lower case boldface for vectors $\boldsymbol{x}$ and upper case boldface for matrices $\boldsymbol{X}$. The letter j represents the imaginary unit (i.e., $\mathrm{j} = \sqrt{-1}$), with the absolute value and angle operators given by the symbols $|(\cdot)|$ and $\angle(\cdot)$. The transpose, conjugate, and conjugate transpose operators are denoted respectively by the symbols $(\cdot)^{\mathrm{T}}$, $(\cdot)^*$, and $(\cdot)^{\mathrm{H}}$. The sets of N-dimensional vectors of complex and real numbers are represented by $\mathbb{C}^N$ and $\mathbb{R}^N$. The Euclidean norm of the vector $\boldsymbol{x}$ is denoted by $||\boldsymbol{x}||$. The identity matrix, with size determined from the context, is denoted by $\boldsymbol{I}$. For any complex number x we use $\Re$ and $\Im$ to denote, respectively, the real and the imaginary parts of x. We are using the acronym "bpm" alternatively as breaths per minute (breathing rate) or beats per minute (heart rate). The meaning will be clear from the context.

6.2.2 System Modeling

Fig. 6.1 shows the basic operational principle of contactless radar-based vital sign monitoring. The transmitted FMCW signal can be written as

$$x_{\mathrm{T}}(t) = \sqrt{A_{\mathrm{T}}}\cos(2\pi f_{\mathrm{c}} t + \pi \frac{B}{T_{\mathrm{p}}} t^2 + \phi(t)), \tag{6.1}$$

where A_{T} is the transmitted power, f_{c} is the operating frequency (initial frequency of the chirp), B is the pulse bandwidth, T_{p} the pulse duration and $\phi(t)$ is the transmitter's phase noise (local oscillator). When we breath, or when the heart beats, the subtle chest wall motion modulates the FMCW signal, which is reflected with additional phase information related to this movement. Ideally, the radar receives a scaled and shifted

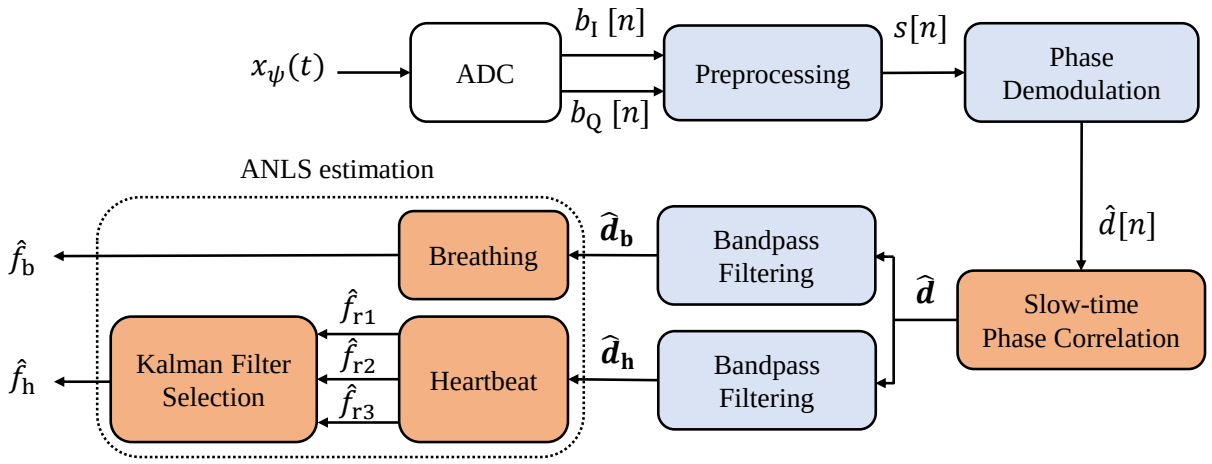

FIGURE 6.2: Block diagram of the proposed signal processing chain.

version of the transmitted signal given by [157]

$$x_\mathrm{R}(t) = \alpha\sqrt{A_\mathrm{T}}\cos\left(2\pi f_\mathrm{c}(t-t_\mathrm{d}) + \pi\frac{B}{T_\mathrm{p}}(t-t_\mathrm{d})^2 + \phi(t-t_\mathrm{d})\right), \tag{6.2}$$

where α represents an attenuation coefficient and $t_\mathrm{d} = 2r(t)/c$ is the range-dependent time delay from a given object at radial range $r(t)$, with c being the speed of light. The received signal is mixed with a replica of the transmitted signal and, after quadrature demodulation, it can be approximated as

$$x_\psi(t) = A_\psi \mathrm{e}^{\mathrm{j}(2\pi f_\psi t + \Delta\theta(t) + \Delta\phi(t))}, \tag{6.3}$$

which represents the beat signal, where A_ψ is the beat signal amplitude, f_ψ the beat frequency and

$$\Delta\theta(t) = 2\pi f_\mathrm{c} t_\mathrm{d} + \pi\frac{B}{T_\mathrm{p}}t_\mathrm{d}^2, \tag{6.4}$$

is the time-varying phase relative to the movement of object. The amplitude terms in (6.2) and (6.3) may vary slightly according to the chest vibration. However, as we are interested in the phase of the slow-time signal, this small variation has no implications and it is often neglected in literature [104, 117, 157]. In addition, due to the range-correlation effect [215], the residual phase noise $\Delta\phi(t)$ in (6.3) is usually neglected for short-range applications. Furthermore, the term $\pi\frac{B}{T_\mathrm{p}}t_\mathrm{d}^2$ in (6.4) can also be discarded as it is negligibly small in practical scenarios [157]. Finally, for an object at nominal range d_0 we have

$$\Delta\theta(t) = \frac{4\pi r(t)}{\lambda_\mathrm{c}} = \frac{4\pi d_0}{\lambda_\mathrm{c}} + \frac{4\pi d(t)}{\lambda_\mathrm{c}}, \tag{6.5}$$

where $\lambda_c = 1/f_c$ is the operating wavelength and, ideally, $d(t)$ would correspond exclusively to the chest wall movement, which is assumed to be the superposition of those induced by breathing and heartbeat. In this case, we can finally write

$$\Delta\theta(t) = \frac{4\pi(d_0 + d_b(t) + d_h(t))}{\lambda_c}, \tag{6.6}$$

with $d_b(t)$ and $d_h(t)$ being the displacements due to breathing and heartbeat, respectively. These movements involve multiple patterns of motion, not only from the chest wall surface but also from the belly, shoulders, and back [96, 97]. Different models have already been proposed for representing these signals, from simple sinusoidal approximations [98, 99] to more complicated patterns as described in [28, 102]. Perfect recovery of the chest wall displacement $d(t)$ would allow precise estimation of breathing and heartbeat frequencies by analyzing the periodicity of the signal. However, in practical applications, besides unavoidable hardware imperfections, the received radar signal is usually mixed with additional reflections from the external environment, arising not only from different body movements of the monitored subject but also from every object in the radar's field-of-view. These interfering signals are usually much stronger than those induced by the chest wall millimeter displacement, and this makes accurate recovery and subsequent estimation of the breathing and heartbeat frequencies a challenging task.

6.2.3 Vital Sign Processing

Figure 6.2 shows the signal processing block diagram of the proposed solution for contactless vital sign monitoring. For providing sufficient SNR, while still preserving the update rate, this processing is commonly performed using overlapped sliding windows. This strategy leaves sufficient time to acquire several breathing/heartbeat cycles, revealing (and enhancing) the periodicity of the movement. Hence, the obtained frequency value from each processing window corresponds to an average over the window duration. In addition, the frequency resolution is also improved. In order to provide new estimates every one or two seconds, large overlaps are usually employed.

The preprocessing block receives the baseband radar signals as in-phase and quadrature samples ($b_I[n]$ and $b_Q[n]$) from the ADCs. In order to extract the slow-time signal from the monitored subject at a specific range and angle position, we use a two-dimensional DFT over the radar data cube, across the range and angle dimensions. Given our specific conditions of monitoring, the detector can be implemented by simply looking for the slow-time signal at the range/angle bin with greater energy.

The phase demodulation is essentially the process where the complex samples of the slow-time signal will be combined with the aim to recover the displacement signal

containing the phase information relative to the chest wall movement over time. Several techniques have been already proposed for that, including the CSD [116, 144, 164] and the linear demodulation [4, 93, 165]. As discussed in [122, 216, 217], these methods suffer from intermodulation products and harmonic interference when applied at higher operating frequencies. To avoid these issues, and enable precise phase recovery, the AD [92, 117, 160] is being used in this work. The recovered displacement signal can thus be obtained as

$$\widehat{d}[n] = \frac{\lambda_c}{4\pi} \cdot \text{unwrap}\left(\arctan\left[\frac{\Im(s[n])}{\Re(s[n])} \right] \right), \tag{6.7}$$

where $s[n]$ represents the samples of the complex slow-time signal at the target range bin. The unwrap operation is necessary for removing possible phase discontinuities caused by the bounded image of the arctangent function. Due to the high sensitivity of mm-wave devices, wrapped phases around $[-\pi, \pi]$ are expected when actual displacements are larger than $\lambda_c/4$.

Prior to the AD, possible DC offsets must be compensated and, for this, we use the Levenberg–Marquardt (LM) algorithm, which provides a maximum likelihood estimate for this problem [218]. For removing any residual DC values, and possible high-frequency noise components, the recovered displacement signal is filtered using a bandpass Kaiser window ($\beta = 6.5$), from 0.1 Hz to 3 Hz ($6 - 180$ breaths/minute) for the breathing, and 0.5 Hz to 5 Hz ($30 - 300$ beats/minute) for the heartbeat. This corresponds to the physiological range of fundamental frequencies, including a few possible harmonics. The bandpass filtered signals $\widehat{\boldsymbol{d}}_b$ and $\widehat{\boldsymbol{d}}_h$ will ideally be a good approximation of the true chest wall motion and can finally be used for frequency estimation. The estimation process is responsible for detecting the breathing/heartbeat cycles and calculating their period, or alternatively, for directly estimating the dominant frequency in which they occur, i.e. the breathing and heart rates.

Slow-time Phase Correlation

The larger bandwidth of mm-wave devices yields a much higher range resolution compared to other radar systems operating at lower frequencies. For instance, if operating at 77 GHz with 4 GHz of bandwidth, the range resolution is around 4 cm. This improved resolution increases the ability not only to resolve closely spaced objects but also to filter-out nearby interference. However, in these conditions, the human body is an extended target and its energy may spread across a few adjacent range bins. Given that belly and back may also be involved in the respiration/heartbeat movement, vital sign information may eventually be detected in these additional range bins.

To exploit this and improve the SNR before estimation, we propose a novel slow-time phase correlation processing, which allows for the integration of the vital sign energy of nearby range bins, while still preserving its relevant frequency content. For achieving this, we first need to look into the correlation between displacement signals at adjacent range bins. By stacking the phase demodulated samples in the current processing window, we can define $\widehat{\boldsymbol{d}}_{\mathrm{d}}$ and $\widehat{\boldsymbol{d}}_{\mathrm{i}}$ as the vectors with the recovered displacement signals at the detected, and the i^{th} adjacent range bin, respectively. We can then calculate the Pearson correlation coefficient, given by

$$\rho(\widehat{\boldsymbol{d}}_{\mathrm{d}}, \widehat{\boldsymbol{d}}_{\mathrm{i}}) = \frac{\mathrm{cov}(\widehat{\boldsymbol{d}}_{\mathrm{d}}, \widehat{\boldsymbol{d}}_{\mathrm{i}})}{\sigma_{\widehat{\boldsymbol{d}}_{\mathrm{d}}} \sigma_{\widehat{\boldsymbol{d}}_{\mathrm{i}}}}, \tag{6.8}$$

where $\mathrm{cov}(\boldsymbol{d}_{\mathrm{d}}, \boldsymbol{d}_{\mathrm{i}})$ represents the covariance between these vectors, with $\sigma_{\boldsymbol{d}_{\mathrm{d}}}$ and $\sigma_{\boldsymbol{d}_{\mathrm{i}}}$ the corresponding standard deviations. If the correlation coefficient exceeds a predetermined threshold, these displacement signals can be summed up and the SNR will improve accordingly. This allows useful exploitation of the energy in nearby range bins, without the need of processing each one of them independently, as suggested in [132]. We can therefore improve estimation performance with no additional cost in terms of computational burden.

Fig. 6.3 shows the effect of the slow-time phase correlation processing. The recovered displacement signals at the detected and its four adjacent are depicted in Fig. 6.3a, with the corresponding calculated values for the correlation coefficient. We empirically set up a threshold value of 0.8 which, in this example, allowed the integration of 3 additional range bins. Fig. 6.3b shows the original phase-demodulated signal (at the detected range bin) and the enhanced signal after processing, where it can be seen how the displacement amplitude increased. In addition, the periodicity remains the same, as confirmed by looking into the spectrum in Fig. 6.3c, where it is clear that the main frequency content is preserved. The peaks corresponding to breathing and heartbeat (inset figure) have increased, and their frequencies match the true values (black dashed lines) associated with this processing window. For calculating the SNR improvement, we compared the SNR at the spectral peak location in the original (detected) displacement, to the one in the enhanced signal. In this example, the obtained improvements were 3.68 dB and 5.45 dB for the breathing and heartbeat signals, respectively. The SNR values were calculated according to [219].

6.2.4 Adaptive NLS Estimation

Due to the inherent periodic nature of breathing and heartbeat, any function representing these movements can eventually be decomposed into Fourier series containing the

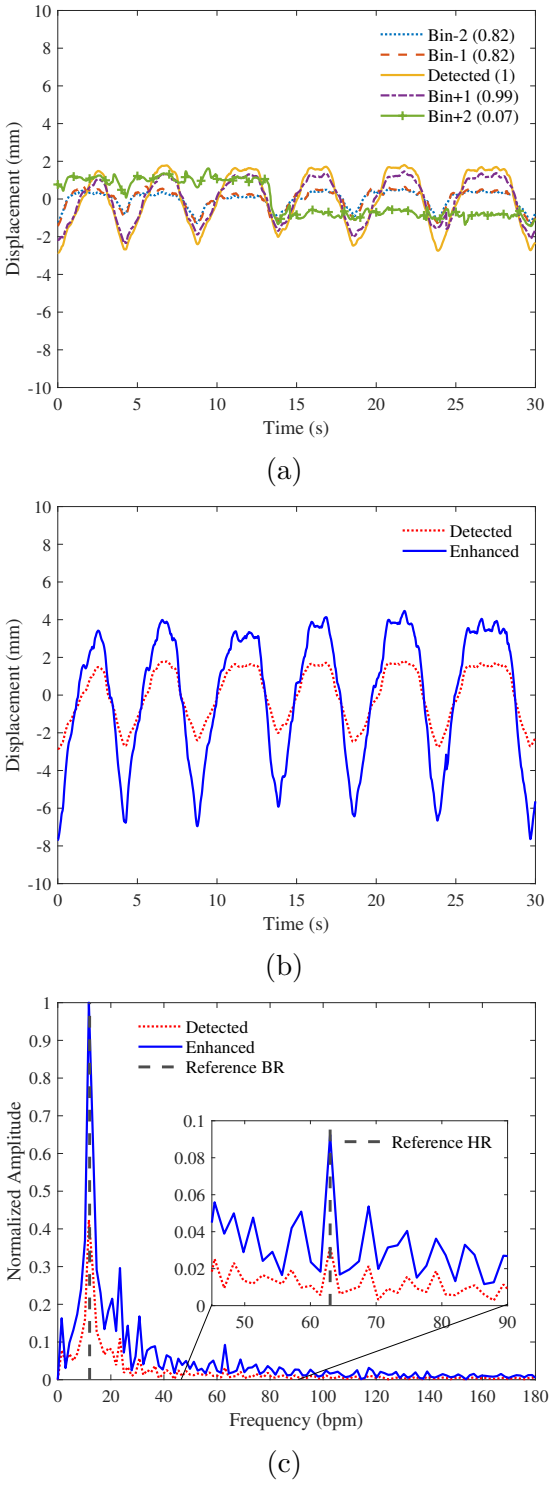

FIGURE 6.3: Slow-time phase correlation processing. (a) Phase-demodulated displacement signals of adjacent range bins. (b) Original phase-demodulated signal (at the detected range bin) and enhanced signal after processing. (c) The spectrum of original and enhanced signals. The inset figure shows a zoom over the heartbeat frequency region. The dashed lines represent the true breathing and heartbeat rates associated with this processing window.

fundamental frequencies and its associated harmonics. Hence, the displacement signal can be modeled as a sum of harmonically related complex sinusoids, having frequencies that are integer multiples of the fundamental breathing/heartbeat frequency. To exploit this harmonic structure, in this section we will use the simple NLS approach recently proposed for breathing rate estimation in [155, 159], and extend it for the heart rate estimation. For doing this, we need to take into consideration the different frequency ranges of these signals, and particularly pay attention to the interference of breathing harmonics in the heartbeat signal.

Basic NLS Framework

The chest wall displacement signal $d(t)$ can thus be modeled as a superposition of K sources with L_k harmonically related complex sinusoids for the k^{th} source, whose frequencies that are integer multiples of the fundamental frequency $\omega_k > 0$. The fundamental frequencies are related to the physiological frequencies f_k (in Hertz) as $\omega_k = 2\pi \frac{f_k}{f_s}$, where f_s is the slow-time sampling frequency which is determined by the time between transmitted frames. In addition, $f_k = 1/\tau_k$ where τ_k is the breathing/heartbeat period. After sampling for $n \in \{0, \cdots, N-1\}$, the model for the chest wall displacement signal can be written as [199]

$$d[n] = \sum_{k=1}^{K} d_k[n] = \sum_{k=1}^{K} \sum_{l=1}^{L_k} a_{k,l} \mathrm{e}^{\mathrm{j}\omega_k l n}, \tag{6.9}$$

where $a_{k,l} = A_{k,l}\mathrm{e}^{\mathrm{j}\phi_{k,l}}$ is the complex amplitude of the l^{th} harmonic.

Now, let us consider a single source k, and define $\boldsymbol{d}_k = [\, d_k[0] \ \cdots \ d_k[N-1] \,]^{\mathrm{T}} \in \mathbb{C}^N$, the vector consisting of N consecutive samples of $d_k[n]$, which can be expressed as

$$\boldsymbol{d}_k = \boldsymbol{Z}_k \boldsymbol{a}_k, \tag{6.10}$$

with $\boldsymbol{a}_k = [\, A_{k,1}\mathrm{e}^{\mathrm{j}\phi_{k,1}} \ \cdots \ A_{k,L_k}\mathrm{e}^{\mathrm{j}\phi_{k,L_k}} \,]^{\mathrm{T}}$ being the vector containing the complex amplitudes of the harmonics, and the matrix $\boldsymbol{Z}_k \in \mathbb{C}^{N \times L_k}$ having a Vandermonde structure, being constructed from the L_k complex sinusoidal vectors as

$$\boldsymbol{Z}_k = [\, \boldsymbol{z}(\omega_k) \ \boldsymbol{z}(2\omega_k) \ \cdots \ \boldsymbol{z}(L_k\omega_k) \,], \tag{6.11}$$

with $\boldsymbol{z}(\omega) = [\, 1 \ \mathrm{e}^{\mathrm{j}\omega} \ \cdots \ \mathrm{e}^{\mathrm{j}\omega(N-1)} \,]^{\mathrm{T}}$. Using these definitions, the signal model in (6.9) can be rewritten as

$$\boldsymbol{d} = \sum_{k=1}^{K} \boldsymbol{Z}_k \boldsymbol{a}_k. \tag{6.12}$$

To obtain the NLS estimates, we look for the set of fundamental frequencies that minimize the difference between the recovered displacement signal $\widehat{\boldsymbol{d}}$ and the signal model in (6.12). In this way, the NLS optimization problem can be expressed as

$$\{\widehat{\omega}_k\} = \arg \min_{\{\boldsymbol{a}_k\},\{\omega_k\}} \left|\left|\widehat{\boldsymbol{d}} - \sum_{k=1}^{K} \boldsymbol{Z}_k \boldsymbol{a}_k\right|\right|_2^2. \tag{6.13}$$

Assuming that $N \gg 1$, and that all frequencies in $\{\boldsymbol{Z}_k\}$ are distinct and well separated, the sources can be treated independently and (6.13) can be approximated by finding the fundamental frequency of each one of them, i.e.,

$$\widehat{\omega}_k = \arg \min_{\boldsymbol{a}_k,\omega_k} \left|\left|\widehat{\boldsymbol{d}} - \boldsymbol{Z}_k \boldsymbol{a}_k\right|\right|_2^2. \tag{6.14}$$

These problems are equivalent when the matrices $\{\boldsymbol{Z}_k\}$ are orthogonal, which is true asymptotically in N, as long as no harmonics overlap [199]. Minimizing (6.14) with respect to the complex amplitudes $\boldsymbol{a}_k$ gives amplitude estimates

$$\widehat{\boldsymbol{a}}_k = (\boldsymbol{Z}_k^{\mathrm{H}} \boldsymbol{Z}_k)^{-1} \boldsymbol{Z}_k^{\mathrm{H}} \widehat{\boldsymbol{d}}, \tag{6.15}$$

which when inserted in (6.14) yields

$$\widehat{\omega}_k = \arg \max_{\omega_k} \widehat{\boldsymbol{d}}^{\mathrm{H}} \boldsymbol{Z}_k (\boldsymbol{Z}_k^{\mathrm{H}} \boldsymbol{Z}_k)^{-1} \boldsymbol{Z}_k^{\mathrm{H}} \widehat{\boldsymbol{d}}. \tag{6.16}$$

By the assumption that $N \gg 1$, we have $\boldsymbol{Z}_k^{\mathrm{H}} \boldsymbol{Z}_k \approx N \cdot \boldsymbol{I}_{L_k}$ and thus

$$\begin{aligned} \widehat{\omega}_k &\approx \arg \max_{\omega_k} \widehat{\boldsymbol{d}}^{\mathrm{H}} \boldsymbol{Z}_k \boldsymbol{Z}_k^{\mathrm{H}} \widehat{\boldsymbol{d}} \\ &\approx \arg \max_{\omega_k} \left|\left|\boldsymbol{Z}_k^{\mathrm{H}} \widehat{\boldsymbol{d}}\right|\right|_2^2. \end{aligned} \tag{6.17}$$

This resulting cost function can be written as

$$\sum_{l=1}^{L_k} \left|\left|\boldsymbol{z}^{\mathrm{H}}(\omega_k l) \widehat{\boldsymbol{d}}\right|\right|_2^2, \tag{6.18}$$

which is the periodogram power spectral density estimate of $\widehat{\boldsymbol{d}}$, evaluated at and summed over the harmonic frequencies $\omega_k l$ [199]. Therefore, the NLS estimator can be efficiently implemented using an FFT algorithm and a linear grid search over the discrete candidate frequencies $\left\{0, \frac{2\pi}{N}, \cdots, \frac{2\pi}{N}(N-1)\right\}$.

In this work, we are considering single dominant scatters for both breathing and heartbeat, i.e. $K = 2$. In addition, the signal models presented here are based on complex

representations. As the phase-demodulated displacement signal using the AD is real, we need to map it into complex numbers.

Breathing Rate Estimation

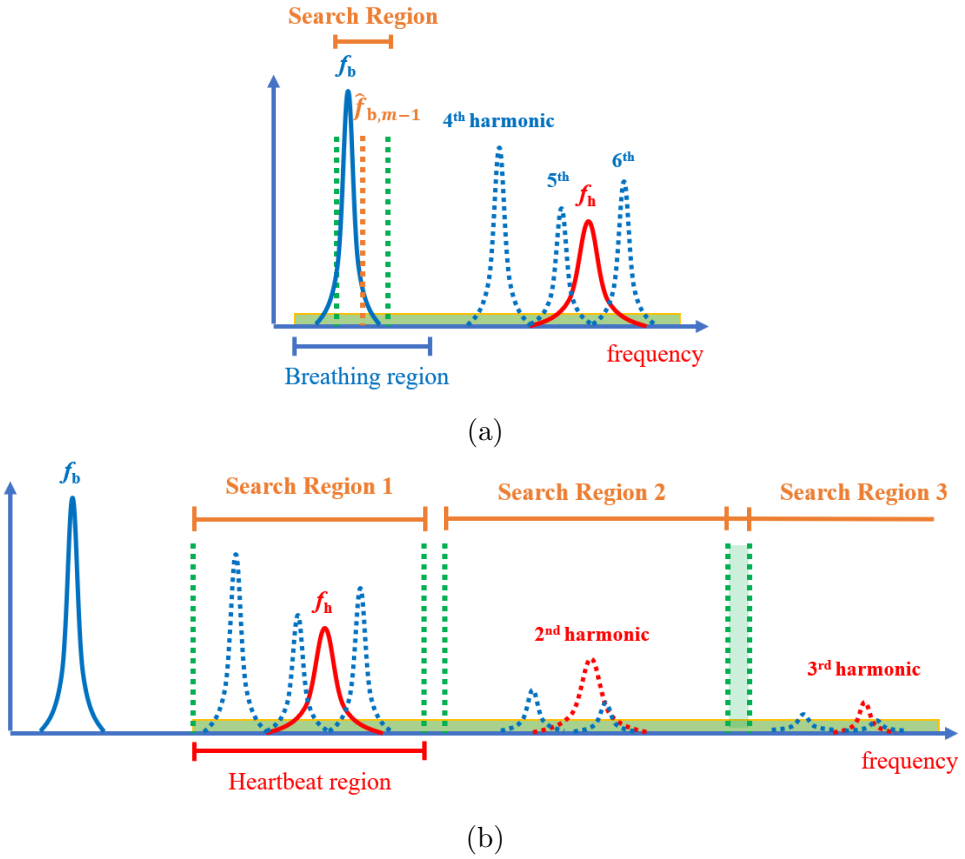

FIGURE 6.4: Adaptive NLS framework. (a) Adaptive search region for breathing rate estimation. The search region for the current processing window is defined around the previous NLS estimate. (b) Multiple search regions for heart rate estimation. In this case, multiple estimates are calculated and the Kalman filter stage adaptively selects among them.

The NLS objective function will exhibit peaks at the fundamental frequencies and its associated harmonics. Given the additive procedure in (6.18), additional peaks may also be erroneously generated at lower frequency positions. For instance, if the true breathing rate is 20 bpm, an additional peak will be generated at 10 bpm (20 bpm is its harmonic), and it may have a higher amplitude than the true one at 20 bpm. To avoid detecting these additional peaks, the NLS estimator proposed in [155, 159] uses an initial (coarse) estimation as a reference for the NLS search region, which is then limited around this value. Besides eliminating these eventual strong low-frequency components, this strategy also reduces the computational effort to perform the grid search.

In [155, 159], this initial reference estimate is obtained using a peak detection algorithm applied directly over the time-domain displacement signal. In this work, we propose a simpler implementation for that. Given the slow variation of the breathing rate over time, instead of using an additional peak detection algorithm for calculating the reference value for the NLS search region, we can use the last NLS estimate, calculated from the previous processing window. Fig. 6.4a illustrates this idea, where f_{b} represents the true breathing frequency at the current (m^{th}) processing window, and $\widehat{f}_{\mathrm{b},m-1}$ is the previous estimate. For the first processing window, the search region is initialized over the entire physiological breathing range. For the subsequent processing windows, the search region is thus limited around the reference value, and it will adaptively change according to the breathing rate variation over time. In this way, besides eliminating the additional processing for calculating a new reference at each processing window, we also avoid using possible outliers as references for the current search region.

Heart Rate Estimation

The NLS framework does not heavily depend on the white noise assumption. In fact, when the noise is white, the NLS estimates can be interpreted as maximum likelihood estimates [198]. However, the NLS estimation performance can be affected by the nonlinear objective, with multiple peaks, and a very sharp global maximum corresponding to ω_k. Hence, finding ω_k by a search algorithm requires accurate initialization [198]. In addition, some of the assumptions made in the previous section may not hold in specific cases, especially considering heart rate estimation. Particularly, for preserving the signal stationarity in each processing window, the number of samples N in $\widehat{\boldsymbol{d}}$ is often small and limited by the CPI. Therefore, it is not always possible to guarantee that the frequency components in $\{\boldsymbol{Z}_k\}$ are distinct and well separated. In fact, while breathing estimation is usually only limited by noise, the spectral region considering the fundamental frequency of the heartbeat is mainly dominated by breathing harmonics. In this way, spectral overlaps may occur and the heartbeat peak may eventually be masked by breathing harmonics.

For tackling these limitations and enable robust heart rate estimation, we extend the basic NLS approach and propose an adaptive framework for adjusting the search region over the NLS objective function. The basic idea is to generate multiple heart rate estimates based on its fundamental frequency and associated harmonics. As highlighted in [99], estimation using the fundamental heartbeat frequency (first harmonic) is mostly limited by breathing interference, whereas the estimates using higher-order harmonics are only limited by noise. This is because the fundamental heartbeat frequency "competes" with still strong 3^{rd}, 4^{th}, and 5^{th} order breathing harmonics. On the other hand, the second

and third heartbeat harmonics, for instance, share their spectral location with strongly attenuated 7^{th}, 8^{th}, and 9^{th} order breathing harmonics. The heart rate estimation can thus be improved if we look for its higher-order harmonics, far away from the strong breathing interference. However, as the amplitude of these harmonics depends on specific characteristics of the breathing and heartbeat chest wall movements, as well as on many other processing parameters, one cannot be sure these higher-order heartbeat harmonics will always be detectable. Therefore, the conventional estimation based on the heartbeat fundamental frequency is still needed. In this way, by simultaneously calculating multiple estimates, we increase the probability of detecting the correct peaks and the solution becomes more robust.

The basic NLS approach can easily be extended to provide multiple estimates by simply segmenting the NLS spectrum (objective function) into different search regions, and performing independent estimations (by finding the maximum value) over each of these regions. This can be done considering that, for a healthy subject at rest, the physiological range of the heart rate usually goes from 50 bpm to 90 bpm [220]. In this way, the search region for the fundamental frequency (first harmonic) can be set up around this range. A second search region can be defined unambiguously from 100 bpm and up to 180 bpm. Fig. 6.4b illustrates this procedure. An additional search region can also be defined, looking for the third heartbeat harmonic, from 150 bpm to 270 bpm. However, as this third region overlaps with the second one, its estimates can be ambiguous in some cases (this issue will be handled in the next section). Due to the efficient FFT-based implementation of the NLS method, we can overcome the SNR limitations reported in [99], without increasing the computation burden. In addition, this "soft" segmentation of the search regions reduces the computational complexity by only using a single bandpass filter for heartbeat estimation, in comparison to the double filtering scheme originally proposed in [99].

Kalman Filter Selection

The NLS method described above provides multiple heart rate estimates for the same processing window. It is thus necessary to come up with a single value for the heart rate estimation for each CPI. For doing this, we propose to use the Kalman filter, a recursive Bayesian algorithm that produces accurate estimates based on noisy or uncertain measurements. The Kalman filter updates its estimates and parameters sequentially as new data arrives. Therefore, it is suitable for real-time processing with the overlapped sliding windows approach commonly used for vital sign processing. As we are considering

three search regions (three estimates), we can define the measurement vector as

$$\boldsymbol{z}_{\mathrm{h}} = \begin{bmatrix} \widehat{f}_{\mathrm{r1}} & \dfrac{\widehat{f}_{\mathrm{r2}}}{2} & \dfrac{\widehat{f}_{\mathrm{r3}}}{3} \end{bmatrix}^{\mathrm{T}}, \tag{6.19}$$

where $\widehat{f}_{\mathrm{r1}}$, $\widehat{f}_{\mathrm{r2}}$ and $\widehat{f}_{\mathrm{r3}}$ represent the estimates originated from the first, second, and third search regions, respectively.

The generic state vector has the form

$$\boldsymbol{x} = \left[f_{\mathrm{h}} \; f'_{\mathrm{h}} \; f''_{\mathrm{h}} \right]^{\mathrm{T}}, \tag{6.20}$$

where f_{h}, f'_{h}, and f''_{h} represent, respectively, the heart rate and its first and second-order derivatives. From the current state $\widehat{\boldsymbol{x}}_{m,m}$, at the m^{th} processing window, the predicted state $\widehat{\boldsymbol{x}}_{m+1,m}$ can be calculated using the state transition equation, defined as

$$\widehat{\boldsymbol{x}}_{m+1,m} = \begin{bmatrix} 1 & \Delta t & \frac{\Delta t^2}{2} \\ 0 & 1 & \Delta t \\ 0 & 0 & 1 \end{bmatrix} \widehat{\boldsymbol{x}}_{m,m} = \boldsymbol{F}\widehat{\boldsymbol{x}}_{m,m}, \tag{6.21}$$

where $\boldsymbol{F}$ is the state transition matrix, with Δt being the time between each new set of NLS estimates. To describe the dynamics of the frequency variation over time, we are using the constant acceleration model, as suggested in [141].

The state vector represents a Gaussian process with mean $\widehat{\boldsymbol{x}}_{m,m}$ and covariance $\boldsymbol{P}_{m,m}$. The extrapolated covariance can be calculated as

$$\boldsymbol{P}_{m+1,m} = \boldsymbol{F}\boldsymbol{P}_{m,m}\boldsymbol{F}^{\mathrm{T}} + \boldsymbol{Q}, \tag{6.22}$$

where $\boldsymbol{Q}$ is related to the process noise uncertainty and can be modeled as $\boldsymbol{Q} = \boldsymbol{g}\boldsymbol{g}^{\mathrm{T}}\rho_a^2$ [141], with

$$\boldsymbol{g} = [0.5\Delta t^2 \; \Delta t \; 1]^{\mathrm{T}}, \tag{6.23}$$

and ρ_a^2 representing the process noise. With the observation matrix

$$\boldsymbol{H} = \begin{bmatrix} 1 & 0 & 0 \\ 1 & 0 & 0 \\ 1 & 0 & 0 \end{bmatrix}, \tag{6.24}$$

we can calculate the measurement innovation (error) as

$$\boldsymbol{e}_m = \boldsymbol{z}_{\mathrm{h}} - \boldsymbol{H}\widehat{\boldsymbol{x}}_{m+1,m}, \tag{6.25}$$

and its associated covariance given by

$$\boldsymbol{S}_m = \boldsymbol{H}\boldsymbol{P}_{m+1,m}\boldsymbol{H}^{\mathrm{T}} + \boldsymbol{R}, \tag{6.26}$$

with $\boldsymbol{R}$ being a diagonal matrix containing the uncertainty in the NLS estimates for each search region, i.e.

$$\boldsymbol{R} = \begin{bmatrix} \sigma_{r1}^2 & 0 & 0 \\ 0 & \sigma_{r2}^2 & 0 \\ 0 & 0 & \sigma_{r3}^2 \end{bmatrix}. \tag{6.27}$$

The algorithm is initialized with predefined $\boldsymbol{Q}$ and $\boldsymbol{R}$ matrices, and initial state $\widehat{\boldsymbol{x}}_{0,0}$ with covariance $\boldsymbol{P}_{0,0}$. If at least one of the NLS estimates is close enough to the predicted state in (6.21) (within a predefined gating threshold), we select from $\boldsymbol{z}_{\mathrm{h}}$ the estimate which minimizes the distance between the new measurement and the filter prediction. Subsequently, we can update the state vector as

$$\widehat{\boldsymbol{x}}_{m+1,m+1} = \widehat{\boldsymbol{x}}_{m+1,m} + \boldsymbol{k}_m e_m(z), \tag{6.28}$$

where z is the index corresponding to the selected NLS estimate, with the Kalman gain $\boldsymbol{k}_m$ being calculated as

$$\boldsymbol{k}_m = \frac{\boldsymbol{P}_{m+1,m}\boldsymbol{h}_z}{S_m(z,z)}, \tag{6.29}$$

where $\boldsymbol{h}_z^{\mathrm{T}}$ is the z^{th} row of $\boldsymbol{H}$ and $S_m(z,z)$ is the z^{th} diagonal element of $\boldsymbol{S}_m$. Finally, the associated covariance

$$\boldsymbol{P}_{m+1,m+1} = (\boldsymbol{I} - \boldsymbol{k}_m\boldsymbol{h}_z^{\mathrm{T}})\boldsymbol{P}_{m+1,m}, \tag{6.30}$$

is also calculated in order to be used in the next filter iteration.

If none of the NLS estimates fall within the gate, we treat all of them as outliers. The Kalman gain is then set to zero and the final estimate will only be based on the predicted state. However, if this condition holds during several adjacent processing windows, it may indicate that the state estimate has diverged. In this case, we reset the updated covariance in (6.30) to its initial (large) value, in order to allow the filter to reacquire.

The final heart rate estimate $\widehat{f}_{\mathrm{h}}$ for the m^{th} processing window is directly obtained from the updated state vector in (6.28), and the algorithm runs for each processing window with the updated state vector, its updated covariance, and a new set of NLS estimates $\boldsymbol{z}_{\mathrm{h}}$ as inputs.

At each iteration, based on its own prediction, the proposed algorithm selects the best estimate among the three NLS search regions, or can even discard all of them. In this

way, we are exploring the temporal information relative to the evolution of the heart rate over time. This knowledge is often neglected by previous approaches that estimate independently at each processing window. Finally, this procedure provides adaptivity to different scenarios, by avoiding wrong estimates that could be originated from harmonic-interfered spectral regions around the heartbeat fundamental frequency, or from low-SNR and ambiguous detections when estimating using higher-order harmonics at the second and third search regions.

6.2.5 Experimental Results

For the experiments, we are using a Texas Instruments (TI) mm-wave FMCW radar (AWR1642 [150]), operating at 79 GHz with a 4-GHz bandwidth. The radar is configured for using a single transmitter and 4 receiver channels. The total duration of each chirp is 64 μs, with an inter-frame period of 10 ms, corresponding to a slow-time sampling frequency of 100 Hz. For providing sufficient integration time, while still preserving the update rate, the data is processed using overlapped sliding windows with a duration of 30 s, with 29 s of overlap, which results in updated estimates every $\Delta t = 1$ s. The NLS search region for breathing estimation was initialized from 8 bpm to 30 bpm and later reduced to ± 2 bpm around the reference (previous) estimate. For the heart rate estimation, the search regions were defined as described in Section 6.2.4. The number of harmonics for the NLS estimation was defined as $L_1 = 5$ for breathing and $L_2 = 3$ for the heart rate. The Kalman filter parameters were initialized as follows: $\rho_a = 2$, $\sigma_{r1} = \sigma_{r2} = \sigma_{r3} = 1.5$ and $\boldsymbol{P}_{0,0} = 1000\boldsymbol{I}$. The initial state is defined as $\widehat{\boldsymbol{x}}_{0,0} = [4\widehat{f}_b \ 0 \ 0]^{\mathrm{T}}$, where $\widehat{f}_b$ is the estimated breathing rate at the first processing window. This specific heart rate initialization value of $4\widehat{f}_b$ is based on the human pulse-respiration quotient, which follows a log-normal distribution centered around four [221, 222].

Fig. 6.5a shows the measurement setup, where 5 subjects (all male) with different age (27-36 years), height (170-192 cm) and weight (60-90 kg), were asked to stay seated in front of the radar, breathing normally, at approximately a 1-meter distance. The wearable commercial device named Hexoskin [153] was used as a reference for true breathing and heart rates. It has two inductance plethysmography sensors (chest and abdomen) for measuring breathing, and a 1-lead electrocardiograph for the heartbeat. This device has already been extensively validated for vital sign monitoring in different conditions [154, 223]. The tests emulated different conditions of movement which are common to an office work environment. The objective was to understand if small random movements from hands, arms, and shoulder, which are very close to the chest, could jeopardize estimation. Besides being static, three other scenarios were emulated:

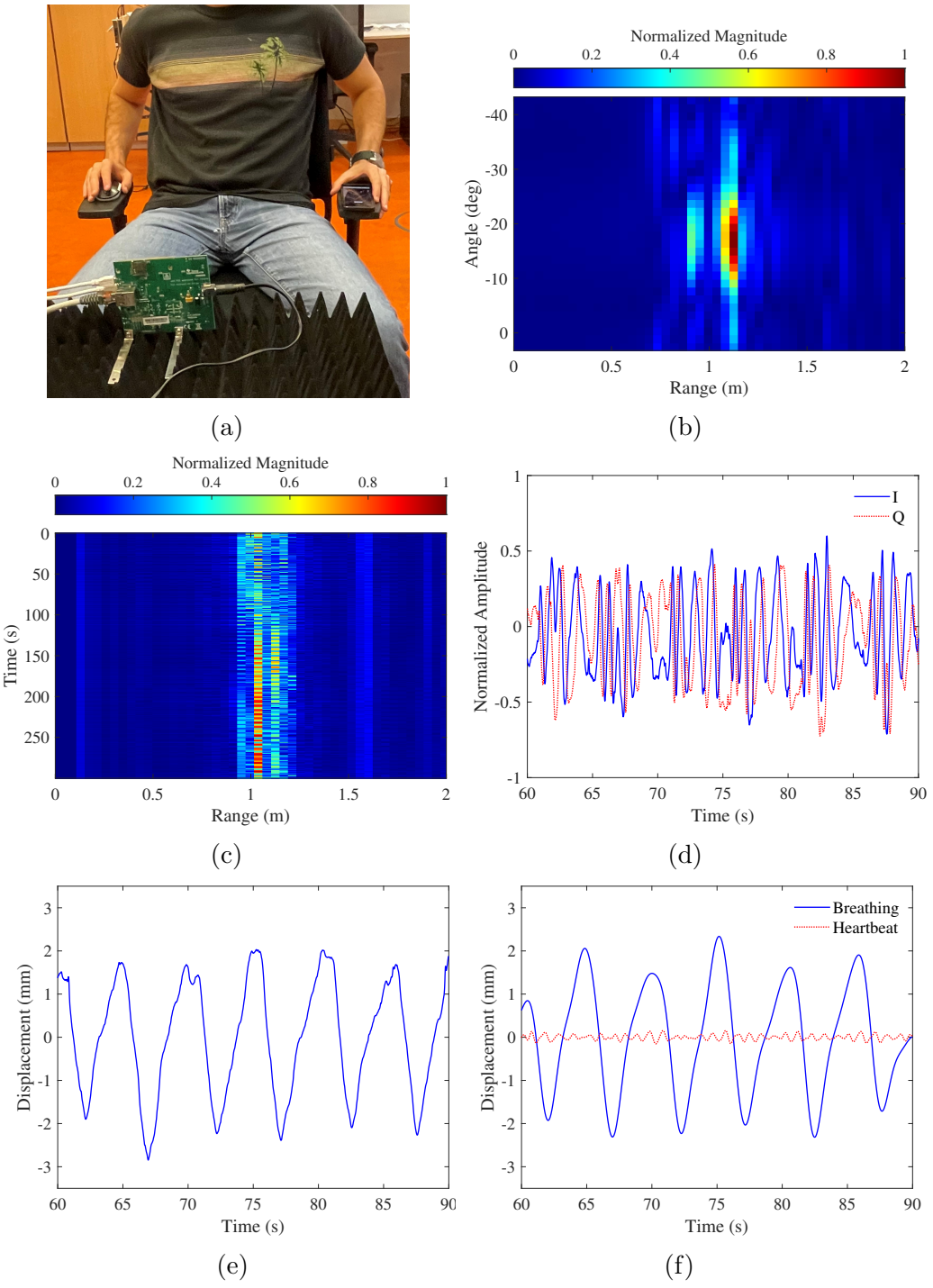

FIGURE 6.5: Vital sign monitoring example. (a) Measurement setup, with the monitored subject seated in front of the radar, at approximately 1 m distance. (b) Range-angle map. (c) Range-profile. (d) A segment of the slow-time signal (I and Q samples) from the target range bin. (e) Phase-demodulated chest wall displacement signal. (f) Bandpass-filtered signals for breathing and heartbeat.

1) holding a phone and texting, **2)** typing on a keyboard, and **3)** controlling a mouse device ("mousing").

Fig. 6.5b and Fig. 6.5c show, respectively, the range-angle map and the range profile, at

the output of the preprocessing block. The energy is mostly concentrated at the detected range bin, but it also spreads over adjacent range bins due to the high range resolution. This allows us to add up correlated range bins for improving the SNR as described in Section 6.2.3. The slow-time signal (I and Q samples) at the target range bin can be seen in Fig. 6.5d. After phase demodulation, the recovered chest wall displacement is depicted in Fig. 6.5e, with its bandpass-filtered versions for breathing and heartbeat in Fig. 6.5f. The periodic pattern is clearly seen, as well as the large-amplitude difference between the breathing and heartbeat signals.

Fig. 6.6a shows the results for a single measurement of 5 minutes. It compares breathing rate estimates obtained using the proposed ANLS framework, with the conventional DFT estimation [147, 157, 217] (commonly used as benchmark), and the true values from the reference wearable device. It can be seen the high correlation between measurements where, most of the time, both techniques provided radar estimates within the ±1 bpm error interval. Similarly, Fig. 6.6b compares the obtained heart rate estimates with the true values from the reference device, for the same measurement of 5 minutes. In this case, while the proposed ANLS framework provided most estimates within the ±2 bpm error interval, the conventional DFT estimation is highly affected by breathing harmonics, specially when the breathing frequency is higher.

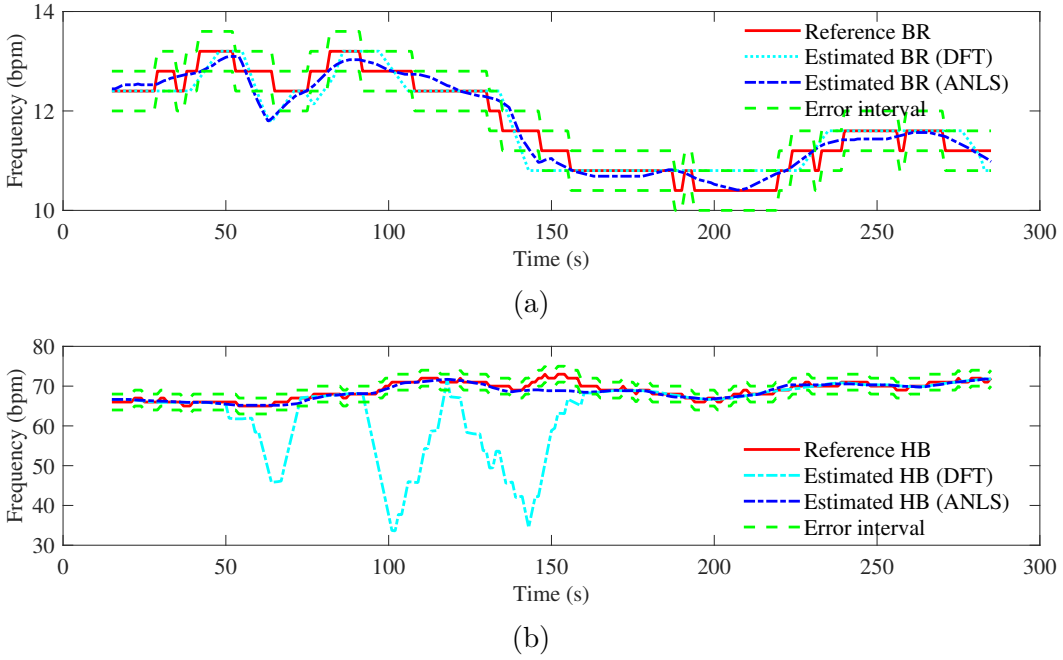

FIGURE 6.6: Comparison between radar and reference device, for a single measurement of 5 minutes. (a) Estimated breathing rate using conventional DFT estimation and the proposed ANLS framework, actual values from the reference device, and corresponding 1-bpm error interval. (b) Estimated heart rate using conventional DFT estimation and the proposed ANLS framework, actual values from the reference device, and corresponding 2-bpm error interval.

Fig. 6.7a shows one example of the chest wall displacement signal under the influence small random body movements ("typing" scenario). The corresponding estimation results and comparison to the reference device are depicted in Fig. 6.7b. This example demonstrates the continuous nature of the emulated random body movements, which differentiate this work from previous literature [93, 224, 225], where emulated movements are short and sparse episodes. These results clearly show how the conventional DFT estimation is strongly affected by the additional interference, whereas the proposed ANLS approach can still provide accurate heart rate estimation with minor performance degradation.

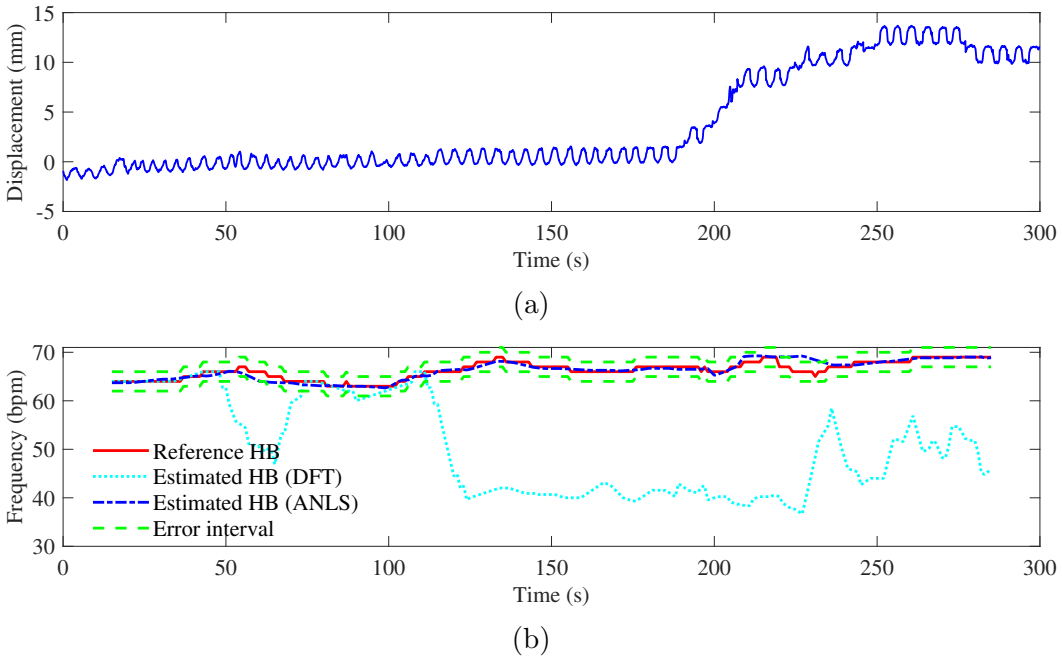

FIGURE 6.7: Measurement under continuous interference of small random body movements ("typing" scenario). (a) Phase-demodulated chest wall displacement signal. (b) Estimated heart rate using conventional DFT estimation and the proposed ANLS framework, actual values from the reference device, and corresponding 2-bpm error interval.

The obtained results are summarized in Table 6.1, which shows the average accuracy and RMSE for each scenario, comparing the proposed solution with the conventional DFT estimation, and the basic NLS approach from [155]. The same preprocessing steps (phase demodulation and bandpass filtering) were used in all cases. The accuracy is calculated as the percentage of time (in terms of processed windows) during which the final estimation from the radar is within a predefined error interval (threshold) in relation to the reference value. For instance, a 1-bpm accuracy of 80% means that the magnitude of the error between radar estimation and the reference device was smaller than 1 bpm for 80% of the time (processing windows). In this work, we considered fixed values of 1-bpm accuracy for breathing and 2-bpm accuracy for the heartbeat. These intervals are below common values for the threshold of clinical acceptance [165, 226]. The RMSE is

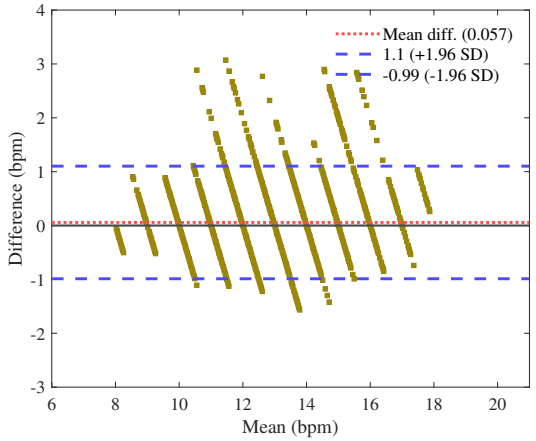

(a)

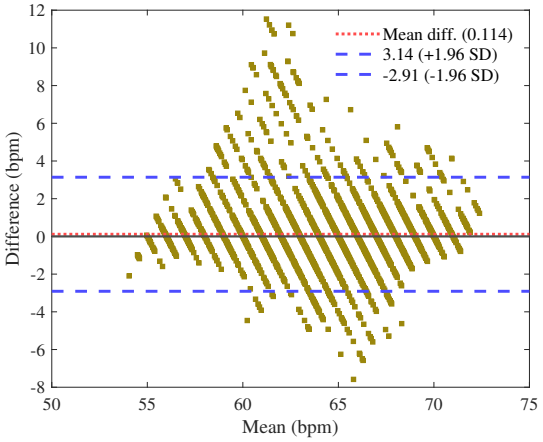

(b)

FIGURE 6.8: Bland-Altman Analysis. (a) Breathing estimation, considering all measurements. (b) Heart rate estimation, considering all measurements.

defined as

$$\text{RMSE} = \sqrt{\frac{1}{M}\sum_{i=1}^{M}(\widehat{f}_i - f_i)^2}, \tag{6.31}$$

where $\widehat{f}_i$ and f_i represent, respectively, the estimated and true (reference) frequency values (in bpm) in the i^{th} processing window, and M is the total number of processing windows.

TABLE 6.1: Average accuracy and RMSE for different scenarios and techniques

Scenarios	**Breathing**						**Heartbeat**					
	Accuracy (%)			**RMSE (bpm)**			**Accuracy (%)**			**RMSE (bpm)**		
	DFT	NLS	ANLS	DFT	NLS	ANLS	DFT	NLS	ANLS	DFT	NLS	ANLS
Static	86.7	91.0	98.5	0.65	1.07	0.43	49.9	96.7	97.6	12.8	0.84	0.76
Texting	75.7	95.3	96.9	0.67	0.55	0.44	33.4	92.7	91.0	17.8	1.16	1.17
Typing	83.0	94.9	94.6	0.72	0.60	0.62	16.5	85.2	91.1	23.2	1.98	1.30
"Mousing"	83.2	96.8	96.8	0.71	0.57	0.52	45.4	81.0	81.3	15.4	2.50	2.27

It can be seen how the proposed framework provides accurate and robust breathing and heart rate estimation in all conditions, with minor performance loss in the scenarios with additional movement. The most challenging situation arises when moving the arms back and forth for controlling the mouse device. Besides overlapping nearby range bins, this movement has a similar behavior as the chest wall displacement, but with much stronger amplitudes.

In the case of breathing, the proposed solution provided slightly better performance when comparing to the conventional DFT estimation in all scenarios. The reason is that, in the absence of strong interfering movements, the breathing displacement signal already dominates the spectrum and thus simple DFT estimation is sufficient for reasonable performance. In the case of heart rate estimation, due to the reduced SNR and the presence of breathing harmonics, the conventional DFT completely fails to provide accurate estimates. The proposed solution provided significant improvement over all scenarios, with the best result in the static case, with 97.6% of accuracy. The RMSE was strongly reduced in all cases, reaching the best performance with 0.76 bpm in the static scenario. The most challenging condition arises when the monitored subjects were controlling the mouse device, with the accuracy reducing to 81.3% and the RMSE increasing to 2.27 bpm.

Fig. 6.8a shows the Bland-Altman plot considering the obtained ANLS breathing rate estimates for all measurements and scenarios. The mean bias was only 0.057 bpm, with 95% upper and lower limits of agreement (LOAs) of 1.1 bpm and -0.99 bpm, respectively. These values are well within the expected interval for clinically acceptance [45]. Similarly, Fig. 6.8b shows the Bland-Altman plot considering the ANLS heart rate estimates for all measurements and scenarios. The mean bias was only 0.114 bpm, with LOAs of 3.14 bpm and -2.91 bpm. These results show very good agreement between radar estimates and the reference device, with comparable or smaller LOAs than recent studies [94, 136, 227], for both breathing and heart rate estimation.

To better evaluate the impact of the proposed ANLS solution for heart rate estimation, Fig. 6.9 shows the percentage of use for each of the search regions (illustrated in Fig. 6.4b). At each processing window, the Kalman filter adaptively selects the best estimate from one of the three search regions. The main bars show the average utilization of each region considering all scenarios, whereas the error bars show the maximum and minimum values obtained in one of the measurements. Even though, most of the time, the estimate from the first region (fundamental frequency) is used, estimates from the second and third regions are used on average in 24.3% and 11.6% of the processing windows, respectively. And these values rise to approximately 44% and 21%, respectively, at specific measurements. This means that, on average, more than 35% of the time the

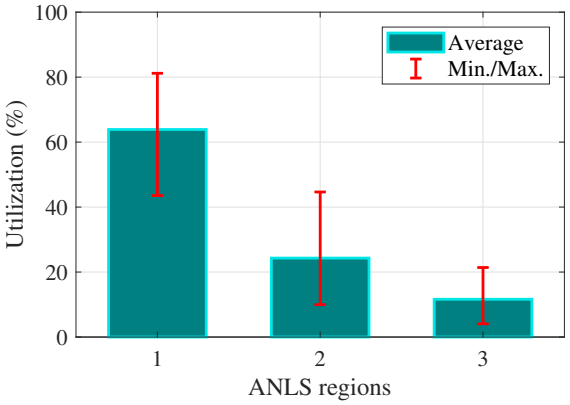

FIGURE 6.9: Utilization of ANLS estimates from different search regions considering all measurements.

spectral region around the fundamental heartbeat frequency is dominated by breathing harmonics or any other additional interference. It confirms the significance of providing multiple estimates from different spectral regions, with an additional smart mechanism to select among them.

TABLE 6.2: Comparison of heart rate estimation performance considering different solutions

	Device	Freq. (GHz)	Dist. (m)	RMSE (bpm)	Accuracy (%) / threshold	Scenario
[132]	FMCW	76-81	1.0	2.53	-	Seated, still
[228]	IR-UWB	7.29	1.0	2.1	-	Lying (supine), still
[229]	FMCW	8.4	1.5	> 1.0	-	Seated, still
[230]	Doppler	2.4	0.5-1.5	1.60	-	Seated, still
[138]	FMCW	60	1.0-2.5	-	85.6 / 4 bpm	Seated, still
[231]	FMCW	61	0.4-1.4	-	83.9 / 5 bpm	Seated, still
[107]	CW	2.4	1.0	-	93.8 / 2 %	Seated, still
[232]	Doppler	10.5	1.5	-	95 / 2 bpm	Seated, still
[133]	FMCW	120	1.0	-	93.7 / 3 %	Seated, still
ours	FMCW	77-81	1.0	0.76	97.6 / 2 bpm	Seated, still
			1.0	1.58	87.8 / 2 bpm	Seated, moving
			1.5	1.25	92.9 / 2 bpm	Seated, still
			2.0	1.71	87.2 / 2 bpm	Seated, still
			2.5	2.53	67.0 / 2 bpm	Seated, still

An additional experiment was also performed at increasing distances from 1.5 m to 2.5, with 5 measurements while seating still at each position. The obtained results are summarized in Table 6.2, which compares the average performance for heart rate estimation in all scenarios with recently proposed solutions, validated in similar experimental conditions. It can be seen that, despite its simple implementation, the proposed ANLS framework outperforms these methods, resulting in higher accuracy and smaller RMSE values. In addition, when considering the scenarios with additional movement (texting, typing and "mousing"), the average results show robust performance even

during small and continuous body movements. Furthermore, at longer distances, despite an expected performance degradation, the results are promising with RMSE values still within thresholds of clinical acceptance [165, 226].

Computational Time

To estimate the computational time of the proposed approach we processed different measurements several times and recorded the average processing time considering all scenarios. Given that we have a new processing window at every second, we can obtain an estimate of the average computational time for each iteration (processing window). We repeated this procedure using the conventional DFT estimation, the simple NLS method and the complete ANLS approach. In relation to the conventional DFT estimation, the obtained results show an increase in the computational time around 22% and 42% for the simple NLS method and the complete ANLS framework, respectively.

6.2.6 Conclusion

In this paper, we presented a complete framework for vital sign processing using a 79-GHz FMCW device. The solution is based on a simple but accurate adaptive nonlinear least-squares framework that explores the inherent harmonics existing in the periodic chest wall displacement signal. In the case of heart rate estimation, an additional Kalman filter stage adaptively selects among multiple estimates originated from different search regions. The solution was evaluated with real human data collected while imitating common working conditions in an office environment. Most of the time the radar provided measurements within the predefined error intervals, being capable of tracking the reference values even during continuous small body movements. Due to the similar behavior to the chest wall movement, the most challenging scenario resulted from controlling the mouse device with back-and-forth arms movements. The final accuracy and RMSE values showed robust and accurate estimation, outperforming conventional spectral estimation and other recently proposed methods in almost all scenarios.

The proposed solution has still limitations under moderate to strong random body movements, especially when this interference leads to phase demodulation errors by using the AD. This will be the main direction of future work. Moving toward a complete solution for vital sign monitoring, additional investigation is also required to understand the effects of dynamic scenarios with multiple moving subjects and multi-path reflections.

Chapter 7

Discussion

This is the last chapter of this thesis, with the aim to summarize and connect our contributions to the contactless monitoring of vital signs using radar devices. In addition, we will also discuss relevant aspects regarding the practical deployment of this technology, and what remains as interesting research avenues.

7.1 Analysis of the contributions

The careful reader may have noticed that the chronological order of the presented manuscripts, and their corresponding contributions, does not match the sequential order in the basic signal processing block diagram. In fact, our first contribution, the NMF-based RBM mitigation algorithm presented in Chapter 5, is related to the Filtering block. Later, we moved to heart rate monitoring in a different scenario, and the challenge of suppressing the harmonic interference from breathing over the heartbeat signal. For accomplishing this, we proposed the ANLS estimation framework, which is related to the Estimation block. Finally, in Chapter 4, we came back to the Phase demodulation block and proposed the use of US for robust recovery of the chest displacement signal in different conditions.

An unfortunate consequence of this mismatched order is the fact that our contributions were not cumulative, *i.e.*, the solution corresponding to the last stage in the signal processing block diagram does not integrate the improvements obtained at previous stages. We will now try to fill this gap (at least theoretically) by presenting, in Fig. 7.1, our suggestion for the complete block diagram for radar-based contactless monitoring of vital signs.

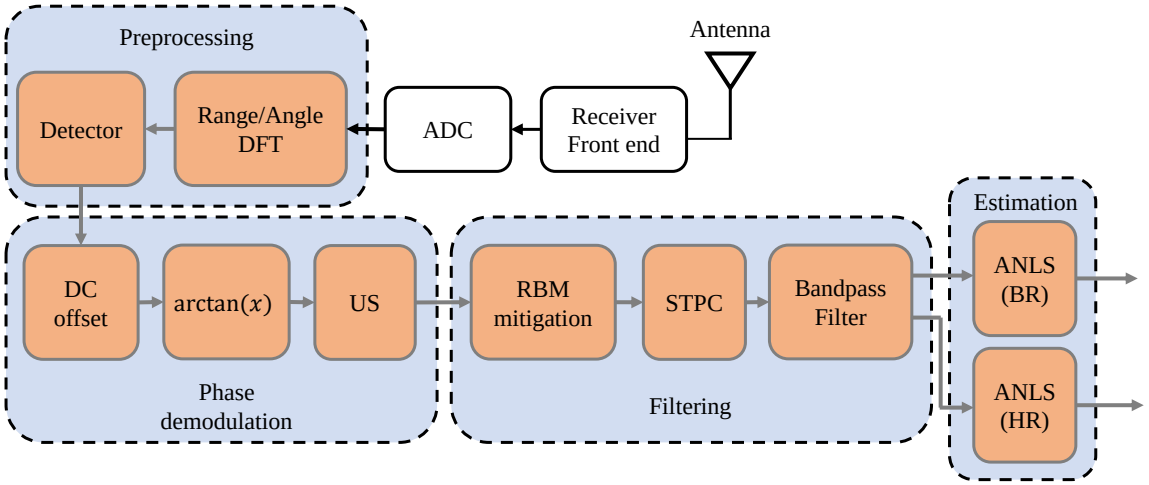

FIGURE 7.1: Complete signal processing block diagram.

As discussed in Section 2.4.1, the Preprocessing stage receives the digitized signals from the ADCs and tries to extract the slow-time signal, corresponding to a specific range and angle position where the monitored subject is located. Most of the time, classic radar signal processing techniques are used at this stage.

In the Phase demodulation stage, we propose to use the US demodulation. This includes the usual DC offset compensation and the arctangent operation, followed by the US framework replacing the conventional unwrap algorithm. As discussed in Chapter 4, the classic unwrap algorithm has limitations in practical situations, especially when dealing with interfering RBMs from the monitored subject. Using the US demodulation enables precise recovery of the chest wall displacement signal, including the additional RBMs that may be present in the processing window.

At first sight, our desire to precisely recover also the RBM signal may look counter-intuitive. However, at this stage, there are two important reasons for this. The first one was already discussed in Section 4.2.5: if the interfering RBM signal is not spectrally overlapped with the vital sign information, it will be easily removed by conventional spectral analysis at the Filtering stage. However, inaccurate demodulation of the RBM signal may introduce nonlinear errors that can spread the spectral energy over the entire bandwidth. This can hinder filtering even under the simplest interfering scenario. The second reason is related to the RBM mitigation algorithm proposed in Chapter 5. There, we assumed that the RBM signal is inherently sparse and, most of the time, much stronger than the breathing and heartbeat signals. Precise recovery of the RBM signal will preserve these characteristics that are fundamental to allow its separation from the vital sign information by using the NMF factorization.

In the Filtering stage, the recovered displacement signal must be further processed to improve the SINR before estimation. In the complete block diagram, we propose to first use the NMF-based RBM mitigation algorithm, which will remove additional interfering components.

Subsequently, the isolated displacement signals from adjacent range bins can be combined using the slow-time phase correlation (STPC) proposed in Chapter 6, Section 6.2.3. As we discussed there, when operating in the mm-wave region, the human body becomes an extended target and its energy may spread across a few adjacent range bins. Given that the belly, back, and shoulders are also involved in the cardiorespiratory movements, vital sign information may eventually be detected in these additional range bins. The STPC will efficiently recombine these signals to improve the SNR while still preserving the relevant frequency content. Finally, the enhanced chest wall displacement signal can be bandpass-filtered to separate the breathing and heartbeat components.

In the Estimation stage, the ANLS framework, proposed in Chapter 6, can be used for calculating the vital sign frequencies. As demonstrated by the results in Table 6.1, for breathing rate estimation, the Kalman filter is not necessary and the adaptation comes from adjusting the NLS search region according to previous estimates from adjacent processing windows. For heart rate estimation, despite the techniques employed at the Filtering stage, most of the time we will still need to deal with the harmonic interference from breathing. In this case, the ANLS estimator can use the harmonics from the heartbeat signal to generate multiple heart rate estimates from different spectral regions. The Kalman filter will then use its gating process to select the best estimates, thus avoiding erroneous candidates originating from harmonic interfered, low-SNR, or ambiguous regions.

7.2 On the practical deployment

Despite the recent technological developments, the adoption of novel patient monitoring systems, including contactless devices, remains a lagging process. In fact, most of the ICU monitoring devices used today, such as ECGs, were already available 50 years ago. Major reasons for this slow progress include the lack of awareness and trust in new technologies, a mismatch of expectations and assumptions by clinical users and manufacturers, and the fear that the adoption of new devices would lead to an increased workload [61]. Behind these reasons lies the main concern about reduced accuracy, and that it could lead to

more false alarms due to unusual (out-of-threshold) estimated values. This could increase the risk of "alarm fatigue"[1] and compromise patient care [72].

Interestingly, alarm fatigue is not a new issue. In fact, it is considered a major limitation of current continuous monitoring systems. Surprisingly, recent research indicates that around 70% (at least) of all alarm signals in the critical care environment are false or non-actionable [61, 233]. As a consequence, a nurse can spend up to 20 minutes per day managing alarms from existing systems, detracting from essential aspects of patient care [72].

Besides inadequate alarm setup due to the lack of staff training and resources, one of the reasons for this situation is related to the current device's susceptibility to errors, especially when dealing with interfering artifacts caused by additional body movements [61]. In fact, there is still an open debate among clinicians on the reliability of current monitoring devices [234]. Regarding breathing monitoring, for instance, there is a paucity of research comparing continuous contact-based monitoring methods (*e.g.*, impedance pneumography and ECG-derived) to visual inspection [43], which is still considered the gold standard for breathing assessment.

In addition, several studies suggest that current patient monitors have relatively simplistic built-in data processing for artifact detection, usually employing a reductionist approach that oversimplifies human physiology [234]. To reduce the occurrences of interfering artifacts, the general recommendation from manufacturers is that the patient should be static. In general, performance is not guaranteed if the patient is moving. This limitation is well-known and most manufacturers already highlight this information in the operating manuals of these devices [206]. In fact, we experienced and discussed this issue in Chapter 5. When the babies were moving, a high level of ADC saturation was observed in the raw data of the reference cabled device. Certainly, in these moments, the reference device will not be able to generate accurate estimates and, therefore, it is not reliable.

These limitations of current devices may bring up technical and philosophical discussions on their reliability. This is especially important considering that, throughout the design and validation of new monitoring devices, the current ones are commonly used as references and ground truth for performance validation. And, sometimes, the investigated scenarios include the ones in which the reference device may not be working properly, *e.g.* while the patient is moving.

[1] Alarm fatigue occurs when clinicians have to deal with so many false or non-actionable alarms that they become desensitized [233]. False alarms occur when there is an invalid triggering event, whereas non-actionable alarms are related to events with no clinical relevance.

In summary, despite being genuine, these general concerns about the adoption of new devices seem to be more related to the change of *status quo* rather than a true technical issue.

Therefore, to increase the benefit and acceptance of new monitoring technologies, it is crucial to include all stakeholders, especially the medical staff, in the implementation and, ideally, also in the development and validation of these solutions. This cooperation should involve product engineering aspects such as usability, interoperability, training, and frequent evaluation and feedback. This is the only way to ensure that stakeholders are confident and engaged in the new solution [59]. In our work at the NICU, we attempted to close this gap by bringing together research, industry, and medical staff, throughout the early development of our solution.

Another common concern when considering wireless devices relates to exposure to electromagnetic radiation. However, VSM applications are mainly focused on very short-range and indoor scenarios, where the monitored subject is usually very close to the device. As a consequence, most solutions in the literature (including the ones shown in this thesis) use devices emitting very low power at non-ionizing frequencies. Radiation levels are usually smaller than those from conventional communication systems operating within accepted standards. Nevertheless, careful consideration of potential risks for long-term exposure must be considered before the widespread adoption of radar technologies for contactless monitoring of vital signs [76].

Finally, regulatory approval is required for the clinical deployment of these systems at a broad scale. Physiological monitoring systems are considered Class II devices by the US Food and Drug Administration (FDA), with well-defined requirements for testing and performance [235, 236]. When considering non-critical consumer applications, the required accuracy of such systems is unclear as they straddle a grey zone between a medical device and a consumer product [72]. Approval for use in critical care settings will surely require larger and more complete clinical trials.

7.3 Future work

Despite the good performance and robustness of the proposed US phase demodulation, our initial study was purely theoretical and limited to the noiseless scenario. Due to the difficulties in providing ground truth for the interfering RBMs, we could not use previously collected data or perform new measurements. A thorough investigation of this method in practical scenarios is still necessary.

Whereas the integration of NMF-based RBM mitigation algorithm to the US demodulation is straightforward, there are two important aspects that require further investigation. The first one was already mentioned at the end of Chapter 5, and it refers to the NMF factorization algorithm. We can use our prior knowledge about the signal structure (*e.g.* the periodicity of the displacement signal, and/or the sparsity of the RBM signal) to improve the factorization by imposing constraints on either $\boldsymbol{W}$ or $\boldsymbol{H}$. For instance, there are already several "sparse" NMF implementations [197] and we believe that using one of these algorithms could greatly improve the separation between the vital sign information and the interfering signals.

The second aspect relates to the inherent time/frequency resolution trade-off when using the STFT prior to the NMF factorization. In our work, we used short STFT windows (3 seconds) with larger overlaps (2 seconds) in order to increase the time resolution and improve RBM detection using the time basis on $\boldsymbol{H}$. However, larger STFT windows would rather increase frequency resolution and improve the frequency separation between the desired information and the interfering signals. This would enable RBM detection by using the frequency basis on $\boldsymbol{W}$. In addition, this approach would also allow direct use of the filtered spectrogram $\widehat{\boldsymbol{X}}$ for instantaneous frequency estimation. In this way, we could eliminate the inverse STFT step (please refer to Section 5.2.5), thus resulting in reduced computation complexity.

Regarding the proposed ANLS framework, while we understand that breathing rate estimation performance is already good enough for practical deployment, some work can still be done to improve heart rate estimation. Particularly, our implementation of the Kalman filter is still simplistic, and a deeper investigation of the related models and parameters may result in interesting outcomes. An interesting direction of study would be the joint breathing/heart rate estimation, by exploring prior knowledge about their relation, *e.g.* the pulse-respiration quotient [221, 222], and the associated harmonic positions. This additional information can be embedded in the dynamic model of the Kalman filter or even before, in the NLS estimation.

At the NICU, we are already investigating radar performance for the heart rate monitoring of premature newborns. We are now using a MIMO FMCW radar, at a higher operating frequency, which will enable not only range isolation from external interference but also to steer the radar's field-of-view directly to the monitored infant. In addition, MIMO beamforming capabilities will also enable simultaneous monitoring of both infants during the co-bedding of twins.

Despite our attempt to move a bit forward in investigating more realistic scenarios, there is still a big gap when considering the practical deployment of a radar-based solution for contactless monitoring of vital signs. Several challenges still need to be addressed, most

of them related to the dynamics of monitoring in a practical environment. Particularly, interesting, yet unanswered, research questions arise when monitoring multiple subjects moving freely.

Even though target separability, tracking, and range migration are classic radar problems, they become much more complex when considering the simultaneous extraction and processing of vital sign information when the monitored subjects are moving. The longer CPIs needed for acquiring at least a few breathing cycles yield to an additional energy trade-off. For instance, if considering a processing window of 12 seconds (only 2 breathing cycles at a breathing rate of 10 bpm), the monitored subject can move around 10 meters while walking slowly. This means that the vital sign energy will be spread over dozens of range/angle cells, which can completely jeopardize detection and estimation.

Speaking is another major challenge for both breathing and heartbeat monitoring. When we speak, the breathing pattern becomes irregular and speech-dependent. The additional body movements will also interfere and can easily mask both breathing and heartbeat signals. In this case, the interfering RBMs may become less sparse and, therefore, more difficult to identify and filter out using the technique proposed in Chapter 5.

An intuitive step to overcoming all these challenges is moving to a multi-modal multi-sensor approach, including distributed radar sensing and cameras. This would allow additional degrees of freedom to extract the vital sign information and remove the RBM interference. In this case, sensor fusion becomes a key and challenging aspect, and specific complexity and cost analysis will be required according to the intended application.

Finally, machine and deep learning techniques could be used in many different ways to improve radar performance, especially considering the complex physiology behind the chest wall displacement signal and the difficulty in obtaining precise mathematical models for representing it. The inherent challenge that arises, in this case, is how to provide enough data for training.

Investigating these remaining questions will be the main direction of our future work.

Bibliography

[1] World Health Organization, "Ageing and health," (accessed in December, 2022).

[2] Y. Han, T. Lauteslager, T. S. Lande, and T. G. Constandinou, "UWB Radar for Non-contact Heart Rate Variability Monitoring and Mental State Classification," in *2019 41st Annu. Int. Conf. IEEE Eng. Med. Biol. Soc.* IEEE, jul 2019, pp. 6578–6582.

[3] V. P. Tran, A. A. Al-Jumaily, and S. M. S. Islam, "Doppler Radar-Based Non-Contact Health Monitoring for Obstructive Sleep Apnea Diagnosis: A Comprehensive Review," *Big Data Cogn. Comput.*, vol. 3, no. 1, p. 3, jan 2019.

[4] W. Massagram, V. M. Lubecke, A. Høst-Madsen, and O. Boric-Lubecke, "Assessment of heart rate variability and respiratory sinus arrhythmia via doppler radar," *IEEE Trans. Microw. Theory Tech.*, vol. 57, no. 10, pp. 2542–2549, 2009.

[5] R. P. Gaynes *et al.*, "Comparison of rates of nosocomial infections in neonatal intensive care units in the united states. national nosocomial infections surveillance system," *Am. J. Med.*, vol. 91, no. 3, pp. 192S–196S, 1991.

[6] D. P. Barker and N. Rutter, "Exposure to invasive procedures in neonatal intensive care unit admissions," *Arch Dis Child Fetal Neonatal Ed*, vol. 72, no. 1, pp. F47–F48, 1995.

[7] P. B. Smith *et al.*, "Is an increased dwell time of a peripherally inserted catheter associated with an increased risk of bloodstream infection in infants?" *Infect. Control Hosp. Epidemiol.*, vol. 29, no. 8, pp. 749–753, 2008.

[8] K. J. Anand, "Clinical importance of pain and stress in preterm neonates," *Biol. Neonate*, vol. 73, no. 1, pp. 1–9, 1998.

[9] S. Goedicke-Fritz *et al.*, "Preterm birth affects the risk of developing immune-mediated diseases," *Frontiers in immunology*, vol. 8, p. 1266, 2017.

[10] P. Cartlidge, P. Fox, and N. Rutter, "The scars of newborn intensive care," *Early human development*, vol. 21, no. 1, pp. 1–10, 1990.

[11] A. Bin Obadi *et al.*, "A Survey on Vital Signs Detection Using Radar Techniques and Processing with FPGA Implementation," *IEEE Circuits Syst. Mag.*, vol. 21, no. 1, pp. 41–74, 2021.

[12] J. Le Kernec *et al.*, "Radar signal processing for sensing in Assisted living," *IEEE Signal Process. Mag.*, no. July, pp. 29–41, 2019.

[13] Y. Zhang, F. Qi, H. Lv, F. Liang, and J. Wang, "Bioradar Technology: Recent Research and Advancements," *IEEE Microw. Mag.*, vol. 20, no. 8, pp. 58–73, aug 2019.

[14] S. M. Islam, O. Boric-Lubecke, V. M. Lubecke, A. K. Moadi, and A. E. Fathy, "Contactless Radar-Based Sensors: Recent Advances in Vital-Signs Monitoring of Multiple Subjects," *IEEE Microw. Mag.*, vol. 23, no. 7, pp. 47–60, 2022.

[15] M. Kebe *et al.*, "Human vital signs detection methods and potential using radars: A review," *Sensors (Switzerland)*, vol. 20, no. 5, 2020.

[16] F. Fioranelli, J. Le Kernec, and S. A. Shah, "Radar for Health Care: Recognizing Human Activities and Monitoring Vital Signs," *IEEE Potentials*, vol. 38, no. 4, pp. 16–23, 2019.

[17] I. J. Brekke, L. H. Puntervoll, P. B. Pedersen, J. Kellett, and M. Brabrand, "The value of vital sign trends in predicting and monitoring clinical deterioration: A systematic review," *PLoS One*, vol. 14, no. 1, pp. 1–13, 2019.

[18] M. Elliott, "The global elements of vital signs assessment: a guide for clinical practice," 2021, (accessed in October, 2022).

[19] L. Tarassenko, A. Hann, and D. Young, "Integrated monitoring and analysis for early warning of patient deterioration," *Br. J. Anaesth.*, vol. 97, no. 1, pp. 64–68, 2006.

[20] M. M. Churpek *et al.*, "Multicenter development and validation of a risk stratification tool for ward patients," *Am. J. Respir. Crit. Care Med.*, vol. 190, no. 6, pp. 649–655, 2014.

[21] S. K. Hung, H. M. Lan, S. T. Han, C. C. Wu, and K. F. Chen, "Current evidence and limitation of biomarkers for detecting sepsis and systemic infection," *Biomedicines*, vol. 8, no. 11, pp. 1–15, 2020.

[22] T. Kenzaka *et al.*, "Importance of vital signs to the early diagnosis and severity of sepsis: Association between vital signs and sequential organ failure assessment score in patients with sepsis," *Intern. Med.*, vol. 51, no. 8, pp. 871–876, 2012.

[23] J. C. A. Martins, H. M. Guedes, C. C. Souza, and T. C. M. Chianca, "Association between vital signs and Manchester Triage System: A retrospective observational study," *Online Brazilian J. Nurs.*, vol. 16, no. 4, pp. 379–388, 2017.

[24] P. Jevon and S. Shamsi, "Using National Early Warning Score (NEWS) 2 to help manage medical emergencies in the dental practice," *Br. Dent. J.*, vol. 229, no. 5, pp. 292–296, 2020.

[25] N. Yanamala *et al.*, "A vital sign-based prediction algorithm for differentiating COVID-19 versus seasonal influenza in hospitalized patients," *npj Digit. Med.*, vol. 4, no. 1, pp. 1–10, 2021.

[26] C. Kitchen, H. Y. Chang, J. P. Weiner, and H. Kharrazi, "Assessing the Added Value of Vital Signs Extracted from Electronic Health Records in Healthcare Risk Adjustment Models," *Risk Manag. Healthc. Policy*, vol. 15, no. September, pp. 1671–1682, 2022.

[27] Merriam-Webster dictionary, "Respiration," (accessed in October, 2022).

[28] A. Albanese, L. Cheng, M. Ursino, and N. W. Chbat, "An integrated mathematical model of the human cardiopulmonary system: model development," *Am. J. Physiol. Circ. Physiol.*, vol. 310, no. 7, pp. H899–H921, 2016.

[29] J. G. Betts *et al.*, "Anatomy and Physiology," 2013, (accessed in October, 2022).

[30] G. Gouna *et al.*, "Positioning effects on lung function and breathing pattern in premature newborns," *J. Pediatr.*, vol. 162, no. 6, pp. 1133–1137.e1, 2013.

[31] C. Wong, C. O. F. Kamlin, J. A. Dawson, C. J. Morley, and P. G. Davis, "Breathing Patterns in Preterm and Term Infants Immediately After Birth," *Pediatr. Res.*, vol. 65, no. 3, pp. 352–356, 2009.

[32] A. Sapra, A. Malik, and P. Bhandari, "Vital sign assessment," *StatPearls*, 2022.

[33] "American Academy of Sleep Medicine (AASM)," (accessed in October, 2022).

[34] A. T. Purnomo, D. B. Lin, T. Adiprabowo, and W. F. Hendria, "Non-contact monitoring and classification of breathing pattern for the supervision of people infected by covid-19," *Sensors*, vol. 21, no. 9, pp. 1–26, 2021.

[35] J. W. Stanifer, "A Peculiar Type of Dyspnea: Kussmaul, Cheyne-Stokes, and Biot Respirations," *Hist. Med.*, vol. 3, no. 1, p. E22, 1946.

[36] A. Fenner, U. Schalk, H. Hoenicke, A. Wendenburg, and T. Roehling, "Periodic breathing in premature and neonatal babies: Incidence, breathing pattern, respiratory gas tensions, response to changes in the composition of ambient air," *Pediatr. Res.*, vol. 7, no. 4, pp. 174–183, 1973.

[37] A. C. Liddle, "Principles of monitoring postoperative patients," *Nurs. Times*, vol. 109, no. 22, pp. 24–26, 2013.

[38] R. R. Mlgaard *et al.*, "Effectiveness of respiratory rates in determining clinical deterioration: a systematic review protocol," *JBI database Syst. Rev. Implement. reports*, vol. 14, no. 7, pp. 19–27, 2016.

[39] M. Elliott, "Why is Respiratory Rate the Neglected Vital Sign? A Narrative Review," *Int. Arch. Nurs. Heal. Care*, vol. 2, no. 3, 2016.

[40] J. F. Fieselmann, M. Hendryx, and C. M. Helms, "Respiratory Rate Predicts Cardiopulmonary Arrest for Internal Medicine lnpatients," *J. Gen. Intern. Med.*, vol. 8, no. 7, pp. 354–360, 1993.

[41] M. A. Cretikos, R. Bellomo, K. Hillman, J. Chen, S. Finfer, and A. Flabouris, "Respiratory rate: The neglected vital sign," *Med. J. Aust.*, vol. 188, no. 11, pp. 657–659, 2008.

[42] E. Vanegas, R. Igual, and I. Plaza, "Sensing systems for respiration monitoring: A technical systematic review," *Sensors (Switzerland)*, vol. 20, no. 18, pp. 1–84, 2020.

[43] L. K. Bawua, C. Miaskowski, X. Hu, G. W. Rodway, and M. M. Pelter, "A review of the literature on the accuracy, strengths, and limitations of visual, thoracic impedance, and electrocardiographic methods used to measure respiratory rate in hospitalized patients," *Ann. Noninvasive Electrocardiol.*, vol. 26, no. 5, pp. 1–14, 2021.

[44] P. H. Charlton *et al.*, "Breathing Rate Estimation From the Electrocardiogram and Photoplethysmogram: A Review," *IEEE Rev Biomed Eng.*, pp. 2–20, 2022.

[45] K. van Loon *et al.*, "Accuracy of remote continuous respiratory rate monitoring technologies intended for low care clinical settings: a prospective observational study," *Can. J. Anesth.*, vol. 65, no. 12, pp. 1324–1332, 2018.

[46] C. Massaroni *et al.*, "Contact-based methods for measuring respiratory rate," *Sensors (Switzerland)*, vol. 19, no. 4, pp. 1–47, 2019.

[47] F. Q. Al-Khalidi, R. Saatchi, D. Burke, H. Elphick, and S. Tan, "Respiration rate monitoring methods: A review," *Pediatr. Pulmonol.*, vol. 46, no. 6, pp. 523–529, 2011.

[48] W. Daw, "Medical Devices for Measuring Respiratory Rate in Children: a Review," *J. Adv. Biomed. Eng. Technol.*, vol. 3, no. 1, pp. 21–27, 2016.

[49] N. Molinaro *et al.*, "Contactless Vital Signs Monitoring From Videos Recorded With Digital Cameras: An Overview," *Front. Physiol.*, vol. 13, 2022.

[50] A. Al-Naji, K. Gibson, S. H. Lee, and J. Chahl, "Monitoring of Cardiorespiratory Signal: Principles of Remote Measurements and Review of Methods," *IEEE Access*, vol. 5, pp. 15 776–15 790, 2017.

[51] O. Alexis, "Providing best practice in manual pulse measurement," *Br. J. Nurs.*, vol. 19, no. 4, pp. 228–234, 2010.

[52] N. De Pinho Ferreira, C. Gehin, and B. Massot, "A Review of Methods for Non-Invasive Heart Rate Measurement on Wrist," *Irbm*, vol. 42, no. 1, pp. 4–18, 2021.

[53] A. Tarniceriu *et al.*, "Towards 24/7 continuous heart rate monitoring," *Proc. Annu. Int. Conf. IEEE Eng. Med. Biol. Soc. EMBS*, vol. 2016-Octob, pp. 186–189, 2016.

[54] J. Kranjec, S. Beguš, G. Geršak, and J. Drnovšek, "Non-contact heart rate and heart rate variability measurements: A review," *Biomed. Signal Process. Control*, vol. 13, no. 1, pp. 102–112, sep 2014.

[55] G. B. Smith, A. Recio-Saucedo, and P. Griffiths, "The measurement frequency and completeness of vital signs in general hospital wards: An evidence free zone?" *Int. J. Nurs. Stud.*, vol. 74, pp. A1–A4, 2017.

[56] J. Gravel, L. Opatrny, and S. Gouin, "High rate of missing vital signs data at triage in a paediatric emergency department," *Paediatr. Child Health (Oxford).*, vol. 11, no. 4, pp. 211–215, 2006.

[57] B. Gary, R. David, and S. William, "A Comparison of the Ability of the Physiologic Components of Medical Emergency Team Criteria and the UK National Early Warning Score," *Critical Care Medicine*, vol. 44, no. 12, pp. 2171–2181, 2016.

[58] H. Hogan *et al.*, "Preventable deaths due to problems in care in English acute hospitals: A retrospective case record review study," *BMJ Qual. Saf.*, vol. 21, no. 9, pp. 737–745, 2012.

[59] C. L. Downey, S. Chapman, R. Randell, J. M. Brown, and D. G. Jayne, "The impact of continuous versus intermittent vital signs monitoring in hospitals: A systematic review and narrative synthesis," *Int. J. Nurs. Stud.*, vol. 84, no. December 2017, pp. 19–27, 2018.

[60] K. Philip, R. Richardson, and M. Cohen, "Staff perceptions of respiratory rate measurement in a general hospital," *Br. J. Nurs.*, vol. 22, no. 10, 2013.

[61] A. S. Poncette *et al.*, "Clinical requirements of future patient monitoring in the intensive care unit: Qualitative study," *JMIR Med. Informatics*, vol. 7, no. 2, 2019.

[62] J. P. Leenen *et al.*, "Current evidence for continuous vital signs monitoring by wearable wireless devices in hospitalized adults: Systematic review," *J. Med. Internet Res.*, vol. 22, no. 6, 2020.

[63] M. Hravnak *et al.*, "Cardiorespiratory instability before and after implementing an integrated monitoring system," *Crit. Care Med.*, vol. 39, no. 1, pp. 65–72, 2011.

[64] S. P. Slight *et al.*, "The return on investment of implementing a continuous monitoring system in general medical-surgical units," *Crit. Care Med.*, vol. 42, no. 8, pp. 1862–1868, 2014.

[65] E. A. Ochroch *et al.*, "The impact of continuous pulse oximetry monitoring on intensive care unit admissions from a postsurgical care floor," *Anesth. Analg.*, vol. 102, no. 3, pp. 868–875, 2006.

[66] J. Morgan, S. McGrath, and G. Blike, "Cost Effectiveness of Patient Surveillance Systems," *Proceeding from Int. Anesth. Res. Soc. Annu. Meet.*, no. 249, pp. 5–6, 2010.

[67] P. C. Dykes *et al.*, "Reducing ICU Utilization, Length of Stay, and Cost by Optimizing the Clinical Use of Continuous Monitoring System Technology in the Hospital," *Am. J. Med.*, vol. 135, no. 3, pp. 337–341.e1, 2022.

[68] T. C. Asogwa, E. Fidelis, C. Obodoeze, and I. N. Obiokafor, "NMF and its Interdisciplinary Applications: A Review," *Int. J. Adv. Res. Comput. Commun. Eng. ISO*, vol. 3297, no. 4, pp. 67–72, 2007.

[69] C. R. Ratliff, "Descriptive study of the frequency of medical adhesive related skin injuries in a vascular clinic," *J. Vasc. Nurs.*, vol. 35, no. 2, pp. 86–89, 2017.

[70] C. Konya *et al.*, "Skin injuries caused by medical adhesive tape in older people and associated factors," *J. Clin. Nurs.*, vol. 19, no. 9-10, pp. 1236–1242, 2010.

[71] C. H. Lund *et al.*, "Neonatal skin care: clinical outcomes of the AWHONN/NANN evidence-based clinical practice guideline," *J. Obstet. Gynecol. Neonatal Nurs.*, vol. 30, no. 1, pp. 41–51, 2001.

[72] S. Xu *et al.*, "Wireless skin sensors for physiological monitoring of infants in low-income and middle-income countries," *Lancet Digit. Heal.*, vol. 3, no. 4, pp. e266–e273, 2021.

[73] C. Lund, "Medical Adhesives in the NICU," *Newborn Infant Nurs. Rev.*, vol. 14, no. 4, pp. 160–165, 2014.

[74] A. Conde-Agudelo and J. L. Díaz-Rossello, "Kangaroo mother care to reduce morbidity and mortality in low birthweight infants," *Cochrane Database Syst. Rev.*, vol. 2016, no. 8, 2016.

[75] J. C. Lin, "Noninvasive microwave measurement of respiration," *Proceedings of the IEEE*, vol. 63, no. 10, pp. 1530–1530, 1975.

[76] S. A. Shah and F. Fioranelli, "RF Sensing Technologies for Assisted Daily Living in Healthcare: A Comprehensive Review," *IEEE Aerosp. Electron. Syst. Mag.*, vol. 34, no. 11, pp. 26–44, 2019.

[77] K.-m. Chen, D. Misra, H. Wang, H.-r. Chuang, and E. Postow, "An X-Band Microwave Life-Detection System," *IEEE Trans. Biomed. Eng.*, vol. 33, no. 7, pp. 697–701, 1986.

[78] C. Li, V. M. Lubecke, O. Boric-Lubecke, and J. Lin, "A Review on Recent Advances in Doppler Radar Sensors for Noncontact Healthcare Monitoring," *IEEE Trans. Microw. Theory Tech.*, vol. 61, no. 5, pp. 2046–2060, 2013.

[79] Z. Liu, X. Liu, J. Zhang, and K. Li, "Opportunities and Challenges of Wireless Human Sensing for the Smart IoT World: A Survey," *IEEE Netw.*, vol. 33, no. 5, pp. 104–110, 2019.

[80] J. Liu, H. Liu, Y. Chen, Y. Wang, and C. Wang, "Wireless Sensing for Human Activity: A Survey," *IEEE Commun. Surv. Tutorials*, vol. 22, no. 3, pp. 1629–1645, 2020.

[81] L. Bernardi, C. Porta, A. Gabutti, L. Spicuzza, and P. Sleight, "Modulatory effects of respiration," *Auton. Neurosci. Basic Clin.*, vol. 90, no. 1-2, pp. 47–56, 2001.

[82] V. Selvaraju *et al.*, "Continuous Monitoring of Vital Signs Using Cameras: A Systematic Review," *Sensors*, vol. 22, no. 11, 2022.

[83] I. Lorato, S. Stuijk, M. Meftah, D. Kommers, P. Andriessen, C. van Pul, and G. de Haan, "Towards continuous camera-based respiration monitoring in infants," *Sensors*, vol. 21, no. 7, pp. 1–18, 2021.

[84] M. Villarroel *et al.*, "Non-contact physiological monitoring of preterm infants in the Neonatal Intensive Care Unit," *npj Digit. Med.*, vol. 2, no. 1, pp. 1–18, 2019.

[85] F. T. Z. Khanam, A. Al-Naji, and J. Chahl, "Remote monitoring of vital signs in diverse non-clinical and clinical scenarios using computer vision systems: A review," *Appl. Sci.*, vol. 9, no. 20, 2019.

[86] D. McDuff, "Camera measurement of physiological vital signs," *ACM Comput. Surv.*, vol. 55, no. 9, 2023.

[87] M. Harford, J. Catherall, S. Gerry, J. D. Young, and P. Watkinson, "Availability and performance of image-based, non-contact methods of monitoring heart rate, blood pressure, respiratory rate, and oxygen saturation: a systematic review," *Physiol. Meas.*, vol. 40, no. 6, 2019.

[88] J.-C. Cobos-Torres, M. Abderrahim, and J. Martínez-Orgado, "Non-Contact, Simple Neonatal Monitoring by Photoplethysmography," *Sensors*, vol. 18, no. 12, p. 4362, dec 2018.

[89] M. Zakrzewski, A. Vehkaoja, A. S. Joutsen, K. T. Palovuori, and J. J. Vanhala, "Noncontact Respiration Monitoring During Sleep With Microwave Doppler Radar," *IEEE Sens. J.*, vol. 15, no. 10, pp. 5683–5693, oct 2015.

[90] J. Li, L. Liu, Z. Zeng, and F. Liu, "Advanced Signal Processing for Vital Sign Extraction With Applications in UWB Radar Detection of Trapped Victims in Complex Environments," *IEEE J. Sel. Top. Appl. Earth Obs. Remote Sens.*, vol. 7, no. 3, pp. 783–791, 2014.

[91] F. Fioranelli *et al.*, "Radar sensing for healthcare," *Electron. Lett.*, vol. 55, no. 19, pp. 1022–1024, 2019.

[92] Wei Hu, Zhangyan Zhao, Yunfeng Wang, Haiying Zhang, and Fujiang Lin, "Noncontact Accurate Measurement of Cardiopulmonary Activity Using a Compact Quadrature Doppler Radar Sensor," *IEEE Trans. Biomed. Eng.*, vol. 61, no. 3, pp. 725–735, mar 2014.

[93] M. Mercuri *et al.*, "Vital-sign monitoring and spatial tracking of multiple people using a contactless radar-based sensor," *Nat. Electron.*, vol. 2, no. 6, pp. 252–262, 2019.

[94] W. H. Lee *et al.*, "Feasibility of non-contact cardiorespiratory monitoring using impulse-radio ultra-wideband radar in the neonatal intensive care unit," *PLoS One*, vol. 15, no. 12, pp. 1–15, 2021.

[95] C. Li, "Vital-sign monitoring on the go," *Nat. Electron.*, vol. 2, no. 6, pp. 219–220, 2019.

[96] U. Frey, M. Silverman, A. L. Barabási, and B. Suki, "Irregularities and power law distributions in the breathing pattern in preterm and term infants," *J. Appl. Physiol.*, vol. 85, no. 3, pp. 789–797, 1998.

[97] U. Karahasanovic, T. Stifter, H.-P. Beise, A. Fox, and D. Tatarinov, "Mathematical Modelling and Simulations of Complex Breathing Patterns Detected by RADAR Sensors," in *2018 19th Int. Radar Symp.*, 2018, pp. 1–10.

[98] J. Tu, T. Hwang, and J. Lin, "Respiration Rate Measurement Under 1-D Body Motion Using Single Continuous-Wave Doppler Radar Vital Sign Detection System," *IEEE Trans. Microw. Theory Tech.*, vol. 64, no. 6, pp. 1937–1946, 2016.

[99] Y. Rong and D. W. Bliss, "Remote Sensing for Vital Information Based on Spectral-Domain Harmonic Signatures," *IEEE Trans. Aerosp. Electron. Syst.*, vol. 55, no. 6, pp. 3454–3465, 2019.

[100] J. Geisheimer and E. F. Greneker, "A non-contact lie detector using radar vital signs monitor (RVSM) technology," *IEEE Aerosp. Electron. Syst. Mag.*, vol. 16, no. 8, pp. 10–14, 2001.

[101] M. Czerkawski *et al.*, "On Models and Approaches for Human Vital Signs Extraction from Short Range Radar Signals," *14th Eur. Conf. Antennas Propagation, EuCAP 2020*, pp. 0–4, 2020.

[102] A. De Groote, M. Wantier, G. Cheron, M. Estenne, and M. Paiva, "Chest wall motion during tidal breathing," *J. Appl. Physiol.*, vol. 83, no. 5, pp. 1531–1537, nov 1997.

[103] F. Quaiyum *et al.*, "Electromagnetic Modeling of Vital Sign Detection and Human Motion Sensing Validated by Noncontact Radar Measurements," *IEEE J. Electromagn. RF Microwaves Med. Biol.*, vol. 2, no. 1, pp. 40–47, 2018.

[104] M. Nosrati and N. Tavassolian, "High-Accuracy Heart Rate Variability Monitoring Using Doppler Radar Based on Gaussian Pulse Train Modeling and FTPR Algorithm," *IEEE Trans. Microw. Theory Tech.*, vol. 66, no. 1, pp. 556–567, 2018.

[105] D. R. Morgan and M. G. Zierdt, "Novel signal processing techniques for Doppler radar cardiopulmonary sensing," *Signal Processing*, vol. 89, no. 1, pp. 45–66, 2009.

[106] C. Yang, S. Tang, and N. Tavassolian, "Utilizing Gyroscopes Towards the Automatic Annotation of Seismocardiograms," *IEEE Sens. J.*, vol. 17, no. 7, pp. 2129–2136, 2017.

[107] M. Nosrati and N. Tavassolian, "Accurate Doppler Radar-Based Cardiopulmonary Sensing Using Chest-Wall Acceleration," *IEEE J. Electromagn. RF Microwaves Med. Biol.*, vol. 3, no. 1, pp. 41–47, 2019.

[108] K. Kishimoto, S. Yonezawa, N. Shiraki, D. Sasakawa, and N. Honma, "Evaluation of vital sign distribution using array antenna," *2017 Int. Symp. Antennas Propagation, ISAP 2017*, vol. 2017-Janua, no. c, pp. 1–2, 2017.

[109] Ø. Aardal, S. E. Hamran, T. Berger, J. Hammerstad, and T. S. Lande, "Radar cross section of the human heartbeat and respiration in the 500MHz to 3GHz band," *IEEE Radio Wirel. Week*, pp. 422–425, 2011.

[110] A. Singh, S. U. Rehman, S. Yongchareon, and P. H. J. Chong, "Multi-Resident Non-Contact Vital Sign Monitoring Using Radar: A Review," *IEEE Sens. J.*, vol. 21, no. 4, pp. 4061–4084, 2021.

[111] C. Li *et al.*, "A Review on Recent Progress of Portable Short-Range Noncontact Microwave Radar Systems," *IEEE Trans. Microw. Theory Tech.*, vol. 65, no. 5, pp. 1692–1706, 2017.

[112] G. Beltrão, M. Alaee-Kerahroodi, U. Schroeder, M. R. B. Shankar, G. Beltrao, M. Alaee-Kerahroodi, U. Schroder, and S. M. Bhavani, "Joint Waveform/Receiver Design for Vital-Sign Detection in Signal-Dependent Interference," in *IEEE Radar Conf.*, 2020, pp. 1–6.

[113] J.-M. Munoz-Ferreras, Z. Peng, R. Gomez-Garcia, and C. Li, "Review on Advanced Short-Range Multimode Continuous-Wave Radar Architectures for Healthcare Applications," *IEEE J. Electromagn. RF Microwaves Med. Biol.*, vol. 1, no. 1, pp. 14–25, 2017.

[114] Texas Instruments, "mmWave radar sensors," (accessed October, 2022).

[115] Infineon, "Radar sensors," (accessed October, 2022).

[116] Changzhi Li and Jenshan Lin, "Random Body Movement Cancellation in Doppler Radar Vital Sign Detection," *IEEE Trans. Microw. Theory Tech.*, vol. 56, no. 12, pp. 3143–3152, 2008.

[117] B.-K. Park, O. Boric-Lubecke, and V. M. Lubecke, "Arctangent Demodulation With DC Offset Compensation in Quadrature Doppler Radar Receiver Systems," *IEEE Trans. Microw. Theory Tech.*, vol. 55, no. 5, pp. 1073–1079, 2007.

[118] C. Li and J. Lin, "Complex signal demodulation and random body movement cancellation techniques for non-contact vital sign detection," *IEEE MTT-S Int. Microw. Symp. Dig.*, pp. 567–570, 2008.

[119] M. Zakrzewski, H. Raittinen, and J. Vanhala, "Comparison of center estimation algorithms for heart and respiration monitoring with microwave doppler radar," *IEEE Sens. J.*, vol. 12, no. 3, pp. 627–634, 2012.

[120] J. Wang, X. Wang, L. Chen, J. Huangfu, C. Li, and L. Ran, "Noncontact distance and amplitude-independent vibration measurement based on an extended dacm algorithm," *IEEE Trans. Instrum. Meas.*, vol. 63, no. 1, pp. 145–153, 2014.

[121] S. Guan, J. A. Rice, C. Li, and C. Gu, "Automated DC offset calibration strategy for structural health monitoring based on portable CW radar sensor," *IEEE Trans. Instrum. Meas.*, vol. 63, no. 12, pp. 3111–3118, 2014.

[122] G. Beltrão, M. Alaee-Kerahroodi, U. Schroeder, D. Tatarinov, and M. R. Bhavani Shankar, "Statistical Performance Analysis of Radar-Based Vital-Sign Processing Techniques," in *Sensing Technology.* Springer International Publishing, 2022, pp. 101–112.

[123] C. Li, J. Cummings, J. Lam, E. Graves, and W. Wu, "Radar Remote Monitoring of Vital Signs," *IEEE Microw. Mag.*, vol. 10, no. 1, pp. 47–56, 2009.

[124] Q. Lv *et al.*, "Doppler Vital Signs Detection in the Presence of Large-Scale Random Body Movements," *IEEE Trans. Microw. Theory Tech.*, vol. 66, no. 9, pp. 4261–4270, 2018.

[125] J. D. Kim, W. H. Lee, Y. Lee, H. J. Lee, T. Cha, S. H. Kim, K. M. Song, Y. H. Lim, S. H. Cho, S. H. Cho, and H. K. Park, "Non-contact respiration monitoring using impulse radio ultrawideband radar in neonates," *R. Soc. Open Sci.*, vol. 6, no. 6, 2019.

[126] J.-Y. Park *et al.*, "Preclinical evaluation of noncontact vital signs monitoring using real-time IR-UWB radar and factors affecting its accuracy," *Sci. Rep.*, vol. 11, no. 1, pp. 1–12, 2021.

[127] F. Adib, H. Mao, Z. Kabelac, D. Katabi, and R. C. Miller, "Smart homes that monitor breathing and heart rate," *Conf. Hum. Factors Comput. Syst. - Proc.*, vol. 2015-April, pp. 837–846, 2015.

[128] F. Khan and S. H. Cho, "A detailed algorithm for vital sign monitoring of a stationary/non-stationary human through IR-UWB radar," *Sensors (Switzerland)*, vol. 17, no. 2, 2017.

[129] W. Xia, Y. Li, and S. Dong, "Radar-Based High-Accuracy Cardiac Activity Sensing," *IEEE Trans. Instrum. Meas.*, vol. 70, 2021.

[130] W. Ren *et al.*, "Vital sign detection in any orientation using a distributed radar network via modified independent component analysis," *IEEE Trans. Microw. Theory Tech.*, vol. 69, no. 11, pp. 4774–4790, 2021.

[131] F. Weishaupt, I. Walterscheid, O. Biallawons, and J. Klare, "Vital sign localization and measurement using an LFMCW MIMO radar," *Proc. Int. Radar Symp.*, vol. 2018-June, pp. 1–8, 2018.

[132] L. Sun *et al.*, "Remote Measurement of Human Vital Signs Based on Joint-Range Adaptive EEMD," *IEEE Access*, vol. 8, pp. 68 514–68 524, 2020.

[133] W. Lv, W. He, X. Lin, and J. Miao, "Non-Contact Monitoring of Human Vital Signs Using FMCW Millimeter Wave Radar in the 120 GHz Band," *Sensors*, vol. 21, no. 8, p. 2732, 2021.

[134] H. Shen *et al.*, "Respiration and Heartbeat Rates Measurement Based on Autocorrelation Using IR-UWB Radar," *IEEE Trans. Circuits Syst. II Express Briefs*, vol. 65, no. 10, pp. 1470–1474, 2018.

[135] C. Ye, K. Toyoda, and T. Ohtsuki, "Blind Source Separation on Non-Contact Heartbeat Detection by Non-Negative Matrix Factorization Algorithms," *IEEE Trans. Biomed. Eng.*, vol. 67, no. 2, pp. 482–494, 2020.

[136] M. He, Y. Nian, L. Xu, L. Qiao, and W. Wang, "Adaptive Separation of Respiratory and Heartbeat Signals among Multiple People Based on Empirical Wavelet Transform Using UWB Radar," *Sensors*, vol. 20, no. 17, p. 4913, 2020.

[137] S. Kim and K. K. Lee, "Low-Complexity Joint Extrapolation-MUSIC-Based 2-D Parameter Estimator for Vital FMCW Radar," *IEEE Sens. J.*, vol. 19, no. 6, pp. 2205–2216, 2019.

[138] W. Zhang, G. Li, Z. Wang, and H. Wu, "Non-contact monitoring of human heartbeat signals using mm-wave frequency-modulated continuous-wave radar under low signal-to-noise ratio conditions," *IET Radar, Sonar Navig.*, vol. 16, no. 3, pp. 456–469, 2022.

[139] E. Conte, A. Filippi, and S. Tomasin, "ML period estimation with application to vital sign monitoring," *IEEE Signal Process. Lett.*, vol. 17, no. 11, pp. 905–908, 2010.

[140] N. Regev and D. Wulich, "Radar-based, simultaneous human presence detection and breathing rate estimation," *Sensors*, vol. 21, no. 10, 2021.

[141] M. Arsalan, A. Santra, and C. Will, "Improved Contactless Heartbeat Estimation in FMCW Radar via Kalman Filter Tracking," *IEEE Sensors Lett.*, vol. 4, no. 5, pp. 1–4, 2020.

[142] E. M. Wong, F. Tablin, and E. S. Schelegle, "Comparison of nonparametric and parametric methods for time-frequency heart rate variability analysis in a rodent model of cardiovascular disease," *PLoS One*, vol. 15, no. 11, pp. 1–15, 2020.

[143] S. Chen, X. Dong, G. Xing, Z. Peng, W. Zhang, and G. Meng, "Separation of Overlapped Non-Stationary Signals by Ridge Path Regrouping and Intrinsic Chirp Component Decomposition," *IEEE Sens. J.*, vol. 17, no. 18, pp. 5994–6005, 2017.

[144] R. Qian, T. Jin, H. Li, and Y. Dai, "WT-Based Data-Length-Variation Technique for Fast Heart Rate Detection," in *2018 Prog. Electromagn. Res. Symp.*, vol. 66, no. 1. IEEE, 2018, pp. 399–404.

[145] V. L. Petrovic *et al.*, "High-Accuracy Real-Time Monitoring of Heart Rate Variability Using 24 GHz Continuous-Wave Doppler Radar," *IEEE Access*, vol. 7, pp. 74 721–74 733, 2019.

[146] M. Le and B. Van Nguyen, "Multivariate Correlation of Higher Harmonics for Heart Rate Remote Measurement Using UWB Impulse Radar," *IEEE Sens. J.*, vol. 20, no. 4, pp. 1859–1866, 2020.

[147] M. Alizadeh, G. Shaker, J. C. M. D. Almeida, P. P. Morita, and S. Safavi-Naeini, "Remote Monitoring of Human Vital Signs Using mm-Wave FMCW Radar," *IEEE Access*, vol. 7, no. 4, pp. 54 958–54 968, 2019.

[148] J. Y. Shih and F. K. Wang, "Quadrature Cosine Transform (QCT) With Varying Window Length (VWL) Technique for Noncontact Vital Sign Monitoring Using a Continuous-Wave (CW) Radar," *IEEE Trans. Microw. Theory Tech.*, pp. 1–12, 2021.

[149] H. Lee, B. H. Kim, J. K. Park, S. W. Kim, and J. G. Yook, "A Resolution Enhancement Technique for Remote Monitoring of the Vital Signs of Multiple Subjects Using a 24 GHz Bandwidth-Limited FMCW Radar," *IEEE Access*, vol. 8, pp. 1240–1248, 2019.

[150] Texas Instruments, "TI AWR1642," (accessed October, 2022).

[151] *optoNCDT laser sensor*, (accessed October, 2022).

[152] A. R. Diewald *et al.*, "RF-based child occupation detection in the vehicle interior," *Proc. Int. Radar Symp.*, vol. 2016-June, pp. 1–4, 2016.

[153] "Hexoskin," (accessed October, 2022).

[154] R. Villar, T. Beltrame, and R. L. Hughson, "Validation of the Hexoskin wearable vest during lying, sitting, standing, and walking activities," *Appl. Physiol. Nutr. Metab.*, vol. 40, no. 10, pp. 1019–1024, 2015.

[155] G. Beltrão *et al.*, "Nonlinear Least Squares Estimation for Breathing Monitoring Using FMCW Radars," in *2021 18th Eur. Radar Conf.*, 2022, pp. 241–244.

[156] J. K. Park, Y. Hong, H. Lee, C. Jang, G. H. Yun, H. J. Lee, and J. G. Yook, "Noncontact RF Vital Sign Sensor for Continuous Monitoring of Driver Status," *IEEE Trans. Biomed. Circuits Syst.*, vol. 13, no. 3, pp. 493–502, 2019.

[157] A. Ahmad, J. C. Roh, D. Wang, and A. Dubey, "Vital signs monitoring of multiple people using a FMCW millimeter-wave sensor," in *2018 IEEE Radar Conf.*, no. 4. IEEE, 2018, pp. 1450–1455.

[158] C. Li, J. Ling, J. Li, and J. Lin, "Accurate doppler radar noncontact vital sign detection using the RELAX algorithm," *IEEE Trans. Instrum. Meas.*, vol. 59, no. 3, pp. 687–695, 2010.

[159] G. Beltrão *et al.*, "Contactless radar-based breathing monitoring of premature infants in the neonatal intensive care unit," *Sci. Rep.*, vol. 12, no. 1, pp. 1–15, 2022.

[160] T. Sakamoto *et al.*, "Feature-based Correlation and Topological Similarity for Interbeat Interval Estimation using Ultra-Wideband Radar," *IEEE Trans. Biomed. Eng.*, vol. 63, no. 4, pp. 1–1, 2015.

[161] A. Bhandari, F. Krahmer, and R. Raskar, "On unlimited sampling," *2017 12th Int. Conf. Sampl. Theory Appl. SampTA 2017*, pp. 31–35, 2017.

[162] ——, "On Unlimited Sampling and Reconstruction," *IEEE Trans. Signal Process.*, vol. 69, pp. 3827–3839, 2021.

[163] ——, "Unlimited Sampling of Sparse Signals," *ICASSP, IEEE Int. Conf. Acoust. Speech Signal Process. - Proc.*, pp. 4569–4573, 2018.

[164] K. Naishadham, J. E. Piou, L. Ren, and A. E. Fathy, "Estimation of Cardiopulmonary Parameters From Ultra Wideband Radar Measurements Using the State Space Method," *IEEE Trans. Biomed. Circuits Syst.*, vol. 10, no. 6, pp. 1037–1046, 2016.

[165] M. Mercuri *et al.*, "Enabling Robust Radar-Based Localization and Vital Signs Monitoring in Multipath Propagation Environments," *IEEE Trans. Biomed. Eng.*, vol. 68, no. 11, pp. 3228–3240, 2021.

[166] K. Itoh, "Analysis of the phase unwrapping algorithm," *Appl. Opt.*, vol. 21, no. 14, p. 2470, 1982.

[167] A. Bhandari, F. Krahmer, and T. Poskitt, "Unlimited Sampling from Theory to Practice: Fourier-Prony Recovery and Prototype ADC," *IEEE Trans. Signal Process.*, vol. 70, pp. 1131–1141, 2022.

[168] D. Florescu, F. Krahmer, and A. Bhandari, "The Surprising Benefits of Hysteresis in Unlimited Sampling: Theory, Algorithms and Experiments," *IEEE Trans. Signal Process.*, vol. 70, pp. 616–630, 2022.

[169] T. Feuillen, M. Alaee-Kerahroodi, A. Bhandari, B. S. M. R, and B. Ottersten, "Unlimited Sampling for FMCW Radars: A Proof of Concept," in *2022 IEEE Radar Conf.* IEEE, mar 2022, pp. 1–5.

[170] C. P. Howson *et al.*, "Born too soon: Preterm birth matters," *Reproductive Health*, vol. 10, no. 1, p. S1, 2015.

[171] E. Bancalari and N. Claure, "Definitions and diagnostic criteria for bronchopulmonary dysplasia," in *Seminars in perinatology*, vol. 30, no. 4. Elsevier, 2006, pp. 164–170.

[172] H. Verder, K. Bohlin, J. Kamper, R. Lindwall, and B. Jonsson, "Nasal cpap and surfactant for treatment of respiratory distress syndrome and prevention of bronchopulmonary dysplasia," *Acta paediatrica*, vol. 98, no. 9, pp. 1400–1408, 2009.

[173] J. Zhao, F. Gonzalez, and D. Mu, "Apnea of prematurity: from cause to treatment," *European journal of pediatrics*, vol. 170, no. 9, pp. 1097–1105, 2011.

[174] A. Nuytten *et al.*, "Postnatal corticosteroids policy for very preterm infants and bronchopulmonary dysplasia," *Neonatology*, vol. 117, no. 3, pp. 308–315, 2020.

[175] H. U. Chung *et al.*, "Binodal, wireless epidermal electronic systems with in-sensor analytics for neonatal intensive care," *Science*, vol. 363, no. 6430, 2019.

[176] ——, "Skin-interfaced biosensors for advanced wireless physiological monitoring in neonatal and pediatric intensive-care units," *Nature Medicine*, vol. 26, no. 3, pp. 418–429, 2020.

[177] J. Steinbach *et al.*, "Bedside measurement of volatile organic compounds in the atmosphere of neonatal incubators using ion mobility spectrometry," *Frontiers in pediatrics*, vol. 7, p. 248, 2019.

[178] T. Rogosch *et al.*, "Detection of bloodstream infections and prediction of bronchopulmonary dysplasia in preterm neonates with an electronic nose," *The Journal of pediatrics*, vol. 165, no. 3, pp. 622–624, 2014.

[179] N. H. Gangaram-Panday *et al.*, "Dynamic light scattering: A new noninvasive technology for neonatal heart rate monitoring," *Neonatology*, vol. 117, no. 3, pp. 279–286, 2020.

[180] J. Allen, "Photoplethysmography and its application in clinical physiological measurement," *Physiological measurement*, vol. 28, no. 3, p. R1, 2007.

[181] J.-C. Cobos-Torres, M. Abderrahim, and J. Martínez-Orgado, "Non-contact, simple neonatal monitoring by photoplethysmography," *Sensors*, vol. 18, no. 12, p. 4362, 2018.

[182] C. F. Poets, "Apnea of prematurity: What can observational studies tell us about pathophysiology?" *Sleep medicine*, vol. 11, no. 7, pp. 701–707, 2010.

[183] C. F. Poets *et al.*, "Association between intermittent hypoxemia or bradycardia and late death or disability in extremely preterm infants," *Jama*, vol. 314, no. 6, pp. 595–603, 2015.

[184] C. B. Pereira *et al.*, "Noncontact monitoring of respiratory rate in newborn infants using thermal imaging," *IEEE Transactions on Biomedical Engineering*, vol. 66, no. 4, pp. 1105–1114, 2019.

[185] A. K. Abbas, K. Heimann, K. Jergus, T. Orlikowsky, and S. Leonhardt, "Neonatal non-contact respiratory monitoring based on real-time infrared thermography," *Biomedical engineering online*, vol. 10, no. 1, pp. 1–17, 2011.

[186] S. A. Pullano *et al.*, "Medical devices for pediatric apnea monitoring and therapy: Past and new trends," *IEEE Reviews in Biomedical Engineering*, vol. 10, pp. 199–212, 2017.

[187] S. Fleming *et al.*, "Normal ranges of heart rate and respiratory rate in children from birth to 18 years of age: A systematic review of observational studies," *Lancet*, vol. 377, no. 9770, pp. 1011–1018, 2011.

[188] K. M. Hayward *et al.*, "Effect of cobedding twins on coregulation, infant state, and twin safety," *Journal of Obstetric, Gynecologic, & Neonatal Nursing*, vol. 44, no. 2, pp. 193–202, 2015.

[189] Z. Badiee, Z. Nassiri, and A. Armanian, "Cobedding of twin premature infants: Calming effects on pain responses," *Pediatrics & Neonatology*, vol. 55, no. 4, pp. 262–268, 2014.

[190] M. Patel *et al.*, "Clinical associations with immature breathing in preterm infants: part 2—periodic breathing," *Pediatric research*, vol. 80, no. 1, pp. 28–34, 2016.

[191] M. A. Mohr *et al.*, "Quantification of periodic breathing in premature infants," *Physiological measurement*, vol. 36, no. 7, p. 1415, 2015.

[192] Z. Weintraub *et al.*, "The morphology of periodic breathing in infants and adults," *Respiration physiology*, vol. 127, no. 2-3, pp. 173–184, 2001.

[193] G. Shafiq and K. C. Veluvolu, "Surface chest motion decomposition for cardiovascular monitoring," *Sci. Rep.*, vol. 4, pp. 1–9, 2014.

[194] X. Yu, C. Li, and J. Lin, "Two-dimensional noncontact vital sign detection using Doppler radar array approach," *IEEE MTT-S Int. Microw. Symp. Dig.*, pp. 1–4, 2011.

[195] J. M. Munoz-Ferreras, Z. Peng, R. Gomez-Garcia, and C. Li, "Random body movement mitigation for FMCW-radar-based vital-sign monitoring," *Proceedings of BioWireleSS 2016*, pp. 22–24, 2016.

[196] D. D. Lee and H. S. Seung, "Learning the Parts of Objects by NNMF," *Nature*, vol. 401, no. October 1999, pp. 788–791, 1999.

[197] M. W. Berry, M. Browne, A. N. Langville, V. P. Pauca, and R. J. Plemmons, "Algorithms and applications for approximate nonnegative matrix factorization," *Comput. Stat. Data Anal.*, vol. 52, no. 1, pp. 155–173, 2007.

[198] P. Stoica *et al.*, *Spectral analysis of signals*. Pearson Prentice Hall Upper Saddle River, NJ, 2005.

[199] M. G. Christensen and A. Jakobsson, *Multi-pitch estimation*. Morgan & Claypool Publishers, 2009.

[200] B. Lohman *et al.*, "A Digital Signal Processor for Doppler Radar Sensing of Vital Signs," *IEEE Engineering in Medicine and Biology Magazine*, vol. 21, no. 5, pp. 3359–3362, 2002.

[201] J. Wei, L. Zhang, and H. Liu, "Non-Contact Life Signal Extraction and Reconstruction Technique Based on MAE," *IEEE Access*, vol. 7, pp. 110 826–110 834, 2019.

[202] M. G. Christensen, P. Stoica, A. Jakobsson, and S. Holdt Jensen, "Multi-pitch estimation," *Signal Processing*, vol. 88, no. 4, pp. 972–983, 2008.

[203] *MATLAB*, (accessed in October, 2022).

[204] S. Bakhtiari, S. Liao, T. Elmer, N. S. Gopalsami, and A. C. Raptis, "A real-time heart rate analysis for a remote millimeter wave I-Q sensor," *IEEE Trans. Biomed. Eng.*, vol. 58, no. 6, pp. 1839–1845, 2011.

[205] P. Larsen and T. Mousel, "Radio-Frequency Based Detection of Unattended Children to Reduce In-Vehicle Heat Stroke Fatalities," *IRC-17-58 IRCOBI Conf. 2017*, pp. 220–233, 2017.

[206] *Vitaguard*, (accessed in October, 2022).

[207] *Electrodes*, (accessed in October, 2022).

[208] W. Verhelst, "Overlap-add methods for time-scaling of speech," *Speech Commun.*, vol. 30, no. 4, pp. 207–221, 2000.

[209] P. Magron, R. Badeau, and B. David, "Model-Based STFT Phase Recovery for Audio Source Separation," *IEEE/ACM Trans. Audio Speech Lang. Process.*, vol. 26, no. 6, pp. 1091–1101, 2018.

[210] G. Wang, C. Gu, T. Inoue, and C. Li, "A Hybrid FMCW-Interferometry Radar for Indoor Precise Positioning and Versatile Life Activity Monitoring," *IEEE Trans. Microw. Theory Tech.*, vol. 62, no. 11, pp. 2812–2822, 2014.

[211] J. Yan *et al.*, "Phase-Based Human Target 2-D Identification With a Mobile FMCW Radar Platform," *IEEE Trans. Microw. Theory Tech.*, vol. 67, no. 12, pp. 5348–5359, 2019.

[212] C. Li, Y. Xiao, and J. Lin, "Experiment and Spectral Analysis of a Low-Power Ka-Band Heartbeat Detector Measuring From Four Sides of a Human Body," *IEEE Trans. Microw. Theory Tech.*, vol. 54, no. 12, pp. 4464–4471, 2006.

[213] K.-K. Shyu, L.-J. Chiu, P.-L. Lee, T.-H. Tung, and S.-H. Yang, "Detection of Breathing and Heart Rates in UWB Radar Sensor Data Using FVPIEF-Based Two-Layer EEMD," *IEEE Sens. J.*, vol. 19, no. 2, pp. 774–784, 2019.

[214] G. Singh, A. Tee, T. Trakoolwilaiwan, A. Taha, and M. Olivo, "Method of respiratory rate measurement using a unique wearable platform and an adaptive optical-based approach," *Intensive Care Med. Exp.*, vol. 8, no. 1, pp. 0–9, 2020.

[215] A. Droitcour, O. Boric-Lubecke, V. Lubecke, J. Lin, and G. Kovacs, "Range Correlation and IQ Performance Benefits in Single-Chip Silicon Doppler Radars for Noncontact Cardiopulmonary Monitoring," *IEEE Trans. Microw. Theory Tech.*, vol. 52, no. 3, pp. 838–848, 2004.

[216] J. Tu and J. Lin, "Respiration harmonics cancellation for Accurate Heart Rate measurement in non-contact vital sign detection," in *2013 IEEE MTT-S Int. Microw. Symp. Dig.* IEEE, 2013, pp. 1–3.

[217] ——, "Fast Acquisition of Heart Rate in Noncontact Vital Sign Radar Measurement Using Time-Window-Variation Technique," *IEEE Trans. Instrum. Meas.*, vol. 65, no. 1, pp. 112–122, 2016.

[218] M. Zakrzewski *et al.*, "Quadrature Imbalance Compensation With Ellipse-Fitting Methods for Microwave Radar Physiological Sensing," *IEEE Trans. Microw. Theory Tech.*, vol. 62, no. 6, pp. 1400–1408, 2014.

[219] L. Ren, H. Wang, K. Naishadham, O. Kilic, and A. E. Fathy, "Phase-Based Methods for Heart Rate Detection Using UWB Impulse Doppler Radar," *IEEE Trans. Microw. Theory Tech.*, vol. 64, no. 10, pp. 3319–3331, 2016.

[220] A. I. Aladin *et al.*, "Relation of Resting Heart Rate to Risk for All-Cause Mortality by Gender After considering Exercise Capacity," *Am. J. Cardiol.*, vol. 114, no. 11, pp. 1701–1706, 2014.

[221] F. Scholkmann and U. Wolf, "The Pulse-Respiration Quotient: A Powerful but Untapped Parameter for Modern Studies About Human Physiology and Pathophysiology," *Front. Physiol.*, vol. 10, no. APR, pp. 1–18, 2019.

[222] F. Scholkmann, H. Zohdi, and U. Wolf, "The Resting-State Pulse-Respiration Quotient of Humans: Lognormally Distributed and Centered Around a Value of Four," *Physiol. Res.*, vol. 68, no. 6, pp. 1027–1032, 2019.

[223] J. Montes, J. C. Young, R. Tandy, and J. W. Navalta, "Reliability and Validation of the Hexoskin Wearable Bio-Collection Device During Walking Conditions." *Int. J. Exerc. Sci.*, vol. 11, no. 7, pp. 806–816, 2018.

[224] Z.-K. Yang, H. Shi, S. Zhao, and X.-D. Huang, "Vital Sign Detection during Large-Scale and Fast Body Movements Based on an Adaptive Noise Cancellation Algorithm Using a Single Doppler Radar Sensor," *Sensors*, vol. 20, no. 15, p. 4183, 2020.

[225] Q. Wu, Z. Mei, Z. Lai, D. Li, and D. Zhao, "A Non-Contact Vital Signs Detection in a Multi-Channel 77GHz LFMCW Radar System," *IEEE Access*, vol. 9, pp. 49 614–49 628, 2021.

[226] M. Weenk *et al.*, "A smart all-in-one device to measure vital signs in admitted patients," *PLoS One*, vol. 13, no. 2, p. e0190138, 2018.

[227] T. Lauteslager *et al.*, "Validation of a New Contactless and Continuous Respiratory Rate Monitoring Device Based on Ultra-Wideband Radar Technology," *Sensors*, vol. 21, no. 12, p. 4027, 2021.

[228] H. Xu *et al.*, "Accurate Heart Rate and Respiration Rate Detection Based on a Higher-Order Harmonics Peak Selection Method Using Radar Non-Contact Sensors," *Sensors*, vol. 22, no. 1, p. 83, 2021.

[229] Y. Xiong *et al.*, "Differential Enhancement Method for Robust and Accurate Heart Rate Monitoring via Microwave Vital Sign Sensing," *IEEE Trans. Instrum. Meas.*, vol. 69, no. 9, pp. 7108–7118, 2020.

[230] Y. Ding *et al.*, "A Novel Real-Time Human Heart Rate Estimation Method for Noncontact Vital Sign Radar Detection," *IEEE Access*, vol. 8, pp. 88 689–88 699, 2020.

[231] H.-I. Choi, W.-J. Song, H. Song, and H.-C. Shin, "Improved Heartbeat Detection by Exploiting Temporal Phase Coherency in FMCW Radar," *IEEE Access*, vol. 9, pp. 163 654–163 664, 2021.

[232] Y. Xiong, S. Chen, X. Dong, Z. Peng, and W. Zhang, "Accurate Measurement in Doppler Radar Vital Sign Detection Based on Parameterized Demodulation," *IEEE Trans. Microw. Theory Tech.*, vol. 65, no. 11, pp. 4483–4492, 2017.

[233] K. E. Sandau *et al.*, "Update to Practice Standards for Electrocardiographic Monitoring in Hospital Settings: A Scientific Statement From the American Heart Association," *Circulation*, vol. 136, no. 19, pp. e273–e344, 2017.

[234] S. Nizami, J. R. Green, and C. McGregor, "Implementation of artifact detection in critical care: A methodological review," *IEEE Rev. Biomed. Eng.*, vol. 6, pp. 127–142, 2013.

[235] US Food and Drug Administration, *Guidance for Industry: cardiac monitor guidance*, (accessed in December, 2022).

[236] ——, *Pulse Oximeters - Premarket Notification Submissions [510(k)s]: Guidance for Industry and Food and Drug Administration Staff*, (accessed in December, 2022).